



Institut für Technische
Thermodynamik



Functionally Graded Anode Catalyst Layers for PEM Water Electrolysis

Funktionell gradierte Anoden-Katalysatorschichten für die PEM
Wasser-Elektrolyse

Bei der Fakultät für Mathematik und Naturwissenschaften der Carl von
Ossietzky Universität Oldenburg zur Erlangung des Grades und Titels eines

Doktors der Naturwissenschaften

Dr. rer. nat.

eingereichte Dissertation

von Herrn Marius Gollasch
geboren am 15.08.1994 in Delmenhorst

Erstgutachter:

Prof. Dr. Michael Wark
Institut für Chemie, Carl von Ossietzky Universität Oldenburg, Deutschland

Zweitgutachter:

Prof. Dr. Marc Secanell Gallart
Department of Mechanical Engineering, University of Alberta, Edmonton, Kanada

Abstract

The dependence on expensive and scarce Ir catalysts hampers the widespread application of proton-exchange membrane water electrolysis systems, making the reduction of required materials crucial for the future role of this technology in energy transition. More efficient utilization of catalyst material can accelerate its commercialization; even minor gains in catalyst efficiency can have a substantial overall impact. This thesis examines novel gradient-based designs for anode catalyst layers with the aim of enhancing catalyst utilization and efficiency, potentially reducing the necessary amounts of Ir.

Several different supported Ir-based catalyst syntheses are evaluated, considering their electrochemical activity, stability, reproducibility, and specificity of the desired Ir loading. A catalyst developed using the modified Adam's fusion approach is identified as optimal for further use in this thesis due to its relatively high activity towards the oxygen evolution reaction and excellent stability, primarily attributed to its predominantly rutile-IrO₂ composition.

This catalyst is subsequently used to create homogeneous and gradient-design catalyst layers. Their characterization provides insights into specific local overpotentials during catalyst layer operation and the gradient's impact on them. Beneficial interactions are observed between the Ir species and the Sb-doped SnO₂ support, enhancing kinetic parameters significantly beyond metallic Ir reference catalysts. This improvement is theorized to arise from strong metal-support interaction, possibly induced by a semiconductor-metal junction interface between the particles, leading to positive effects on the overall catalyst. The gradient design, based on differential Ir loading along the thickness of the catalyst layer, results in improved overall performance, exceeding the expected average of both homogeneous sublayers. Various effects on electrical conductivity and ionic transport resistance are observed, determined by the positioning of individual sublayers. These effects lead to a reduction in overall cell potential, thus enhancing catalyst efficiency. A higher Ir loading near the porous transport layer proves to be beneficial to performance, yielding the highest performing layer based on the catalyst loading, likely due to reduced local electrical resistances.

Another gradient design, based on differential ionomer loading, is also investigated, revealing beneficial effects and leading to higher performance for the gradient layers compared to the homogeneous ones. An optimized ratio of ionomer-

occupied volume to pore volume appears to be the most influential factor in this context, facilitating an optimized in-plane and through-plane electrical conductivity of the catalyst layer. Both variants of the gradient design lead to improved performance and optimized local overpotential terms for the catalyst layers examined here, leading to a promising concept for catalyst layer design in proton-exchange membrane water electrolysis.

Kurzfassung

Die Abhängigkeit von teuren und knappen Ir-Katalysatoren dämpft die breite Anwendung von Protonenaustauschmembran Wasserelektrolysesystemen, so dass die Verringerung des Materialbedarfs für die künftige Rolle dieser Technologie bei der Energiewende entscheidend ist. Eine effizientere Nutzung des Katalysatormaterials kann die Kommerzialisierung dieser Technologie beschleunigen; selbst geringfügige Steigerungen der Katalysatoreffizienz können einen erheblichen Gesamteffekt haben. In dieser Arbeit werden neuartige, auf Gradienten basierende Strukturen für Anodenkatalysatorschichten mit dem Ziel untersucht, die Katalysatorausnutzung und -effizienz zu verbessern und möglicherweise die erforderlichen Mengen an Ir zu reduzieren.

Es werden mehrere verschiedene Katalysatorsynthesen auf Ir-Trägerbasis unter Berücksichtigung ihrer elektrochemischen Aktivität, Stabilität, Reproduzierbarkeit und Spezifität der gewünschten Ir-Beladung bewertet. Ein Katalysator, der mit dem Adam's Fusions-Ansatz entwickelt wurde, konnte als optimal für die weitere Verwendung in dieser Arbeit angesehen werden. Dies beruht auf dessen relativ hohen elektrochemischen Aktivität gegenüber der Sauerstoffevolutionsreaktion und der ausgezeichneten Stabilität, die in erster Linie auf seine überwiegende Rutil-IrO₂-Zusammensetzung zurückzuführen ist.

Dieser Katalysator wird weiterhin zur Herstellung von homogenen und Gradienten-Katalysatorschichten verwendet. Die Charakterisierung dieser Schichten gibt Aufschluss über spezifische lokale Überspannungen während des Betriebs der Katalysatorschicht und die Auswirkungen der Gradientenstruktur auf diese. Zwischen den Ir-Spezies und dem Sb-dotiertem SnO₂-Träger werden vorteilhafte Wechselwirkungen beobachtet, die die kinetischen Parameter im Vergleich zu metallischen Ir-Referenzkatalysatoren erheblich verbessern. Es wird angenommen, dass diese Verbesserung durch Metall-Metalloxid Trägerinteraktionen zustande kommt, möglicherweise durch eine Halbleiter-Metall-Kontakt an der Grenzfläche zwischen den Partikeln, was sich positiv auf den gesamten Katalysator auswirkt. Das Gradientendesign, das auf einer unterschiedlichen Ir-Beladung entlang der Dicke der Katalysatorschicht beruht, führt zu einer verbesserten Gesamtleistung, die den erwarteten Durchschnitt der beiden homogenen Teilschichten übertrifft. Es werden verschiedene Auswirkungen auf die elektrische Leitfähigkeit und den Ionen-transportwiderstand beobachtet, die durch die Positionierung der einzelnen Teilschichten bestimmt werden. Diese Effekte führen zu einer Verringerung des Ge-

samzellpotenzials, wodurch die Katalysatoreffizienz verbessert wird. Eine höhere Ir-Beladung in der Nähe der porösen Transportschicht erweist sich als vorteilhaft für die Leistung und führt zur leistungsstärksten Schicht auf der Grundlage der Katalysatorbeladung, was wahrscheinlich auf geringere lokale elektrische Widerstände zurückzuführen ist.

Ein weiteres Gradientendesign, das auf einer unterschiedlichen Ionomerbeladung basiert, wird ebenfalls untersucht, wobei sich vorteilhafte Effekte zeigen und die Gradientenschichten im Vergleich zu den homogenen Schichten eine höhere Leistung aufweisen. Ein optimiertes Verhältnis von Ionomer-besetztem Porenvolumen zum gesamten Porenvolumen scheint in diesem Zusammenhang der einflussreichste Faktor zu sein, der eine optimierte elektrische Leitfähigkeit der Katalysatorschicht in der Ebene und quer zur Ebene ermöglicht. Beide Varianten des Gradienten-Designs führen zu einer verbesserten Leistung und optimierten lokalen Überspannungstermini für die hier untersuchten Katalysatorschichten, was zu einem vielversprechenden Konzept für das Design von Katalysatorschichten in der Protonenaustauschmembran Wasserelektrolyse führt.

Danksagung

Zu Beginn möchte ich meine Dankbarkeit all jenen aussprechen, die mich während dieser Doktorarbeit begleitet und mich uneingeschränkt unterstützt haben.

Ein besonderer Dank gebührt Prof. Dr. Michael Wark. Nicht nur für das sorgfältige Begutachten dieser Arbeit, sondern auch für den wissenschaftlichen Austausch und die Betreuung, die er mir in den vergangenen drei Jahren zukommen ließ bin ich dankbar. Ebenso möchte ich mich bei Prof. Dr. Marc Secanell Gallart bedanken für die Übernahme des Zweitgutachtens.

Ein aufrichtiger Dank geht an Dr. Corinna Harms. Ohne ihre Unterstützung wäre meine Promotion am DLR und der fruchtbare Austausch während dieser intensiven Zeit nicht möglich gewesen. Weiterhin bin ich Dr. Julian Lorenz, Sebastian Bragulla, Arne Schechterle, Konstantin Rücker und der gesamten AMEC Gruppe zutiefst verbunden. Ihre Unterstützung im Labor, der wissenschaftliche Austausch und ihre Hilfe bei der Bewältigung zahlreicher Herausforderungen waren für mich unersetzlich.

Darüber hinaus gilt mein Dank allen Mitgliedern der Arbeitsgruppe Wark. Ihr wissenschaftlicher Austausch in den Seminaren und die Unterstützung haben mich voran gebracht.

Ein besonderer Dank geht an die Arbeitsgruppe des Energy Systems Design Laboratory der University of Alberta in Edmonton, Kanada. Ihre herzliche Aufnahme und der inspirierende Forschungsaufenthalt waren einzigartig. Ein spezieller Dank an Eric Beaulieu, der mir die kanadische Kultur näherbrachte.

Ich bin auch Jasmin Schmeling dankbar für ihre Unterstützung bei den Laborarbeiten und ihr Engagement, welches zu einem beidseitig erfolgreichen Forschungspraktikum führte. Ebenso danke ich Jana Ewert für ihre wertvolle und tatkräftige Hilfe bei zahlreichen Messungen, insbesondere bei den ICP-MS und SEM Charakterisierungen.

Zuletzt aber gilt der allergrößte Dank meiner Familie, meinen Eltern, Lukas und insbesondere Julia für die Unterstützung und den unermüdlichen Rückhalt in jeglicher Hinsicht während dieser Promotion.

Contents

Abstract	i
Kurzfassung	iii
Danksagung	v
1 Introduction	1
2 Motivation	3
3 Fundamentals	5
3.1 Water Electrolysis	5
3.1.1 Principles	5
3.1.2 Application Technologies	10
3.1.3 Oxygen Evolution Catalysts in Acidic Environment	16
3.2 Catalyst Layer Design	22
4 Methods	29
4.1 Electron Microscopy	29
4.2 X-ray Techniques	30
4.3 Other Physical Characterizations	32
4.4 Electrochemical Techniques	34
5 Experimental	39
5.1 Catalyst Synthesis	39
5.2 CCM Preparation via Ultrasonic Spray Coating	42
5.3 Electrochemical Characterisation	43
5.4 Physical Characterisation	47

6	Results and Discussion	51
6.1	Comparative Analysis of Ir Catalyst Syntheses	51
6.1.1	Ir Deposition Reproducibility and Precision	53
6.1.2	Physical and Morphological Characterization	55
6.1.3	Electrochemistry	66
6.1.4	Evaluation of the Synthesis Methods	74
6.2	Ionomer Gradient catalyst coated membranes (CCMs)	77
6.2.1	Influence of Ionomer Content on CCMs	77
6.2.2	Influence of Ionomer Gradient Design	90
6.3	Catalyst Loading Gradient CCMs	99
6.3.1	Optimization of Ionomer Content	99
6.3.2	Influence of a Varied Ir Loading in IrO ₂ /ATO CCMs	101
6.3.3	Gradient Ir Loading CCMs	112
7	Conclusions and Summary	117
8	Outlook	121
	Bibliography	123
A	Appendix	133
A.1	List of Figures	133
A.2	List of Tables	137
A.3	Supplementary Figures	138
A.4	Supplementary Tables	140
A.5	Supplementary Equations	143
A.6	Publication and Conference Contributions	144
A.7	Abbreviations and Symbols	145

1 Introduction

Anthropogenic climate change presents one of the most substantial challenges humanity faces today, caused by the emission of greenhouse gases.^[1] These gases absorb and re-emit infrared radiation in the atmosphere, leading to a concentrating effect of heat energy on the Earth's surface.^[2] The rising temperatures lead to increasing probabilities of considerable destructive events, such as floods, heat waves, and the loss of habitats.^[1-3] Already, the global average temperature has increased by about 1.2 °C with emissions still rising. Therefore, it is vital to reduce further increases in global temperatures. It has been estimated that a maximum increase of 1.5 °C compared to pre-industrial levels by 2030 would already be destructive worldwide. Thus, the emission of greenhouse gases, most prominently CO₂, needs drastic reduction to achieve this goal. A decrease of about 43 % of global emissions compared to those in 2019 is needed at least by 2030 to accomplish the 1.5 °C target.^[3] However, according to the OECD, greenhouse gas emissions are currently predicted to increase by about 10 % by that year instead of decreasing.^[3] The Paris climate agreement has set the target at a 2 °C temperature increase, with most countries working towards a similar target of setting a climate-neutrality goal by 2050.^[3,4] Achieving these goals requires a complete transformation of the world's energy systems, shifting away from fossil-based fuels to renewable and emission-free energy. Multiple sectors, including the energy sector itself, transportation, building, and heating sectors, need to convert their energy usage.^[4] The phasing-out of fossil-burning energy producers, such as coal

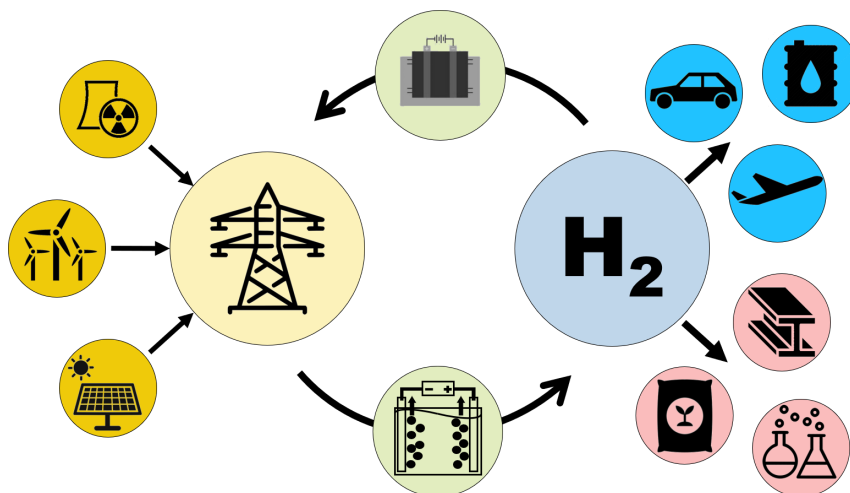


Figure 1.0.1: Circular hydrogen economy schema depicting emission-free electricity generation in yellow, transportation-based hydrogen applications in blue and, industrial hydrogen application in red.

and gas power plants, is already underway, with Germany proposing complete coal energy replacement before 2038 and a substantially increased focus on renewable electricity generation through solar and wind sources.^[5] Not only will the current energy supply be replaced by renewable sources, but the overall energy demand is said to increase even further, placing significant stress on the expansion of solar and wind energy.^[6] This also extends to the transportation sector, where gasoline and diesel need to be replaced by electricity-based propulsion for cars, trucks, and also planes or ships. The shipping sector alone is responsible for about 2 % of global CO₂ emissions, but electrification is not easily feasible through the use of batteries. Even the intermittency of renewable energy generation requires more energy storage in the electricity grid, as peak solar output is usually at off-peak consumption hours. Climate-neutral generated hydrogen is poised to play a large role in the energy transition as it can be utilized as an energy carrier in different sectors, such as fuel for cars and ships or re-electrified in fuel cells as grid balancing plants. Its generation can be achieved through electrolysis of water with an electricity supply and transported much easier than batteries or other energy storage media. The German government puts a big focus on the economy of hydrogen as an energy carrier in many different forms throughout all sectors.^[7] By 2030, a requirement of about 90 to 110 TWh of hydrogen in all sectors is estimated, and domestic production will not be sufficient long-term. It is also proposed to be used as feed stock for many currently fossil-fuel-driven processes, such as steel-making and the chemical industry.^[7,8] Furthermore, it can be converted to different zero-emission fuels like ammonia and green methanol or used directly in either hydrogen combustion engines or fuel cells. The generation, as well as the import and export of hydrogen at a global scale, will play a big role in the transition to a climate-neutral world by 2050 and reaching the goal of a limited global temperature increase below 1.5 °C.

2 Motivation

The role of water electrolysis in the hydrogen economy is crucial as it is the generation backbone for all following technologies that utilize the energy carrier. This puts special focus on the scalability of the technology to produce hydrogen at a relatively low cost and at massive scale while reducing the electricity required. For a successful transformation of the energy system, the generation of hydrogen also needs to be economically feasible for market-penetration since subsidies are not sufficient at this scale. Currently, the implementation of electrolysis systems invests in the idea of a future green hydrogen economy as it cannot compete with hydrogen from fossil fuels at current prices of about 3.2-8.2 \$ kg⁻¹ and 1.5-1.8 \$ kg⁻¹, respectively.^[9] Extended capacities for low-cost renewable energy are projected to change this dynamic as the cost for hydrogen generation is 70-90 % electricity expenditure.^[9,10] As the electricity cost from renewables declines, the hydrogen price is expected to decrease accordingly, especially in Asia where renewables could half the price for hydrogen in the coming years.^[9] With the current efficiency of a proton-exchange membrane (PEM) water electrolysis system, the price of green hydrogen could surpass that from fossil-sources by 2030 without subsidies.

Different electrolysis technologies excel in various applications, as the PEM system is especially adept at handling fluctuations in the renewable load.^[9-13] This puts this technology on the forefront for an increasing renewable electricity share but is currently held back not only by high electricity costs but also high upfront investment costs.^[10-12] This high capital expenditure (CAPEX) is mainly due to specialized materials used in the cell, such as machined Ti and noble-metal catalysts. At scale, the cost of Ti components is projected to be dominant for CAPEX costs but substantial research effort is put into alternative materials. In addition, the efficiency of the catalyst is of utmost importance, as the operational expenditure (OPEX), mainly determined by the electricity price, can make up a large portion of the overall electrolyzer cost depending on yearly operation hours. Besides the high costs of noble-metal catalysts, its scarcity might become a considerable challenge as the annual production of Ir is quite low even compared to other noble-metals as it is one of the scarcest elements in the Earth's crust. The decarbonization of the transport sector alone is projected to require more than half of the annual Ir production by 2100.^[9] Already, its price has tripled in 2020 and is only poised to increase further with ongoing adoption of PEM electrolysis systems.

Without suitable non-noble-metal catalysts, the reduction of used material for adequate efficiency is paramount to an ongoing adoption of the technology and its role in the energy transition. Increased electrical efficiency can be achieved through development of novel catalysts and is an ongoing research effort with several materials being considered. Another important aspect is the efficient utilization of the materials currently used in order to avoid unnecessarily high catalyst loadings.

Traditional electrolysis cell design is based on a thin catalyst layer (CL) with a homogeneous composition in all spatial dimensions. The adaption and redistribution of material within the layer could increase its utilization through a homogenization of the reaction rate, which is not uniform in a homogeneous layer.^[14–16] With an increased catalyst utilization the overall Ir loading can be reduced and would significantly impact the technology's long-term prospects. A gradient CL design was already investigated for fuel cell applications but remains a yet unexplored area in the field of PEM water electrolysis. This thesis focuses on the adaption of this design for PEM water electrolysis anode CLs with different material gradients and the evaluation of its feasibility. To this end, the project is separated into three parts which complement each other.

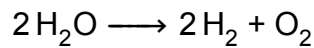
The first part is a study into several catalyst synthesis methods is carried out to find a suitable catalyst for the third project and with that a recommendation for laboratory and industrial applications is given. The goal here is to provide a systematic overview for different methods to yield a Ir or IrO_x/IrO₂ catalyst, supported on an Sb-doped SnO₂ (ATO) substrate. This catalyst is then used in the third project where it is produced with different amounts of Ir on the support material. Second is the implementation of an ionomer gradient for CL's with the ionomer component varying along the CL's thickness and its contributions to the cells efficiency and performance are analyzed in order to evaluate the gradient of this component. Finally, the catalysts produced in the first part are used to generate gradient CLs with an Ir loading gradient along its thickness. The goal here is to generate and evaluate a more efficient CL with a more rational distribution of Ir particles compared to homogeneous layers. All gradient CLs are investigated in a close-to-application testbench setup with several electrochemical characterization techniques to assess individual overpotential contributions pertaining to the gradient design. Through this effort, the layers can be optimized and their adaption to industrial application may be evaluated further on. This thesis is designed to give elementary insights into this novel CL design for PEM water electrolysis and expedite development of more efficient water electrolysis systems.

3 Fundamentals

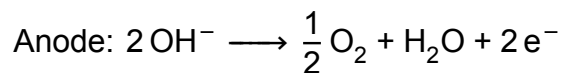
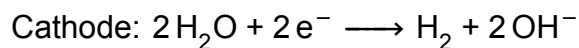
3.1 Water Electrolysis

3.1.1 Principles

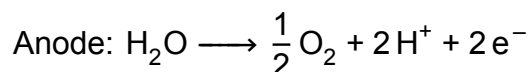
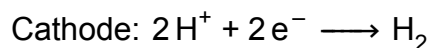
The process of water electrolysis to produce hydrogen and oxygen gas by supplying an electrical direct current to water was discovered over 250 years ago.^[17,18] Since then, this process was used extensively, with first industrial-scale electrolyzers appearing around 1900.^[19] The basic reactions in liquid water are divided into two half-cell reactions, which are as follows:^[20,21]



Each half-cell reaction depends on the pH value of the liquid water present since the charge carrier can either be H^+ or OH^- in liquid electrolyte. In an alkaline pH value, the charge carrier is OH^- , and the half-reactions proceed as follows with the reduction of water to produce H_2 gas (known as the hydrogen evolution reaction (HER)) and the oxidation of OH^- to produce O_2 (known as the oxygen evolution reaction (OER)).^[20,22]



In an acidic electrolyte, the charge carrier is H^+ , and the following half-cell reactions occur during water splitting.^[22]



The conversion of water to its constituents is not spontaneous at standard conditions because its free Gibbs enthalpy (ΔG°) is positive at 237 kJ mol^{-1} .^[9,11] This energy is determined by the reaction temperature (T), its change in entropy (ΔS°),

3.1 Water Electrolysis

and its change in enthalpy (ΔH°), according to Equation 3.1.^[9,20,23]

$$\Delta G^\circ = \Delta H^\circ - T \Delta S^\circ \quad (3.1)$$

To initiate the reaction, energy must be supplied, which can be done efficiently in an electrochemical cell by supplying electrical energy in the form of electrons. The electrochemical potential that must be overcome is the reversible standard potential (E^0) of the reaction at which the reaction is in equilibrium at standard conditions. This translates to ΔG° in relation to the electrical charge passed through the system according to Equation 3.2.^[20,23]

$$E^0 = -\frac{\Delta G^\circ}{zF} \quad (3.2)$$

Here, the electrical charge is described by the electron transfer number (z) and the Faraday constant (F) ($9.6485 \times 10^4 \text{ C mol}^{-1}$). E^0 for the equilibrium reaction of $\text{H}_2\text{O} \rightleftharpoons \text{H}_2 + \frac{1}{2} \text{O}_2$ is 1.23 V vs. RHE with two electrons transferred overall, while the sign for E^0 is dependent on the direction of the reaction as a convention since the sign of E^0 is related to the sign of ΔG° .^[9,22,23] The potential of an actual electrochemical cell potential (E) deviates from E^0 according to the activity (a), which is proportional to the partial pressure in case of gaseous species, of the reactants as described by the Nernst equation 3.3.^[11,23]

$$E = E^0 + \frac{RT}{zF} \ln \frac{a(\text{O}_2)^{0.5} a(\text{H}_2)}{a(\text{H}_2\text{O})} \quad (3.3)$$

Here, R is the universal gas constant. According to this, the E^0 of the overall electrochemical reaction can also be assigned to E^0 of each individual half-cell reaction as:^[23]

$$E^0 = E_{cat}^0 - E_{ano}^0 \quad (3.4)$$

In the case of the water-splitting reaction, the convention of potentials given is against the reversible hydrogen electrode (RHE), which is the same reaction as the cathode reaction and thus 0.0 V vs. RHE. Hence, E^0 is determined by the anode reaction with 1.23 V vs. RHE. However, this is only the case for strong acidic electrolytes with a pH value of 0. The half-cell reaction E^0 shifts with the pH values according to the Nernst equation and their respective activities, as depicted in the Pourbaix diagram in Figure 3.1.1.a.^[24] The overall potential difference remains the same at 1.23 V vs. RHE, but each reaction's E^0 shifts to $E_{cat}^0 = -0.414 \text{ V}$ and $E_{ano}^0 = 0.815 \text{ V}$ for a neutral pH value of 7 and to $E_{cat}^0 = -0.828 \text{ V}$ and $E_{ano}^0 = 0.401 \text{ V}$

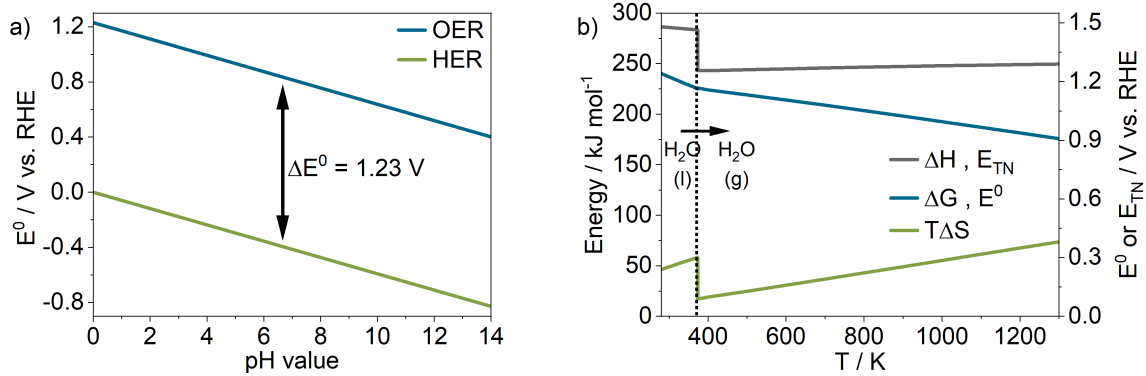


Figure 3.1.1: Schematic representation of a) the Pourbaix diagram of liquid water, showing the pH value dependence of E^0 according to the Nernst equation and b) the change of thermodynamic parameters with the reaction temperature for liquid and gaseous water along with their respective E^0 or E_{TN} . The depictions were adapted by Li *et al.*^[24] with thermodynamic parameters taken from the NIST-JANAF database for thermodynamic parameters.^[25]

for a strong alkaline pH value of 14, respective to the RHE potential.

During this reaction, a change in entropy occurs and thus causes the reversible cell voltage to be dependent on T , as depicted in Figure 3.1.1.b.^[22] This makes the reaction at a potential without a change in temperature more appropriate to describe the reaction's standard potential, which is called the thermo-neutral potential (E_{TN}). Here, the consumed energy in the form of heat energy matches the generated one. Equation 3.1 is extended by the term of entropy change, thus yielding equation 3.5, which makes the change in overall enthalpy (ΔH) the determining factor.^[22]

$$E_{TN} = \frac{\Delta H}{zF} = \frac{\Delta G}{zF} + \frac{T\Delta S}{zF} \quad (3.5)$$

In general, this relation implies that with rising temperature, a part of the required energy for the reaction can be supplied as heat energy, thus lowering the relative required amount of electrical energy and rendering the reaction more efficient in terms of supplied electricity.^[11] At standard conditions, this change in entropy is described as ΔS° with a value of 48.7 kJ mol^{-1} .^[24] As liquid water is typically supplied to the reaction, the phase change from the liquid state of water to the gaseous state has to be considered, and thus two values for ΔH emerge as an approximation for the continuous temperature-dependent change in Figure 3.1.1.b.^[11,22] These are known as the higher heating value (HHV) for liquid water and lower heating value (LHV) for gaseous water, with ΔH values of 286 kJ mol^{-1} and 242 kJ mol^{-1} , respectively.^[22] These energy values are the sum of ΔG and ΔS

at the respective conditions. Per definition, the HHV is the energy difference of a specified amount of fuel being combusted at 25 °C and the products equilibrated back to 25 °C, while the LHV is equilibrated to 150 °C.^[24] This results in E_{TN} of 1.48 V vs. RHE with liquid water and 1.25 V vs. RHE for steam.^[11] If E is below E_{TN} , heat must be supplied to the reaction as it is endothermic, and above E_{TN} , it becomes exothermic and produces heat.

Besides the thermodynamic constraints of the water-splitting reaction imposed and described by the Nernst equation, E is determined by the overpotential as a general descriptor for energy losses, resulting in the sum of inherent thermodynamic potential contributions in E_{TN} and additional potential increases in form of overpotentials, which also include kinetic aspects of the specific reaction.^[24] Specific terms of the overpotential can be attributed to various parts of an application level water-splitting cell, such as activation losses of charge transfer, ohmic losses through electrical conduction, and electrolyte mass transfer losses through ionic conduction of charge carriers. The decrease of different overpotential contributions is paramount for efficient application of the water-splitting reaction for energy-efficient gas production. The voltage efficiency (VE) of an electrolytic cell is typically defined by the ratio of E_{TN} to its E with the HHV or LHV used for calculating E_{TN} depending on the application.^[11] Additionally, the Faradaic efficiency (FE) is often compared between electrolysis devices as it encompasses all energy losses and compares the amount of product gas stream to the theoretical one calculated from consumed current, according to Equation 3.6.^[24]

$$FE = \frac{\dot{n}_{gas,produced}}{\dot{n}_{gas,theoretical}} = \frac{\dot{n}_{gas,produced}}{i (zF)^{-1}} \quad (3.6)$$

Here, \dot{n} represents the substance flow and i denotes the current passing through the electrolysis cell. Alternatively, the product gas amount produced over time can be related to the consumed electrical charge instead of the current in a given time interval. In modern applications, a catalyst is almost always used at the interface between the electrolyte and electrode to reduce the activation overpotential (η_{act}) caused by charge transfer from the reactant to the external circuit. Depending on the technology's environment, the catalyst has to possess certain properties such as electrical conductivity, chemical stability, and, most importantly, the ability to lower the activation energy required for the reaction to proceed. These catalysts are typically made from metals, metal oxides, or composite materials. The activation behavior of a catalyst in an electrochemical reaction can be described by the Butler-Volmer theory.^[23,26] This theory describes the energy barrier of an electro-

chemical reaction on a heterogeneous interface based on the applied potential and how this barrier can shift.^[23] According to the current-potential characteristic defined by Butler and Volmer, the reaction's current, either produced or consumed, is dependent on the applied overpotential. Thus, a reaction rate can be driven by increased potential. Assuming mass transport is neglected, the driven current (i) of the reaction can be described approximately by Equation 3.7.^[23]

$$i = i_0 \left(e^{\frac{\alpha_{ano} z F \eta}{RT}} - e^{-\frac{\alpha_{cat} z F \eta}{RT}} \right) \quad (3.7)$$

Here, i is defined by overpotential (η), exchange current (i_0), and anodic charge transfer coefficient (α_{ano}) and cathodic charge transfer coefficient (α_{cat}) also named symmetry factors. This approximation allows for a description of η_{act} solely based on kinetic effects, representing the catalyst's activity towards the water-splitting reaction. For this approximation to be valid, all other contributions of the overpotential must be compensated, such as ohmic and ionic conductivity resistances. At large overpotentials, one side of the reaction becomes insignificant as the reaction heavily shifts in one direction, and one of the exponential terms becomes negligible.^[23] Therefore, Equation 3.7 can be rearranged to yield Equation 3.8:

$$\eta = \frac{RT}{\alpha F} \ln i_0 - \frac{RT}{\alpha F} \ln i \quad (3.8)$$

From this form, the relation to the Tafel description of kinetics becomes apparent, and the kinetic parameter α can be analytically extracted by constructing a Tafel plot. In this plot, overpotential is plotted against $\log i$, as shown in Figure 3.1.2. From the linear portion of the curve at higher overpotentials, the slope can be determined and either directly compared between catalysts as the often reported Tafel slope or α can be extracted from the slope's value.^[12,23,27]

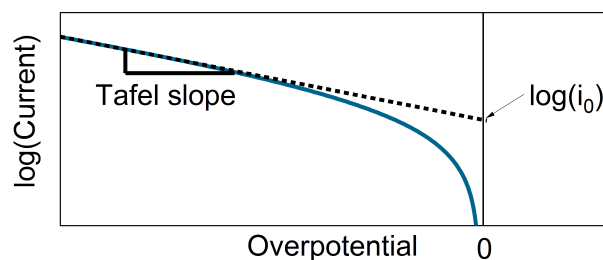


Figure 3.1.2: Schematic representation of the Tafel plot with extractable parameters.^[12,23,27]

The slope takes the form of equation 3.9.^[23]

$$\frac{\Delta \log i}{\Delta \eta} = \frac{-\alpha F}{2.3RT} \quad (3.9)$$

In real applications of electrocatalysts, the approximation of Equation 3.7 regarding the neglected mass-transport may not be applicable, and the Tafel plot can become non-linear again at high enough overpotential, with mass transport being superimposed on η_{act} . This caveat has to be addressed analytically when interpreting the Tafel plot of a given catalyst.

3.1.2 Application Technologies

The transition from the fundamental reaction to actual applicable devices introduces many additional factors that need to be addressed, such as heat transport, reactant and product transport, additional overpotential, and charge carrier choice. Over the years, three main variations have been established within the scope of large-scale H₂ production from electricity, each leveraging different thermodynamical aspects of the water-splitting reaction.^[20,24] These technologies have been under investigation for different amounts of time and are thus at different technological readiness levels. They are mainly characterized by their charge carrier method and are divided into alkaline water electrolysis (AWE), proton-exchange membrane water electrolysis (PEMWE), and solid-oxide water electrolysis (SOWE).

Alkaline Water Electrolysis This technology has the longest history, with its first industrial application more than 100 years ago, mainly for the production of H₂ for NH₃ production.^[19,26] Since then, a lot of research effort has been invested in this electrolysis variant in both academia and industry, with steady improvements in terms of materials and cell architecture. At its simplest, AWE uses an alkaline liquid electrolyte with two electrodes and a separator between them to avoid mixing of gases.^[18,26,28] The half-cell reactions use OH⁻ as the charge carrier, and thus, the reactions proceed as stated at the beginning in an alkaline electrolyte. The first and simplest design of an AWE stack is known as the unipolar design, where the electrodes are simply inserted in the electrolyte with a separator between the anode and cathode (Figure 3.1.3).^[19,20] However, this design requires large system dimensions as well as possesses a high weight. A more sophisticated and commonly used approach today is the bipolar configuration, where the anode and cathode are connected to metal plates, which also separate each cell (Figure 3.1.3). This leads to a smaller system footprint along with reduced cost.

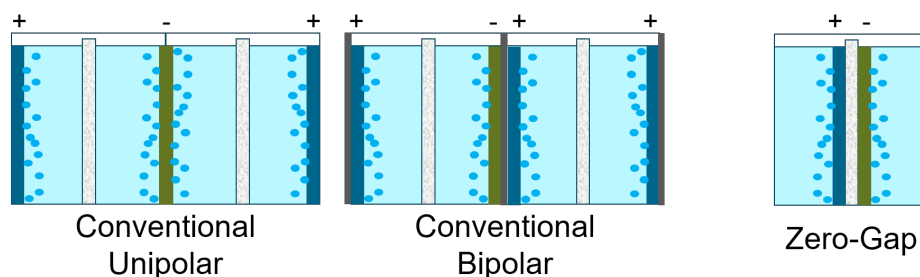


Figure 3.1.3: Schematic of the conventional cell design in unipolar and bipolar multi-cell setup and the zero-gap design with electrodes directly on the separator.

The electrolyte between the electrodes induces resistances based on the separation distance between them, thus decreasing efficiency. A modern solution to this downside is the zero-gap design, where the electrodes are directly pressed onto the separator, reducing the distance between them to a minimum (3.1.3).^[19,20] The separator presents an important part of the cell, especially in regard to safety, as a mixture of the product gases can lead to catastrophic failures. For the longest time, asbestos was used here as it provides excellent mechanical and chemical stability, but has since been outlawed, due to hazardous properties.^[19] Thus, mainly ceramic and polymeric materials have taken its place. Recently, a novel type of AWE cell was presented, which fed the electrolyte through a porous separator due to capillary interactions and thus provided much lower ohmic losses and better gas separation, hence increased efficiency.^[29] The catalyst material of choice, Ni metal, was already used in 1925 for AWE and remains to this day.^[19,20] This provides the benefit of using a similar material for both electrodes and does not pose the need for noble-metal catalysts as in other types of electrolyzers. Most modern catalysts consist of Ni oxides or oxyhydroxides with the addition of small amounts of transition metals. Here, Fe seems to be the metal to boost the electrochemical activity the most.^[19,30,31] The materials used in AWE are mostly accessible and relatively cheap, which makes this technology widely available for industrial-scale applications.^[19,20] It can also produce H_2 at elevated pressure, with today's system providing H_2 with up to 30 bar. However, the maximum current AWE can operate at is lower compared to other technologies, mainly due to the liquid electrolyte used, which consists of an aqueous solution with around 20-40% KOH and is prone to heating under operation conditions.^[19,31] This introduces large ohmic losses and requires fairly high alkaline concentrations, which degrade the peripheral materials of the cell. Additionally, the liquid electrolyte renders the system sluggish, with slow response times to changing loads.^[32] This property is especially important for electrolysis in the context of renewable energy,

which is often very fluctuating, and a fast system response time to the changing load is vital.^[31]

A new approach is to use a semi-permeable membrane instead of the separator, which conducts OH^- ions and is often referred to as anion-exchange water electrolysis (AEMWE). This allows for the usage of pure water or low-concentrated alkaline electrolytes, higher currents, and also higher H_2 pressures (> 30 bar) to improve the system efficiency.^[19,31,33] The main limiting factor of this technology is the membrane, which often shows limited durability. Commercial membranes are already available but with limited lifetime, mainly due to chemical and mechanical degradation under operation conditions.^[31,33] This calls for more research into polymers, conducting OH^- that can be reasonably stable over long operation lifetimes. Thus, this technology is very promising but needs more time to reach the technological maturity of the AWE system.

Solid-Oxide Water Electrolysis The energy required to split water depends on the phase state of the water, including the additional presence of the latent heat of vaporization, as described in Figure 3.1.1. The SOWE technology has a main advantage, making water electrolysis a much more efficient process if the water is supplied in gaseous form, as steam.^[26,34–37] Here, the cell is operated at temperatures between 700 and 900°C, not only providing steam as a reactant but also increasing the reaction rate substantially through the elevated temperature.^[35] The efficiency of a SOWE system can get over 95% if the steam is supplied by an external source, such as waste heat from other industrial processes, which is not possible with other low-temperature technologies.^[34,36] These systems also allow for a wide range of educts, enabling, for example, the co-electrolysis of water and CO_2 .^[34,36] The simultaneous generation of H_2 and CO , also known as syngas, is possible with this process, which is a crucial feedstock for the industrial chemical industry.^[36] Hence, the possible generation of CH_4 directly from the syngas enables direct coupling of the generation of renewable electricity with fuel production in a power-to-gas or power-to-fuel setup.

The design of modern SOWE cells is mainly split into variants, depending on the mechanically supporting component: cathode-supported cells and electrolyte-supported cells.^[34] Each specific component supporting the cell is much thicker than the other cell layers. The charge carrier conducting medium is most often made from a ceramic, such as Y-stabilized ZrO_2 (YSZ) or Gd-doped CeO_2 (GCO), that conducts O^{2-} ions at the elevated operation temperature from the H_2 electrode to the air electrode.^[34] The latter material is becoming more prevalent re-

cently due to its higher ionic conductivity. However, the high sintering temperature above 1500 °C poses a manufacturing problem in the other cell components. At the H₂ electrode, water is reduced to produce H₂ gas and O²⁻ ions and thus needs to be conductive for these and also provide porosity for the transport of gases and electrical conductivity. A metal-modified version of the YSZ or GCO electrolyte, most often Ni metal, is used here to form a ceramic-metal. On the other side of the electrolyte, the O²⁻ ions are oxidized to form O₂ on a doped perovskite catalyst. These are most often Co- and Sr-doped materials, commonly utilizing (La, Sr)(Fe, Co)O₃ or La_{0.8}Sr_{0.2}MnO_{3-δ} perovskite structures. Chemical stability of these materials is one of the main challenges due to migration of dopant elements into the electrolyte.^[34,38] Thus, an intermediate layer is often applied between the electrolyte and air electrode to avoid dopant migration and dampen mismatched thermal expansion of both adjacent materials, which can lead to lower contact or mechanical failure of the cell. This can be a modification of the electrolyte ceramic that is compatible with the electrode, such as Y-doped CeO₃ or GCO.^[34] Another variant of the standard asymmetrical cell is the symmetrical cell design, employing a perovskite catalyst for both electrodes and thus avoiding material mismatch and alleviating manufacturing constraints, leading to lower manufacturing costs.^[37] In general, the main problem hindering SOWE systems is their limited lifetime, which is typically only 2-3 years of operation, lagging behind other electrolysis technologies.^[34,37,38] This can be attributed to the chemical instability, such as migration of Sr and Co, and thermal damage that leads to mechanical instabilities of the materials, like brittleness and delamination. However, further research into this technology can make it a widely adopted electrolysis variant, particularly for use in the chemical industry where steam is readily available, as well as for power stations to generate H₂ with a steady electricity supply.

Proton-Exchange Membrane Water Electrolysis The third main type of water electrolyzer employs a proton conducting membrane, leveraging protons as charge carriers for the water splitting reaction.^[9,10,39] Originally designed for critical applications, such as aerospace missions, where device reliability is more important than manufacturing costs, this type utilizes high noble-metal loadings and thick membranes.^[39] Since its inception in the 1960s, it has been steadily developed to drive down manufacturing costs and has already been applied at a moderate scale. This is mainly due to the invention of the Nafion[®] polymer by DuPont, which is more advanced than the membrane materials currently available for AEMWE.^[11] Figure 3.1.4 shows a schematic of a PEMWE cell. Nafion[®] is a perfluoro sulfonic acid (PFSA) polymer with a perfluoro ethylene backbone

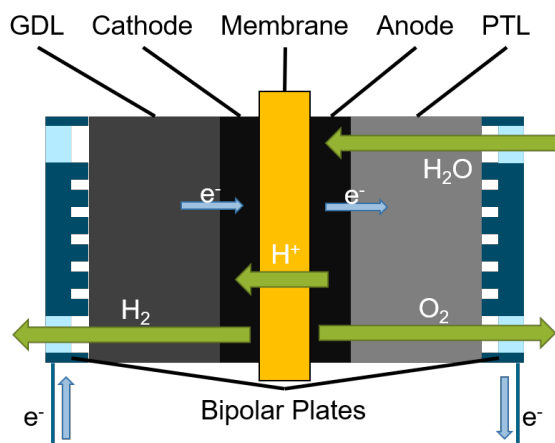


Figure 3.1.4: Schematic of a PEMWE cell.

and sulfonic acid functional groups that facilitate proton conductivity.^[40] The polar groups orient themselves together to form hydrophilic pockets in the polymer, where water can be retained. Thus, the conduction of protons through these pockets is facilitated by a mix of Grotthuss transport and vehicular transport, caused by electroosmotic drag.^[11,40] The hydration of the polymer is crucial as it directly influences ion conductivity and is essential in PEM fuel cell applications. In water electrolysis, however, the membrane is always hydrated enough through the supply of educt water. The membrane has to provide proton conduction between the electrodes but also has to separate the product gases and provide electrical insulation.^[9,12] The separation of products is especially important as crossover not only increases the demand for further purification but can also lead to detrimental outcomes at high concentrations, causing safety concerns.^[21,41] PFSA membranes only ensure sufficient life-times at moderate temperatures up to 90 °C, limiting the application range to liquid water electrolysis, while higher temperatures require novel membrane materials.^[11] In a typical cell, the electrodes are in direct contact with the membrane and are often made from noble metals.

The HER catalyst typically consists of Pt nanoparticles supported on a high surface area C substrate.^[12,42,43] These are similar to the catalysts used in fuel cells and show very fast kinetics, which lower the need for large amounts of Pt.^[9,12] In comparison to the OER anode reaction, the HER is much faster in PEMWE operations, as it operates in an acidic regime with the anode constantly at potentials above 1.48 V vs. RHE, leading to the dissolution of most non-noble catalysts. Consequently, very stable materials are required, which in turn increase the manufacturing cost. State-of-the-art OER catalysts consist of Ir and are further discussed in section 3.1.3.

In addition to the catalyst, other components must also withstand harsh conditions, hence they are most often made from machined Ti.^[12,44] The membrane with both catalysts is further sandwiched by the gas-diffusion layer (GDL) and porous transport layer (PTL) on the cathode and anode, respectively. The GDL can be made from C paper or woven to produce C cloth. These materials have a long history of application in PEM fuel cells and are extensively investigated. Their main task is to facilitate product transport away from the catalyst with a micro-porous mesh in addition to providing electrical conductivity to the surrounding electrical circuit. The PTL in the anode serves the same purpose but has to be made from more resilient materials, such as Ti or noble-metal coated substrates.^[11,45] The oxidative environment leads to oxidation of the PTL surface, which increases contact resistances and thus lowers efficiency, making it one of the main degradation drivers.^[45] Noble-metal coating can alleviate this degradation but comes with increased manufacturing costs. The same treatment can be applied to the bipolar plate (BBP), which surround the GDL and PTL and provide compression as well as mechanical stability to the cell. These can be manufactured from C-based materials, such as graphite on the cathode but require stable materials on the anode. Machined Ti is often used as anode BBPs, incurring high costs and sometimes requiring further noble-metal coating to avoid surface oxidation.^[12,44] The BBPs provide the in- and outlets for educts and products and connect to the electricity supply. In order to spread the educts over the entire active cell area, a flow field is machined into the BBP, which can show different geometries like a serpentine or parallel ridge arrangement.^[46]

For later application of the product gases, they must be further compressed for efficient transport and their end-use.^[47] In order to alleviate the need for compression, the operation of the PEMWE cell can also be performed under elevated pressure of the product gases.^[26] Here, the electrochemical reaction directly compresses the H₂ and O₂ at formation and not only leads to increased system efficiency through less extra compression but also has beneficial kinetic effects on the reaction.^[11] The lower volume of the generated H₂ at the catalyst occupies fewer active sites, which increases the reaction rate. The pressure can be applied equally to both parts of the cell or in differential mode, where the H₂ side is pressurized with the O₂ side at ambient or only slightly increased pressure. This can further increase system efficiency and avoid risks of compressed O₂, but it requires more stable and expensive materials, especially membranes.^[11,12,47] The operation under increased pressure can also increase gas-crossover from one electrode to the other, posing a significant safety concern that must be addressed with operation procedures and additional periphery.^[11,12]

3.1.3 Oxygen Evolution Catalysts in Acidic Environment

Before the introduction of PEMWE cells, research on OER catalysts in acid electrolyte was already present from the early 1960s using different noble metals.^[48] Since the OER at low pH values occurs at fairly high potentials, the catalyst materials must be especially stable. Therefore, only noble metals can be used in this environment without detrimental dissolution, which is why they have been investigated the most. In general, the activity towards the OER can be correlated with the O binding capacity or oxyphilicity, represented in a volcano plot in Figure 3.1.5.^[49–51] The strength of the metal-O bond depends on the d-band position, which comes from the d-orbital combination of the individual atoms in the lattice.^[50,52] A higher occupation of the anti-binding d-states could lower the bond strength and the adsorption strength of the O, and vice versa. Through these effects, the specific metal-O bond strength can be tuned via the synthesis of different material structures resulting in different oxidation states, lattice distortions, or lattice vacancies to influence the d-band position. The bond strength needs to be in a certain range to be neither too strong nor too weak. Figure 3.1.5 shows

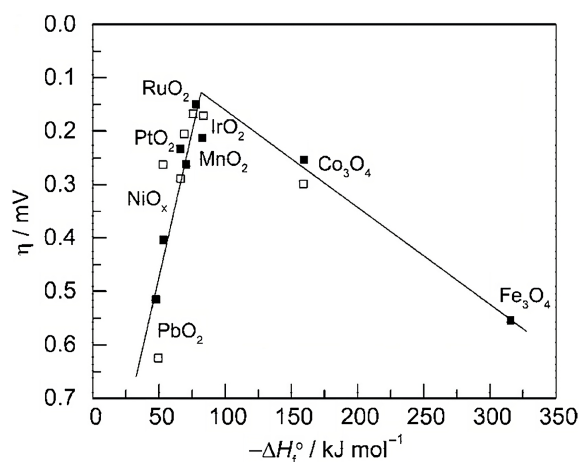


Figure 3.1.5: Electrocatalytic activity in O₂ evolution at various oxide electrodes as a function of the enthalpy of the lower to higher oxide transition in alkaline (hollow) and acidic (full) solutions. Reprinted with permission from [53]. Copyright 1984, Elsevier Ltd.

that the oxides Ir and Ru have superior OER activity compared to other noble metals, especially Pd and Pt, which are very active for the HER and in a fuel cell setting.^[48,54] One advantage of Ir and Ru for the OER is that the oxide phases of these elements, which form during the reaction, are quite active, unlike those of Pt.^[48,55] However, the stability of the noble-metal oxide is inversely proportional to its oxyphilicity, indicating a role of oxide stability in the OER activity. Ru and Ir form less stable oxides than Pt or Au, granting them higher OER activity. For

Ru-based catalysts this presents a major drawback as they are remarkably active but rapidly dissolve under operational conditions.^[48–50,56] Thus, Ir catalysts have been investigated and applied in whole systems the most as a good trade-off between stability and activity. Nonetheless, Ru catalysts are still under investigation because Ru is less scarce than Ir, and stabilizing Ru catalysts could lower manufacturing costs due to material availability.^[57–59] Addition of Ir or its oxides seems to stabilize the catalysts, and thus mixed metal catalysts or alloys could become a promising alternative in the future.^[48,60,61]

The requirements a catalyst has to fulfill to be applied in widespread applications are manifold, including material properties such as electrochemical activity, pore structure, electrical conductivity, and stability, as well as other factors as the availability of materials, price, and the manufacturing method for up-scaled production.^[50,52] Macroscopic structure of a catalyst material can significantly impact its overall activity, even though the intrinsic activity, based on d-band position and other factors, may not be the highest. The available surface area of the catalyst plays a big role here, as exposing more active sites increases its utilization and cost-effectiveness. Pore structure of the material is also crucial, as it affects reactant and product transport and ensures that the active sites are not starved from reactants or blocked by products. One approach to increase the available surface area of the catalyst is to anchor it on a non-catalytic support material, stabilizing small particles and exposing more of their surface.^[50,52] This also reduces the overall content of noble metals in the catalyst and makes it more cost-effective. In some cases, single atoms can be supported on a substrate to maximize the utilization of the metal.^[62,63] For electrochemical applications specifically, the catalyst requires high electrical conductivity, as contact resistances can otherwise significantly diminish the system's efficiency.^[50] This is especially crucial for supported catalysts, as the substrate must also be sufficiently electrically conductive. Material stability is also essential, as the catalyst can dissolve and decrease its activity or become passivated, thereby reducing available surface area and electrical conductivity.^[64] When considering noble metals, availability and subsequent high price can be problematic, especially when scaling up catalyst production.^[52] This is particularly relevant for Ir-based catalysts, as it is one of the scarcest elements in the earth's crust. Additionally, Pt availability plays a role for the cathode of PEMWE systems and as an electrode in PEM fuel cells. A simple synthesis method can lower manufacturing costs, but this must conform to easily scalable industrial processes. However, some catalysts require intricate synthesis, making them commercially unfeasible despite high activity and good properties. Many properties need to be considered when designing a catalyst system and trade-offs

must be made. As the production of Ir for PEMWE catalysts is limited, the recyclability of the cells becomes increasingly important with their expanded application. The recovery of Ir from end-of-life cells can be performed with remarkable efficiency with recovery rates over 90 % without substantial loss in activity or quality.^[65] Catalyst material can either be recovered by thermal decomposition of the entire membrane electrode assembly (MEA) or direct recuperation of catalyst material as described by Carmo *et al.*

Ir-based OER catalysts Ir-based catalysts are the most active for the OER and are also stable, making them highly investigated. During the O oxidation, Ir atoms involved in the reaction are mostly in some oxidic form, either as IrO_2 or lower coordinated Ir oxides.^[50,52] Their exact structure and coordination depends on the operation conditions and catalyst synthesis. As previously discussed, the stability of the metal oxide influences its activity, suggesting the participation of unstable moieties in the reaction mechanism.^[49,50] Two reaction mechanisms proposed are the adsorbate evolution mechanism (ADEM) and the lattice participated mechanism (LPM), which depend on the oxidation degree and crystallinity of the oxide structure.^[49,50,66,67] The ADEM and LPM mechanisms are shown schematically in Figure 3.1.6. The ADEM process involves the adsorption of water molecules

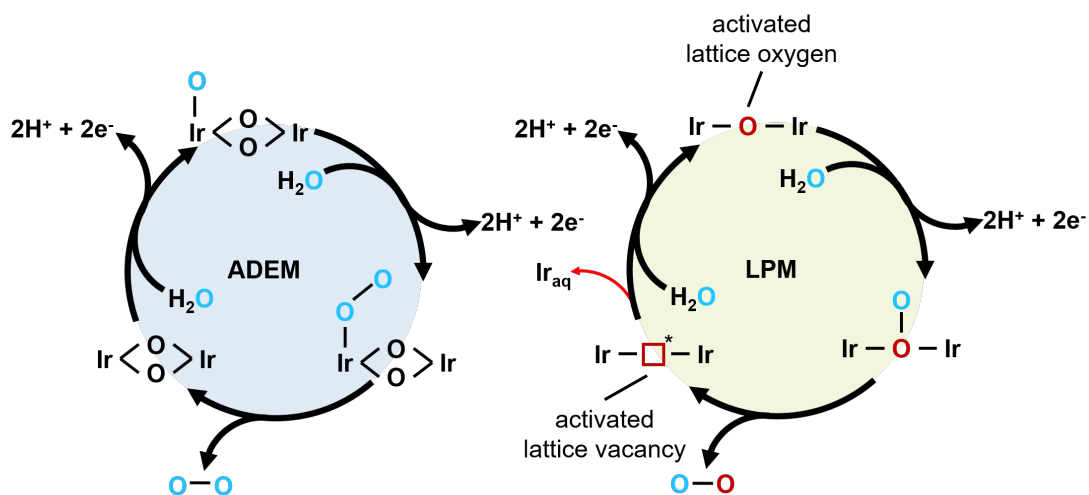


Figure 3.1.6: Schematic representation of postulated ADEM (left) and LPM (right) OER mechanisms, adapted from Geiger *et al.*^[66]

on the surface of the Ir oxide and occurs on the surface of crystalline $[\text{IrO}_6]$ octahedra. First, O is adsorbed on an Ir site from the oxidation reaction of a water molecule under discharge of 2H^+ and 2e^- . Then, a second water oxidation takes place with the O atom adsorbing either on an adjacent Ir site or bound to the already adsorbed O atom, as depicted in the schema. Finally, an O_2 molecule

is discharged without charge transfer, and the Ir site is freed again. In the LPM process, activated lattice oxygen atoms directly participate in the reaction and get expelled with the product O_2 , restoring the lattice vacancy from additional water molecules. Here, in a water oxidation process, the O atom binds to the activated oxygen atom inside the catalyst lattice under discharge of protons and electrons. The O_2 molecule formed from the oxidized water and the lattice atom leaves, while leaving a lattice vacancy that is highly reactive. This vacancy can either proceed in filling an O atom by oxidation of a water molecule, or it can release solvated Ir ions as the structure degrades and dissolves. Both mechanisms are driven at different potentials, but both take place simultaneously and compete.^[52] The LPM is expected to lead to higher OER activity, but the participation of the lattice O atoms can lead to instability of the lattice and dissolution of Ir species.^[52,66] Different oxide structures may favor one mechanism over the other as more defects in the oxide structure lead to higher lattice O activation. This could explain the differences in activity and stability, as promotion of the LPM can lead to lower lifetimes of the catalyst.^[66]

Support Materials The deposition of catalyst material on a high-surface-area support material has been extensively investigated and applied in many different fields of heterogeneous catalysis.^[50] The basic principle is to dilute the active species on a larger substrate to increase the catalyst's available surface area through mechanical and electrochemical stabilization of small active particles. Several properties need to be considered for OER catalysts in PEMWE applications, including sufficient electrical conductivity, electrochemical stability at operating conditions, and the ability for Ir deposition. Different support-catalyst interactions can also modify the electronic structure of the active species and influence the deposition dispersion.^[50,68,69] Supports that have already found application in fuel cells and as cathode PEMWE catalysts are C-based materials. Different studies have shown that they provide excellent activity when combined with Ir catalysts, but they tend to corrode rapidly under harsh OER conditions. C is not stable under elevated potential in acidic pH, and thus, it offers very limited lifetime. Many C modifications have been investigated, including C nanotubes or graphene with very high Ir activity due to their high electrical conductivity and favorable interactions between the catalyst and the π -support structure.^[50,70,71] Nonetheless, limited durability makes them unusable; however, more graphitized and B- or N-doped modifications rather than amorphous ones make more stable C supports possible.^[50,72,73] Long-term investigations into these materials under different real system conditions are still lacking and require more effort, but they pose promising

materials if stabilized. Another category of support materials are transition metal oxides, which are promising since they show adequate stability; however, their electrical conductivity is often low. Some of the most prominent supports here are Ti oxides. These show excellent stability but are practically non-conductive in their TiO₂ rutile and anatase phases. Without direct modification of the Ti oxide phases, the only way to increase electrical conductivity is to drive electrons through the Ir particles, and thus a percolating particle network is required.^[50,74] A lower support surface area could thus counterintuitively increase the catalyst's activity through network formation at lower Ir loadings.^[50,75] Some interaction between the TiO₂ and Ir species was reported as higher oxidation numbers for the Ir were preserved, thus increasing its stability.^[50,76] Another approach is to use a core-shell structure with a TiO₂ core, which improves conductivity while lowering the overall Ir loading. The ubiquitous commercial IrO₂/TiO₂ benchmark catalyst by the company Umicore is an example of this approach. Rutile and anatase TiO₂ phases are practically non-conductive, but suboxide phases, where parts of the Ti lattice are reduced to Ti^{III}, also known as Magnéli phases, show much higher electrical conductivity.^[50,77–80] However, during operational conditions, these supports might be oxidized and thus lose conductivity. Again, a sufficiently high Ir loading might protect the support from excessive oxidation.^[50,81] Stabilization of these suboxides could thus alleviate some of the disadvantages of Ti oxides. In contrast to suboxide Ti, doping of TiO₂ could also improve its conductivity, while avoiding the degradation of Magnéli phase Ti oxides.^[50] When n-type dopants are introduced to the TiO₂ lattice, they provide an e⁻ surplus and distortion of the lattice, resulting in higher conductivity and a modified structure. Most of these elements, such as Nb, V or Ta, thus increase the surface area, its conductivity and can also impact the electrochemical performance through metal-support interaction and have shown to be suitable supports.^[50,82,83]

Among the chemically stable transition metal oxides is SnO₂, which shows poor electrical conductivity but with sufficient Ir loading, this problem could be overcome, similar to the approaches in Ti oxides.^[50] More promising alternatives, however, are doped SnO₂ phases, which drastically increase its electrical conductivity, such as Sb, In, Nb or Ta.^[50,84–86] These materials have been extensively investigated for different applications, including photochemistry and fuel cells. The SnO₂ with the highest electrical conductivity is the Sb-doped variant.^[50,87] This material is also considered to improve Ir dispersion and thus increase mass-based activity.^[50] Still, commercial ATO requires high Ir loadings for adequate performance, but other synthesis methods were shown to increase its activity and thus make lower loadings possible.^[50,74,85] In addition to higher Ir dispersion, ATO seems

to promote lower oxidation states in the Ir species, through strong metal-support interactions (SMSIs) that increase both activity and stability.^[50,68,88] Besides the support materials mentioned, metal nitrides and carbides attracted some attention, especially the Ti ones.^[50] However, more research is still needed on these materials as PEMWE supports.

The design of a supported Ir catalyst is generally not only dependent on the support material but also the Ir deposition method and specific species. As the Ir loading in relation to the support surface area is crucial for less conductive supports, a catalyst system has to be designed as a whole, taking all effects into account. Different supports also provide an electronic interaction with the catalyst species and thus might promote certain Ir species during deposition, which influences their properties.^[50,68,69]

3.2 Catalyst Layer Design

The electrodes of an electrochemical cell are the main contributing factor for the efficiency of the reactions, and their composition has to be carefully designed with multiple different components working together.^[9,89] For both fuel cells and PEMWE cells, the electrode most often consists of the catalyst material, which is mixed with a binder and an electrolyte and thinly coated onto a membrane.^[9,89] Reactions take place where reactants, ionic charge carriers, and electric charge carriers are present at a so-called triple-phase boundary (TPB).^[90] This composition is designed to facilitate the TPB by distributing reactants across the whole CL through a porous network for the reactant and product gases and through an electrolyte network for charge carriers as displayed in Figure 3.2.1. Electric charge carriers are conducted through the catalyst material, which also acts as a reaction site for increased overall efficiency through kinetic reaction promotion. Optimization of this microstructure can have a sizable impact on the performance of the electrochemical cell, and several different parameters have to be considered. The

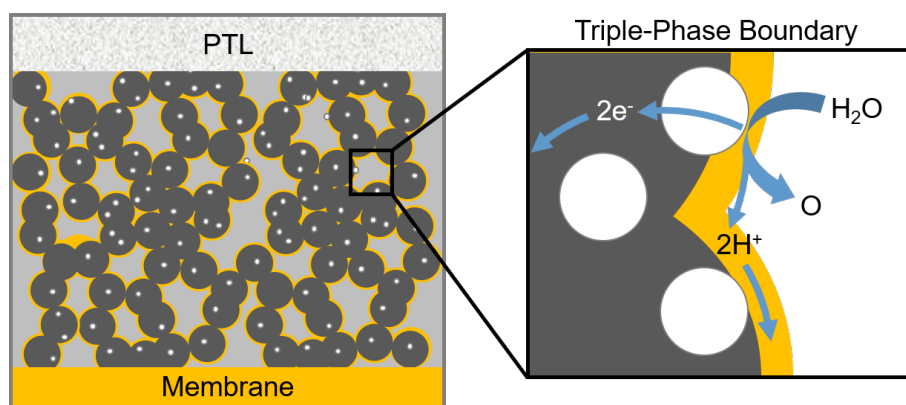


Figure 3.2.1: Schematic representation of a CL with catalyst support indicated in grey, active catalyst in white and ionomer in yellow with indicated TPB and electronic and ionic charge carrier pathways along with reactant pathways.

general optimization process for CLs aims to evaluate the pore structure, thickness, and distribution of the ionomer film, as well as the accessibility of active catalyst sites. Pore structure of the CL is primarily determined by the catalyst material, whether it consists of metal particles or supported particles, which form the rigid framework of the layer. These properties can influence the sizes and distribution of the pores based on particle and agglomerate sizes. The coating process, including the potential use of pore formers or solvent evaporation rates, also plays a role in determining the pore structure.^[91–94] Availability of ionic charge carriers at the TPB is crucial for achieving good performance and it is influenced by the pres-

ence of ionomer at each reaction site and a continuous ionomer network leading to the membrane. In an ideal scenario, the rigid catalyst framework is uniformly covered by a thin film of ionomer. Thickness of this film impacts both the ionic resistivity of the layer, contributing to efficiency losses (with thicker layers providing better conductivity), and the void volume of the pores as the film fills them, thus affecting reactant transport.^[95] Non-uniformly covered catalysts can lead to ionically isolated regions, reducing catalyst utilization and overall efficiency.^[12,96] Furthermore, at high ionomer loadings, an ionomer film can form between catalyst particles, electrically isolating some parts of the catalyst. To maximize the accessible surface area of the catalyst, the particle size can be reduced. This allows for a greater surface area per unit mass, increasing efficiency. Techniques such as utilizing metal nanoparticles, supporting nanoparticles on a substrate, or employing novel engineering approaches with ordered structural substrates can be employed to achieve particle size reduction.^[50,77,97] Especially structural substrates, such as meso- and macroporous TiO_2 , ATO or other metal oxides might allow for a better fine-tuning of CL properties, in particular the pore network and particle accessibility. The deposition of Ir as a thin film of a substrate could also be utilized to achieve a higher utilization, as has been demonstrated by Böhm *et al.*^[98]

The manufacturing of CLs offers multiple approaches, each impacting the CL's properties in different ways. Direct deposition of a catalyst suspension can be achieved through spray coating, inkjet printing, or doctor-blading onto a membrane.^[99–102] Here, the catalyst is suspended in a solvent mixture and combined with a binder and electrolyte and processed to allow for maximum dispersion of all components. Afterward, the CCM is dried and sometimes hot-pressed to achieve better contact between the membrane and CL. Industrially, a decal process is more often employed that coats the CL onto an inert Teflon[®] substrate from where the CL can be transferred to a membrane through hot-pressing.^[9] This process avoids membrane deformation during the spraying process that occurs due to swelling in contact with the solvents and can be inconsistent across the whole membrane, hence leading to lower-quality MEAs. With a decal process, however, the CL can be produced with roll-to-roll processes, which allow for a high-throughput industrially coating process with consistent MEA properties. Besides the approach to coat the CL on the membrane, another one gained prominence where the CL is applied on the GDL or PTL resulting in a gas-diffusion electrode (GDE) or porous transport electrode (PTE), respectively.^[89,99,103,104] This promises better electrical conductivity between the CL and GDL/PTL by direct contact between them across the whole surface. Especially in the field of PEMWE it

was discovered that a low electrical conductivity of the catalyst leads underutilized parts of the CL without direct contact to the PTL.^[93,95,105] The downside of this approach is that the CL morphology is very dependent on the GDL/PTL morphology and catalyst can penetrate in its pores isolating it from the ionomer network, hence lowering catalyst utilization.

Composition Gradient CCMs Standard CLs show a homogeneous distribution of its constituents in all spacial directions in ideal conditions. This approach reduces complexity during its manufacturing process, but can lead to negative performance impact or reduce its efficiency. The reaction does not take place everywhere in the CL at the same time and the reaction front can shift based on materials used as well as operation conditions.^[46,106] Hence, in an homogeneous layer, the catalyst might be underutilized and thus reduces its mass efficiency and increases its CAPEX. The downsides of homogeneous material distribution can impact all CL properties as the pore volume might induce mass transport limitations in some parts of the layer while it does not offer sufficient surface area in others. The reaction rate follows local overpotential variations, allowing for an optimization based on these different overpotential.^[14,107]

To alleviate some of these drawbacks, the electrode can be varied in its composition in different dimensions based on the type of material that is distributed. Figure 3.2.2 illustrates three of these approaches with Figure 3.2.2.a showing a patterned electrode, that changes in catalyst composition based on the channel of the flow field. Most of the reactant and product transport takes place directly underneath the channel of the flow field. At low potentials, the reaction rate is highest at the edge of the channel, where the diffusion paths of the electrons are shortest to the land while sufficient reactions are supplied by the channel.^[14] However, at higher potentials the local highest reaction rate shifts to the channel, where reactants and products can be transported more easily, leading to lower mass transport overpotential. With a higher concentration of catalyst material, the area underneath the channel could thus improve the cells efficiency by increasing the catalysts utilization. This effects, however, have to be tailored to the application of the cell as the optimal distribution shifts with operation conditions. Additionally, the electrical conductivity of the catalyst has to be taken into account, as the area underneath the channel is quite far from the electron pathways through the land and a poorly conductive catalyst leads to higher ohmic overpotential in this area. It was calculated that the maximum reaction rate for a relatively poorly conductive IrO_x catalyst takes place underneath the land while it was underneath the channel for a better conductive Ir metal catalyst.^[95] Besides the catalyst loading, a gradient of poros-

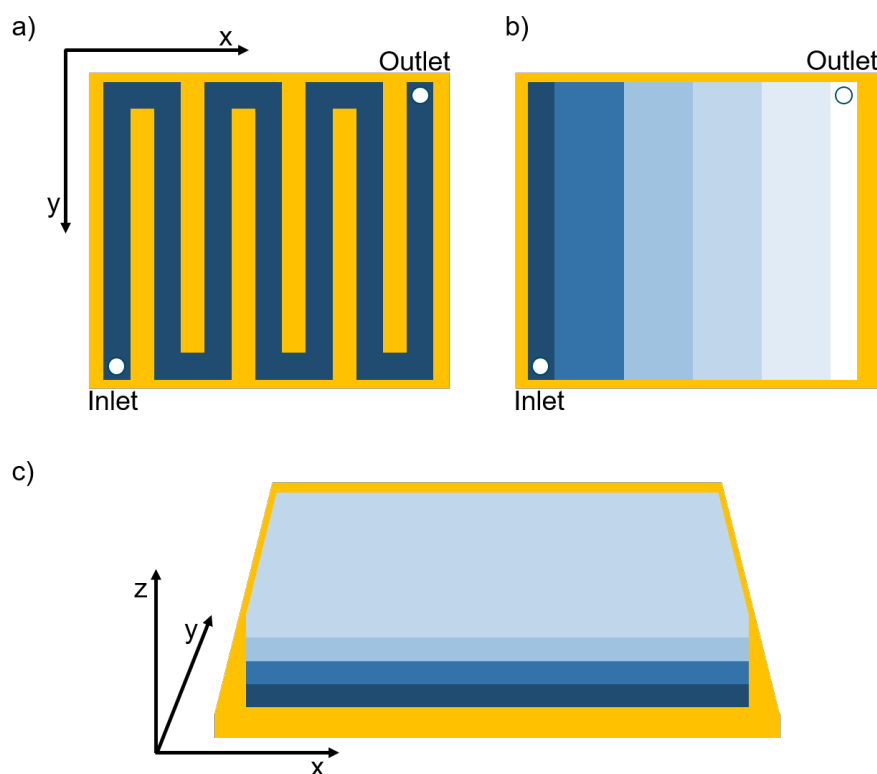


Figure 3.2.2: Schematic representation of a) the electrode patterning following the cells flow field, b) a gradient in x-y direction from inlet to outlet of the flow field, and c) a gradient in z direction of the CCM with the composition gradient indicated in blue shading.

ity could be introduced underneath the channel, through pore-formers or varying deposition parameters, to allow for more pore volume and reduce mass transport overpotential to the area underneath the land.^[14] In general, this approach mainly alleviates mass transport overpotential and therefore leads to higher performance.

Another gradient approach, focusing on the mass transport properties of the CCM, involves changing the distribution of its composition in the in-plane direction (Figure 3.2.2.b) based on the reactant/product ratio. In this approach, reactants are introduced at the inlet of the flow field and react to form products, which increase in concentration towards the outlet. In an homogeneous setup, this leads to an anisotropic distribution of the reaction, with higher reaction rates near the inlet due to an abundance of reactants and no blocking of product pathways.^[15] However, this uneven distribution lowers the utilization of catalysts as the reaction rate decreases near the outlet. To address this issue, a gradient of catalyst loading can be introduced, with lower loading near the inlet and higher loading near the outlet to homogenize the reaction rate across the entire cell.^[15,16] Achieving a more homogeneous reaction rate also increases the lifetime of the cell, as catalyst par-

ticles across the entire CL experience similar potentials, unlike in homogeneous CLs. Interestingly, an improved cell performance can also be observed with a reversed gradient, where high catalyst loading near the inlet homogenizes the reactant concentration along the flow length, rather than the reaction rate.^[108] The effect of gradients in the reactant depletion direction strongly depends on the reactant supply and operation potential and it becomes more pronounced in fuel cells due to the intricate management of product water and reactant gases, unlike in PEMWE cells. In most cases, the PEMWE cell is flooded with water, indicating no reactant gradient along its channel length. Only mass transport limitations through the product gases can result in overpotential. However, at low inlet water fluxes relative to the consumed water, dehydration of the membrane and ionomer can become an issue. This can be counteracted by designing a gradient that adapts certain CCM properties based on the local water content or rather the stoichiometric water ratio.^[109]

The composition gradient approach in the z-direction or the thickness of the CL (Figure 3.2.2.c) has been extensively studied for fuel cell applications, involving variations of multiple parameters such as ionomer loading, catalyst loading, and pore sizes. Various studies have explored the Pt content variation on the support material to address underutilization of the active material.^[110–114] As the distance from the membrane increases, the relative ionic resistance of the ionomer also increases, resulting in higher ionic overpotential and dampened reaction rates. However, with a lower concentration of Pt particles, this underutilization is reduced, leading to an overall improvement in cell efficiency. Ye *et al.* also demonstrated that a porosity gradient, achieved by adding a filler material to the outer layer, results in higher volume between particles and similarly addresses underutilization through this hierarchical pore system.^[107,112] The variation in pore size distribution and catalyst loading primarily impacts areas with high current density, where the reaction rate is high and mass transport overpotential become dominant. In a fuel cell setup, the interplay between reaction rate and reactant transport is crucial, unlike in a PEMWE setup where an oversupply of reactant is preferred. Lowering the humidity of reactant gases can lead to a more homogeneous reaction rate throughout the CL, improving its performance and enhancing the positive effects of grading.^[115] Studies by Nguyen *et al.* and other groups have shown that variation in ionomer loading, such as a linear gradient across the thickness, can improve performance.^[114–120] By increasing ionic conductivity near the membrane, the reaction rate at that location can be enhanced, and a more uniform temperature distribution can be achieved.^[119,120] The overall performance increase can be substantial, as demonstrated by Xing *et al.*, who observed

a 16 % performance increase and a 47 % reduction in Pt usage.^[119] Different material gradients address similar overpotential within the CL and it has been shown that an already improved gradient CL may not benefit from further optimization. Studies have indicated that either a catalyst or ionomer gradient alone might be sufficient, as the performance did not increase further with simultaneous grading.^[114] Although the concept of through-plane gradients has not yet been applied in a PEMWE setup, it holds promise, as numerous performance increases have been observed in fuel cells. As some of the challenges in fuel cells, such as water management and temperature control, are alleviated in PEMWE, the optimization of ionic, ohmic, and mass transport overpotential can be explicitly applied.

4 Methods

4.1 Electron Microscopy

Transmission electron microscopy (TEM) This technique allows for imaging of thin samples at much higher resolutions than with light microscopy.^[121,122] An electron beam is directed at the sample, and the electrons passing through without colliding and scattering are detected. Through the discrimination of scattered and unscattered electrons, a gradient is observed, producing a grayscale image. The scattering probability depends on the mass of the element and sample thickness, and thus different elements create different contrasts in the image. The resolution of this technique depends on the acceleration of the electrons since their de Broglie wavelength corresponds to their momentum through wave-particle duality.^[122] With higher acceleration, a shorter wavelength, and thus higher resolution can be achieved. At very high resolutions, individual crystal planes can be identified, and even singular atoms in some cases. This microscopy technique is especially suited for analysis of nanoparticle catalysts as the high resolution can image individual particles and their morphology can be evaluated. The contrast in the final image is dependent on the electron density of molecules and atoms and thus also the molecular weight of the element, which allows for identification of different components of a catalyst and to distinguish between active catalytic particles and substrates. Especially the evaluation of particle sizes is of special importance as this could directly influence the catalyst activity. For additional investigation, energy dispersive X-ray spectroscopy (EDS) can be used to determine the sample's specific element composition and map these signals to a TEM image.^[121] Through the interaction of irradiated electrons and lower-orbital electrons, X-rays are emitted, which have an element-specific wavelength that is detected in EDS. This can be used for a spatially resolved elemental composition, where specific elemental ratios can be assessed based on their position in the image. Thus, individual particles or structures can be characterized based on their elemental composition.

Scanning electron microscopy (SEM) In contrast to TEM, which employs a stationary electron beam, this technique employs a modulated electron beam in the x- and y-directions, producing a so-called raster scan across the sample.^[122] Through the irradiation of electrons, the samples undergo certain processes, which are recorded in the detector, thus generating an image of the sam-

4.2 X-ray Techniques

ple. Different detectors allow for the observation of different processes, which most often include the detection of secondary electrons and backscattered electrons. Secondary electrons are emitted through the inelastic scattering of impacting electrons, whereas backscattered electrons are elastically scattered in the sample and ejected again without substantial energy loss. The penetration depth of incoming electrons and the emission depth of the secondary electrons depend on the acceleration of the electron beam and follow a circular shape inside the material, as the electrons also propagate laterally inside the sample, as displayed in Figure 4.1.1. In conjunction with SEM, an ion-beam technique is often used,

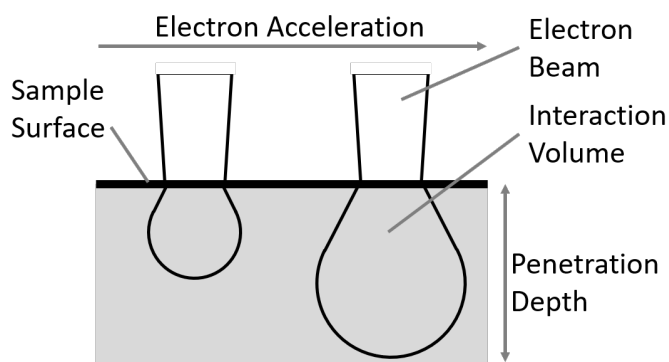


Figure 4.1.1: Schematic representation of the penetration depth and propagation volume inside the sample in SEM.

which bombards the sample with high-energy ions to manipulate the sample and dispatch layers, for example allowing for cross-sectional analysis.^[123] Generally, Ga atoms are used as ions, but recently He atoms were also employed, which allows for higher resolution of the ion beam.

In contrast to TEM, SEM allows for the evaluation of larger samples and constructs, such as microchips or biological samples and most importantly for this work MEAs and catalyst layers.^[123] The analysis of MEA cross-sections can be used to determine layer thicknesses, morphology as well as homogeneity, or elemental mapping in conjunction with EDS. Specifically the elemental mapping of different species within the catalyst layer is of special interest in this work, as it allows for exact determination of material gradients within the CL.

4.2 X-ray Techniques

X-ray diffraction (XRD) The diffraction of a monochromated X-ray beam on electrons in a sample can be used to identify crystalline domains in powders and single-crystals.^[124,125] The X-rays' wavelength is similar to the plane distances be-

tween crystal planes and thus are diffracted on them. This leads to interference depending on the exact separation of the planes. The planes of a crystal are indicated by Miller indices with their corresponding hkl values and describe the geometry of the crystal cell. According to Bragg's Law (4.1), the path lengths of two parallel incident beams on crystal planes are different depending on the incident or glancing angle of the beams, as schematically depicted in Figure 4.2.1. The

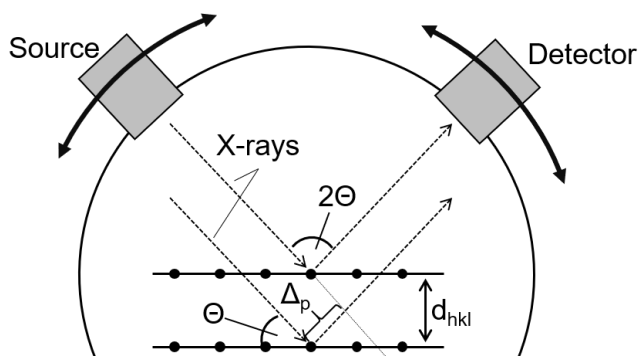


Figure 4.2.1: Schematic representation of the diffraction of X-rays on crystal planes along with the Bragg-Bretano measurement arrangement on the outer circle.

separation of crystal planes (d_{hkl}) can thus be determined by finding the glancing angle (Θ) at which the path-length difference (Δ_p) is an integer of the beam's wavelength (λ). Here, the beams interfere constructively and a signal can be detected.

$$\lambda = 2 d_{hkl} \sin(\Theta) \quad (4.1)$$

For the determination of crystalline domains in powder samples as opposed to single crystal samples, the Bragg-Bretano geometry is most often used for the X-ray source and detector.^[124,125] Here, either the source or detector can be rotated around the flat-pressed sample to scan through different Θ and thus identify different crystal planes. The sample is additionally rotated to gather information in all viewing angles of the circular sample. The analysis of the gathered diffractograms also allows for sophisticated data fitting, such as Rietveld refinement, which can be used for specific quantification of crystalline domains within a sample, or the application of Scherrer analysis, which can help to calculate the sizes of crystalline domains. Especially the Scherrer equation is of use in this work as it can be used to estimate the particle size of metallic and thus crystalline particles as well as the approximate degree of crystallinity for different species.

X-ray photoelectron spectroscopy (XPS) Non-destructive analysis of a sample surface can be achieved by irradiating it with monochromatic X-rays and analyzing the emitted photoelectrons.^[126] The photoelectric effect occurs when X-rays are absorbed by electrons in the atomic and molecular orbitals of the sample, leading to the emission of these electrons. The kinetic energy (E_{kin}) of the emitted electrons is determined by the binding energy (E_B) of the electron in its orbital, as described by Equation 4.2.^[126,127] By analyzing the kinetic energy, the presence and quantity of those electronic states can be studied.

$$E_B = h\nu - E_{kin} - \Theta_s \quad (4.2)$$

Here, E_B is defined by the energy of the irradiated X-rays as described by its wave frequency (ν) along with Planck's constant (h) and the spectrometer work function (Θ_s). The escape depth of emitted electrons without energy loss through inelastic collisions is determined by the element-specific mean free path and is usually around four to eight atomic layers.^[126] At larger depths, the probability to be emitted from the sample without any energy loss becomes so low that the detection is unlikely compared to surface-emitted electrons. Depending on the main quantum number of the orbital from which the electron is emitted, it can experience spin-orbit splitting, which occurs for p-, d-, and f-orbitals. This leads to a doublet splitting of the resulting signal according to the total angular momentum quantum number of the electron, with a specific intensity ratio of the main and trailing signal corresponding to the degeneracy of the state. Depending on the specific electronic environment around an atom, the E_B shifts slightly to positive or negative values. Through this effect, the chemical environment around the atom can be examined, and specific oxidation states and even molecular bonds can be identified. This also allows a quantitative analysis of the different species and oxidation states relative to each other.

4.3 Other Physical Characterizations

Inductively coupled plasma (ICP)-mass spectrometry (MS) The principle of MS lies in the ionization of atoms or molecules and subsequent separation by their mass-to-charge ratio. Of special importance here is the variant with an ICP used to ionize the sample and is especially useful for trace metal analysis.^[128] It employs a noble gas plasma, most often Ar, in order to fragment compounds in the sample and analyze individual atoms. The sample is inserted in liquid form with dissolved ions of the target species and vaporized prior to introduction to the

plasma. The formed ions are then guided through ion lenses and optics in order to obtain a stable ion beam, which is then separated in a quadrupole according to the ion's mass-to-charge ratio and then detected. A schematic of this process is displayed in Figure 4.3.1. In order to calculate the concentration of the ele-

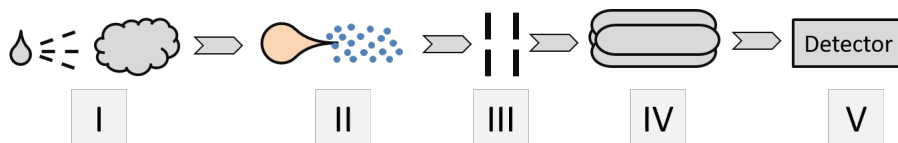


Figure 4.3.1: Schematic representation of the analysis stages for concentration determination via ICP-MS with (I) representing the vaporizer, (II) representing the plasma ionization, (III) representing the ion optics and lenses, (IV) representing the quadrupole splitting and (V) representing the detector.

ment based on the signal intensity in the detector, a device calibration has to be carried out prior to measurement. Here, several stock solutions of known concentration are measured and correlated with the signal in an interpolation with which the sample signal can be associated. The analysis of catalysts via ICP-MS often requires a chemical digestion step, prior to the measurement, as the catalyst species have to be dissolved in order to be analyzed. Especially for noble metals this can pose quite a challenge as metals, such as Pt and Ir, tend to be very stable and require very harsh digestion methods. For example, the digestion of Ir needs to be carried out in aqua regia and under elevated pressure at high temperatures, above 200 °C, which can pose challenges in the experimental setup to reach these conditions.

Thermogravimetric analysis (TGA) The heating of a sample in different environments while observing the weight change can confer information about different characteristics of a sample, such as the uptake of humidity and decomposition or oxidation of species.^[129] The temperature increase can be carried out under different atmospheres to observe different phenomena and it can be extended by further analysis techniques downstream to study decomposition products in the gas atmosphere. Especially, the usage of MS or infrared detectors can yield substantially more information about the decomposition products and complex mixtures can be characterized. In this thesis, the technique is mainly used to study the decomposition of Nafion[®] and oxidation of Ir species in an oxygen atmosphere. Nafion[®] decomposes, when heated in an O₂ atmosphere, mainly to CO₂ and other products containing F and S species. The weight difference during the decomposition of Nafion[®] can thus be used to determine the ionomer content in CLs.^[89,99]

4.4 Electrochemical Techniques

Three electrode setup with a rotating disk electrode (RDE) The electrochemical properties and performance of catalyst materials can be assessed in an aqueous model system with liquid electrolyte and a thin film of catalyst on a disk-working electrode (WE).^[23,130,131] The WE in this technique is rotating, which induces predictable electrolyte flow around the disk, as shown in Figure 4.4.1. This enables reproducible transport phenomena around the WE, leading to loca-

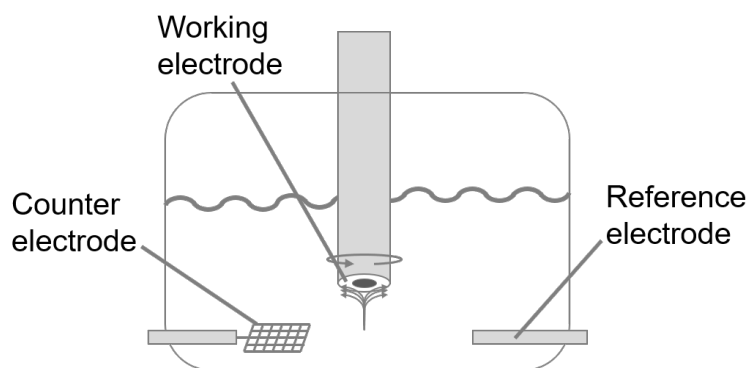


Figure 4.4.1: Schematic representation of the RDE setup.

tion independence of the measured current, as the catalyst film operates under steady-state conditions. Due to the laminar flow around the WE, a diffusion layer is formed that only depends on the WE's rotation speed and thus excludes mass-transport limitations from the measurement and reduces these to diffusion limitation.^[132] This technique thus allows for accurate determination of kinetic properties of the catalyst in a low potential area but is limited by diffusion limitation at higher ones.^[132,133] For investigations of fuel cell catalysts, this limitation is more pronounced as the diffusion of the O₂ educt is rather slow in liquid electrolyte and a diffusion limitation plateau is formed.^[133,134] This limitation is not dominant for electrolysis catalysts but the formed gas products could stick to the catalysts as bubbles and reduce the available surface of the catalyst or lead to additional detrimental effects.^[134] This is particularly the problem when evaluating powder samples, as the bubbles tend to form inside pores of the material, where a shedding is less probable and the blocking of active sites becomes more likely. Thus, special care has to be applied when characterizing these catalysts as the film thickness and composition on the electrode is important for alleviating this issue. The RDE technique can also be used in conjunction with other analysis methods, such as electrolyte analysis via MS for the determination of dissolved species in stability evaluations.

Electrochemical impedance spectroscopy (EIS) One technique of special importance to disseminate different processes during the PEMWE operation is EIS.^[135] Here, a sinusoidal perturbation of either the current or potential is applied with different frequencies and the response signal is analyzed, as seen in Figure 4.4.2.a.^[23,135] The frequency-dependent perturbation thus allows for a temporally resolved analysis of different processes taking place at different time scales. The overall measured impedance (Z) can be separated into its real part of the impedance (Z') and imaginary part of the impedance (Z'') representing the resistive contribution and phase shift of the alternating signal, respectively.^[23] A common form of analysis for impedance data is the Nyquist plot, where Z' is plotted against Z'' , schematically depicted in Figure 4.4.2.b. Here, the signal forms half circles for different processes in the optimal case. These half-circles pertaining

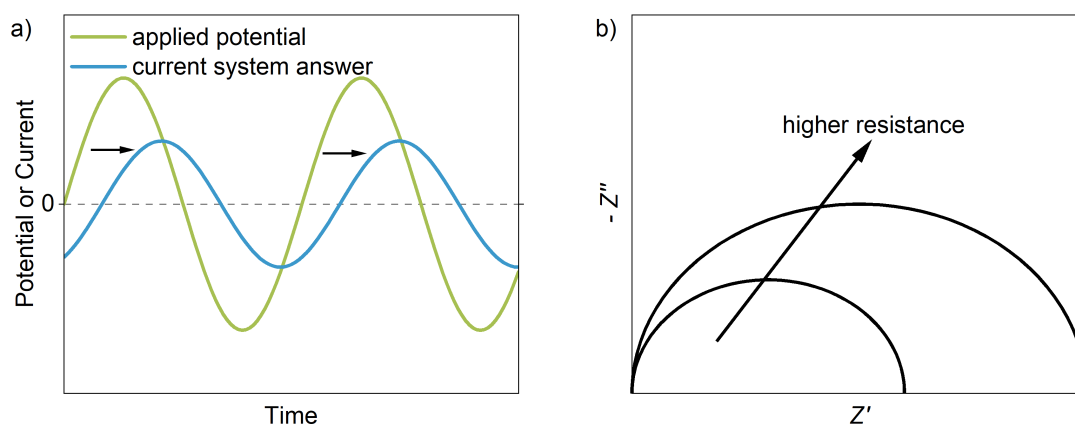


Figure 4.4.2: Schematic depiction of a) the applied sinusoidal signal with its corresponding answer signal and b) an exemplary Nyquist plot with half-circles of processes with different resistances.

to different processes can be fitted with equivalent circuit models and thus individual resistive contributions can be calculated. Each process can be depicted by an electrical element proxy, that can describe the conversion of the applied current or potential to the system answer and be varied in its parameters to yield a resistance value for each process. These electrical elements can consist of a simple resistor, constant phase element, or an inductor and can be put into serial and parallel circuits to better mimic each process. The challenge is that different equivalent circuit models can model the EIS data and distinguishing between processes with too many individual circuit elements can become non-trivial.

Besides the modeling with equivalent circuits, the data can also be analyzed through the distribution of relaxation times (DRT).^[135,136] This yields information about the overall contribution to the total impedance of individual processes re-

solved along a time constant for each one. DRT thus allows for analysis of the system without knowledge about the exact system but requires high-quality data for accurate calculations. The time-dependence of the impedance data can be extracted using discretization, often a Gaussian function, and Tikhonov regularization, which makes the analysis dependent on chosen parameters.^[135] These are the FWHM-coefficient (m), determining the peak's width and the Tikhonov regularization parameter ($\lambda_{Tikhonov}$), that impacts the number of observed peaks, which can easily under- or overestimate the number of processes calculated. The resulting spectrum of DRT process-associated resistance ($\gamma(\tau)$), corresponding to its time constant (τ), is inversely related to the frequency at which the process takes place. Parameters have to be carefully chosen in regards to other evidence of the processes and compared to literature values as the estimation of DRT spectra can be ambiguous without rigorous analysis.

The catalyst layer ionic sheet resistance (R_{ion}^{CL}) of either anodic or cathodic CLs can be determined by analysis of EIS spectra, that are recorded in a non-faradaic potential area. Here, the capacitive contribution to $Z(f)$ can be observed at low frequency (f), where Z' converges to one value and a vertical impedance arc can be observed in the Nyquist-plot.^[10] The total impedance can be described by equation 4.3.

$$\lim_{f \rightarrow 0} Z(f) \approx \frac{R_{ion}^{CL}}{3} + \frac{1}{j C_{DL} f} + \text{HFR} \quad (4.3)$$

Here, R_{ion}^{CL} is defined by the imaginary unit number (j), the double layer capacitance (C_{DL}), and the high-frequency resistance (HFR), which corresponds to the Z' value at zero Z'' , namely the x-intercept of the Nyquist-plot. At the phase minimum of the measurement, the transition of the 45° to the 90° , namely the transition to the capacitive behavior begins. Here, R_{ion}^{CL} can be determined graphically by finding f at this phase minimum and the corresponding Z' value, corrected by the HFR.^[10]

Cyclic voltammetry (CV) In order to characterize the redox processes in a catalyst, CV can be used to discern between different transitions of oxidation states, based on the applied cell potential. Usually, a certain potential range is scanned with a fixed scan rate (r) in a triangular wave and each redox process impacts the measured current density at each potential. Besides the redox processes, a double layer charging occurs, elevating the baseline of each redox signal. Here, this technique is foremost used to determine the electrochemical surface area

(ECSA) of the Ir-based catalysts, which can be categorized in two groups, that require different ECSA determinations. First, on metallic Ir, a hydrogen underpotential deposition (H_{upd}) process takes place, where a single atomic layer of H is adsorbed on Ir sites and the total charge of this process can be correlated with the ECSA based on a metal-specific charge density of H on Ir (q_{Ir}), according to equation 4.4.^[91,137]

$$\text{ECSA} = \frac{Q_{H_{\text{upd}}}}{r q_{\text{Ir}} A_{\text{electrode}} L_{\text{Ir}}} \quad (4.4)$$

Here, the ECSA is defined the electrode area ($A_{\text{electrode}}$), and the Ir loading (L_{Ir}) with a q_{Ir} value of $179 \mu\text{C cm}^{-2}$ for metallic Ir. The underpotential deposition process takes place here at potentials below the equilibrium potential given by the Nernst equation as the interaction between the H and metal interface is energetically favorable, allowing a monolayer of H to adsorb on the surface easily. Second, oxidic Ir species do not show H_{upd} peak, which is why the ECSA determination is less trivial.^[138] Here, the mass-specific charge (q^*) is used as a proxy for the oxidic Ir sites, where the redox peak in the potential area between 0.4 and 1.2 V is assumed to stem from oxidic Ir species, as depicted in Figure 4.4.3. This signal emerges when metallic Ir surface is oxidized, as described by Zhao *et al.*^[138] Since this approach only works for non-supported catalysts, the q^* for supported

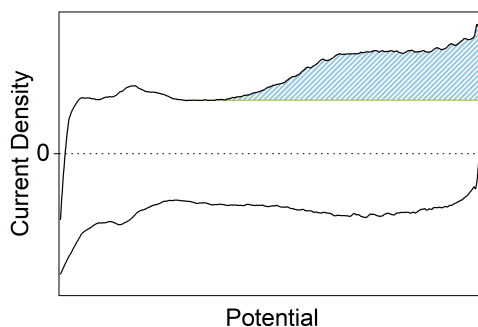


Figure 4.4.3: Schematic depiction of a CV of an oxidic Ir catalyst with indicated oxidic Ir charge used to determine q^* in blue.

catalysts in this work has to be compensated for C_{DL} of the support material. Thus, the minimum current density signal between 0.3 and 0.4 V is assumed to be solely caused by double layer charging and is subtracted from the oxidic Ir charge.

5 Experimental

5.1 Catalyst Synthesis

ATO The ATO material synthesized here was used as the support for all following Ir-based catalysts. The method was adapted from Hartig-Weiss *et al.* and also described in Gollasch *et al.*^[84,139] First, pure Sn granules (42.25 mmol, 5.0 g, Carl Roth), Sb₂O₃ (1.1 mmol, 325 mg, Carl Roth) were added to a solution of concentrated HNO₃ (75.0 mL, 65 vol.%, Carl Roth) and pure water (125.0 mL) for a nominal doping of 5 wt.% (Sb:Sn). During the initial addition of the solid materials, nitric fumes were produced, due to the formation of a colloid, hence the addition was performed in a fume hood with caution. The mixture was added to a 250 mL polytetrafluoroethylene (PTFE) autoclave liner (*DAB-2*, Berghof) and stirred for 15 min. Then, the autoclave was sealed and heated to 140 °C for 10 h. When the autoclave cooled down to room temperature, it was slowly unsealed in a fume hood in case nitric fumes were produced. The light blue powder was then washed several times with pure water to reach a neutral pH and then additionally 2 times with ethanol. Afterward, it was calcined in air atmosphere, to increase its electrical conductivity, in a laboratory oven (*P330*, Nabertherm) at 600 °C (3 °C min⁻¹) for 3 h to produce a dark blue powder.

Reduction synthesis (RS) This synthesis method employs the impregnation of the support material and subsequent chemical reduction with NaBH₄, as described by Wang *et al.*^[140] Additionally, a structure conducting surfactant was added to restrict particle growth of the forming metallic Ir nanoparticles. The reaction requires an inert gas atmosphere, in order to protect the NaBH₄ from decomposition through hydrolysis. All chemicals and materials used in this method have been dried before usage and it was carried out in a nitrogen atmosphere glove box. In a typical synthesis for a 40 wt.% Ir on ATO catalyst (different loadings are displayed in Table A.1), anhydrous absolute ethanol (min. 99.9 vol.%, CHEM-SOLUTE), which was previously dried under 3 Å molecular sieve (TH Geyer) for 3 d, was mixed with ATO (170 mg) and cetyltrimethylammonium bromide (CTAB) (4.82 mmol, 1.755 g, Carl Roth). This mixture was stirred for 30 min before the addition of IrCl₃ x H₂O (0.59 mmol, 212 mg, Alfa Aesar), dissolved in anhydrous ethanol (50.0 mL). To ensure sufficient impregnation of the ATO with the precursor, this suspension was stirred overnight. Then, NaBH₄ (7.66 mmol, 290 mg, Sigma Aldrich) was dissolved in anhydrous ethanol (50.0 mL) and added drop-wise to

the ATO suspension. The mixture was stirred for 4 h, while slowly changing its color to black, indicating the formation of metallic Ir particles. Afterward, the reaction was quenched with pure water, and the solids were separated by centrifuging (7000 rpm, 5 min, *Centrifuge 5430*, Eppendorf). These were washed multiple times with pure water and absolute ethanol. The resulting powder was then dried in air at 70 °C.

In order to investigate the viability of this method under air atmosphere, the method was carried out as described before but without drying the materials or chemicals. To stabilize the NaBH₄, NaOH (1.0 M, 10 mL, AppliChem) was added to the NaBH₄ solution before adding it to the ATO suspension.

Modified Adam's fusion (MAF) The Adams Fusion or modified Adams Fusion method is a variant of the original synthesis of Pt oxides by Adams *et al.* involving the oxidation of a noble-metal precursor in a melt of NaNO₃.^[141] This method was adapted for Ir-based catalysts and described by Böhm *et al.* for support-based Ir catalysts with limited particle growth due to a relatively low reaction temperature compared to similar methods.^[74,142,143] The postulated Ir species formed here is a tetragonal IrO₂. In a typical synthesis for a 40 wt.% Ir on ATO catalyst (different loadings are displayed in Table A.2), IrCl₃ x 3 H₂O (3.81 mmol, 137.0 mg) and NaNO₃ (35.30 mmol, 3.0 g, Carl Roth) were dissolved in pure water in a molar ratio of 1:12.24 and mixed with the ATO support (110 mg). The suspension was then stirred for 3 h and subsequently horn-sonicated for 10 min. Then, it was transferred to a crystallizing dish and bath-sonicated at 80 °C until dry. The dry reaction mixture was ground to a fine powder and heated in a laboratory oven to 150 °C (3 °C min⁻¹) for 2 h, to ensure all remaining water evaporated before the reaction, and then to 375 °C (3 °C min⁻¹) for 1 h. Finally, the product was washed several times with pure water and dried in air at 70 °C. The reaction was also carried out with commercial Ir black (1.30 mmol, 250 mg, *Ir mohr*, Umicore) instead of the IrCl₃ precursor. This was performed to assess the influence of the oxidation of this synthesis on metallic Ir particles.

Colloidal deposition (CD) and Hydrothermal deposition (HTD) For the deposition of an Ir particle colloid a dispersion of particles was first synthesized by the thermal reduction of Ir precursor in ethylene glycol as described by Abbou *et al.*^[144] This colloidal suspension was then further used in both the colloidal deposition and in the hydrothermal deposition. In a typical synthesis of the colloid, a 6.95 mg_{Ir} mL⁻¹ H₂Cl₆Ir x H₂O (0.147 mmol, 60 mg, CHEMPUR) solution was prepared by dissolving it in pure water. This solution (8.6 mL) was then added to

a mixture of ethylene glycol (120 mL, Carl Roth) and pure water (60 mL). To this, NaOH solution (0.5 M in 1:1 ethylene glycol and water) was added until the pH reached 12 and the color of the solution changed to a pale yellow. The solution was then purged with Ar for 10 min, held in Ar atmosphere, and heated to 160 °C for 4 h while refluxing. During this, the Ir precursor got reduced and an Ir colloidal suspension was formed, which turned the color of the solution from yellow to a dark brown.

This suspension was then further processed in two different deposition methods. First, for colloidally deposited catalysts with a nominal loading of 40 wt.% Ir on ATO (different loadings are displayed in Table A.3), ATO support (43 mg) was suspended in a ethylene glycol (10 mL) and pure water (10 mL) mixture and colloid suspension (180 mL) was added. To this, H₂SO₄ solution (1.0 M in 1:1 ethylene glycol and water, Carl Roth) was added until the pH of the solution reached 1. Through the added acid, the Ir intermediates are supposedly condensed and the IrO_x particles are deposited on the support.^[145] This mixture was stirred for 3 d and the solids were separated by centrifuging. The powder was then washed several times with pure water and finally dried in air at 70 °C.

The hydrothermal deposition method employs a further reduction of the colloidal intermediates through thermal treatment in *tert.*-butanol to supposedly bind the particles stronger on the support material, as described by Böhm *et al.*^[146] In a typical synthesis for a 40 wt.% Ir on ATO catalyst (different loadings are displayed in Table A.4), ATO (160 mg) was added to pre-warmed *tert.*-butanol (30 mL, Thermo Fisher Scientific) in a 250 mL PTFE autoclave liner. Then, previously prepared Ir colloidal suspension (190 mL, 0.147 mmol_{Ir}) was added and the autoclave was sealed. While stirring the mixture, the autoclave was heated to 175 °C for 12 h and then passively cooled to room temperature. The resulting suspension was then separated by centrifuging and the solids washed several times with pure water after which the powder was dried in air at 70 °C.

Post-synthesis heat treatment In order to convert metallic Ir and suboxidic IrO_x particles to a IrO₂ form to investigate the difference in electrochemical stability, the RS, CD and HTD catalysts were further heat treated in air atmosphere. The oxidation temperature was chosen to coincide with the reaction temperature of the MAF method in order to provide some comparability. The catalysts were heated in a laboratory oven in air atmosphere to 375 °C (3 °C min⁻¹) for 1 h. After the temperature hold, the sample was allowed to cool to room temperature without any heat source.

5.2 CCM Preparation via Ultrasonic Spray Coating

Catalyst suspension For the coating with an ultrasonic spray coater, the catalysts were suspended in a mixture of different solvents along with an ionomer that acts as a proton-conducting medium as well as a binder. Different catalysts require specific solvent mixtures for a viable suspension and all solvent mixtures for each catalyst are given in Table 5.2.1. In a typical suspension preparation, the catalyst powder was first mixed with the appropriate solvents. Then the suspension was bath sonicated for 30 min, while cooled in an ice bath. After initial sonication, the Nafion[®] ionomer (5 wt.% 1100 equivalent weight solid polymer in aliphatic alcohols, Sigma-Aldrich) was added drop-wise while bath sonicating the suspension. The amount of ionomer depends on the specific desired composition of the catalyst layer but it generally varied between 5 and 30 wt.% of the solids in the suspension. After ionomer addition, the suspension was bath sonicated for an additional 15 min and then horn-sonicated for 15 min with a pulse sequence of 10 s on and 10 s off in an ice bath to avoid solvent evaporation. Finally, the suspension was stirred on a roll-mixer (*RS-TR 10*, Phoenix Instrument) for approximately 30 min to equilibrate to room temperature from the ice bath. The prepared suspensions were either used freshly prepared or kept stirring until used.

Table 5.2.1: Solvent composition for different catalyst materials with solvent ratio of the resulting solvent mixture and solid ratios of the resulting suspension.

Catalyst	solvent 1	solvent 2	solvent ratio / wt.%	solids in suspension / wt.%
Ir black	tetrahydrofuran	2-propanol	50 / 50	1
Ir- and IrO ₂ /ATO	water	2-propanol	50 / 50	1
Pt/C	water	ethanol	85 / 15	20

Coating procedure and treatment The coating of membranes with catalyst suspension was carried out on an *ExactaCoat* (Sonotek) ultrasonic spray coater. This device was additionally equipped with an ultrasonic syringe to keep the suspension agitated during the prolonged coating process and to avoid particle settling in the reservoir. In a typical coating process, a Nafion[®] membrane (Nafion[®] NR212, Chemours) was cut to the appropriate size and fixed in either a 5 cm² or 25 cm² steel mask. The heating plate was then heated to temperatures be-

tween 40 and 100 °C, depending on the desired CL properties. The suspension was filled into the reservoir and sprayed through a 120 kHz ultrasonic nozzle in a corner-alternating serpentine pattern onto the membrane. It was pumped through the nozzle at 0.3 mL s⁻¹ with a conical nitrogen shaping gas stream. The weight of the resulting CL was monitored by coating aluminum foil with the same mask in the same process. It was regularly weighted and this material was monitored instead of the membrane directly due to the swelling of the polymer and subsequent vast variations in weight. After the coating on both sides, the double-sided CCM was hot-pressed (*PW20H*, P/O/Weber) to increase the contact between CL and membrane. Here, the CCM was pressed for 5 min at 125 °C and under the pressure of 5 MPa.

5.3 Electrochemical Characterisation

RDE setup Electrochemical measurements in an aqueous model system were carried out in a 3-electrode setup in acidic medium. All measurements were performed in a glass cell, which was chemically cleaned prior to use by submersion in a mixture of concentrated sulphuric acid and concentrated hydrogen peroxide to remove any organic or inorganic contaminants. The cell remained submerged for 24 h, was rinsed with pure water repeatedly afterward, and placed under pure water between measurements to avoid contamination from ambient air. As the working electrode, a gold disk with a PTFE shroud (Pine Research) and an active surface area of 0.2475 cm² was used in all measurements. Prior to each measurement, the electrode was cleaned by polishing first with 1.0 µm and second with 0.05 µm aluminum oxide abrasion suspension (*MicroPolish 40-10081*, BUEHLER) for 5 min and subsequent ultrasonication in pure water. In addition to the working electrode, either a Pt wire or graphite rod counter electrode, separated from the electrode department by a glass frit, was used in conjunction with a RHE (Mini-hydroflex, gaskatel). For a typical catalyst suspension, catalyst powder (3.5 mg) was suspended in pure water (7.6 mL), 2-propanol (2.4 mL) and Nafion[®] solution (20 µL, 5 wt.% 1100 equivalent weight polymer in aliphatic alcohols, Ionpower) by horn-sonication for 15 minutes, while cooled in an ice bath, and then mixed with a roll-mixer. The suspension (10 µL) was then dropped on the working electrode while rotating at 100 rpm, which was then increased to 600 rpm until the electrode film was fully dry. For stability measurements, the concentration of the catalyst suspension was doubled and the suspension applied twice to the working electrode, resulting in an applied volume of 20 µL. This increase in catalyst mass was performed to ensure sufficient catalyst material for dissolution

measurements. For measurements, the working electrode was submerged in the electrolyte while rotating at 2400 rpm to avoid air bubbles blocking the catalyst film. In a typical measurement, the electrolyte consisted of 0.5 M aqueous H_2SO_4 (*Titripur* quality, VWR). In addition to the in-house synthesized catalysts, reference catalysts have been characterized with this technique. The two used are commercial Ir black and commercial IrO_2 (*Elyst Ir75 048C*, Umicore).

Potentiostatic control of the cell was established with a *PG-STAT128N* (Metrohm Autolab). The electrochemical testing protocol can be divided in a protocol to determine the activity of the catalyst and one to determine its stability. A typical activity determination consisted of activation of the catalyst to generate fresh surfaces on the Ir and to oxidize metallic Ir to its active species. Here, a potential of 1.6 V vs. RHE was applied for 10 min. Afterward, an EIS measurement was carried out at 0.35 V vs. RHE with an amplitude of 10 mV in a frequency range of 100 kHz to 0.1 Hz. The system's Ohmic resistance (R_{Ohm}) was determined through this EIS measurement by determining Z' at zero Z'' , namely the x-intercept of the Nyquist-plot. This resistance was used to correct the measured potential to yield corrected potential (U_{corr}) with equation 5.1

$$U_{corr} = U - i R_{Ohm} \quad (5.1)$$

This measurement was followed by a CV, typically consisting of three scans with a scan rate of 10 mV s^{-1} in a potential range of 0.05 and 1.3 V vs. RHE. In some cases, the CV measurement was also carried out prior to activation procedure to determine the hydrogen underpotential signal of metallic Ir catalysts.^[147,148] This peak is only visible on fresh metallic Ir surface and disappears quickly once the catalyst is exposed to an oxidative potential above 1.4 V vs. RHE. The polarization curves were performed in potentiostatic mode via linear sweep voltammetry (LSV). Here the potential was increased from 1.2 to 2.0 V vs. RHE with a scan rate of 20 mV s^{-1} .

The determination of the stability of the catalyst was performed in a separate measurement with two different accelerated stress tests (ASTs) and subsequent determination of the Stability number (S-number) via the ratio of the amount of produced O_2 (n_{O_2}) during the stress test, which was calculated with equation 5.3, and the amount of dissolved Ir (n_{Ir}) in the electrolyte according to equation 5.2.^[13,66]

$$\text{S-number} = \frac{n_{\text{O}_2}}{n_{\text{Ir}}} \quad (5.2)$$

$$n_{O_2} = \frac{1}{zF} \int i(t)dt \quad (5.3)$$

Here, n_{O_2} is defined by the time (t) of the AST. The n_{Ir} was calculated by taking an aliquot from the electrolyte and determining the Ir concentration by ICP-MS.

Electrolysis testbench setup For measurements involving 4 cm² cells, a measurement cell manufactured by Fraunhofer ISE was used with Ti flow fields in a parallel channel setup (refer Figure 5.3.1). The CCM was placed in a dry state between a Pt-coated high-porosity Ti PTL (250 μm, ~70 % porosity, Fuel Cell Store) and a TGP-H-120 (370 μm, Fuel Cell Store) C GDL on the cathode and a Pt-coated low porosity Ti PTLs (250 μm, ~30 % porosity, Fuel Cell Store) on the anode. The PTL was added on the cathode to avoid an imprint of the flow-field on the C GDL and provide even compression for the GDL and CCM. This assembly was then compressed to 2 kN with four 127 μm thick Kapton[®] gaskets with two 127 μm Teflon[®] gaskets around the MEA to compress the C GDL by ~50 %. The optimal spacing for the gaskets was achieved with two 3D printed parts, that span around the flow field and provide compression on the gaskets in order to seal the setup. Measurements of CCMs in a testbench setup have been

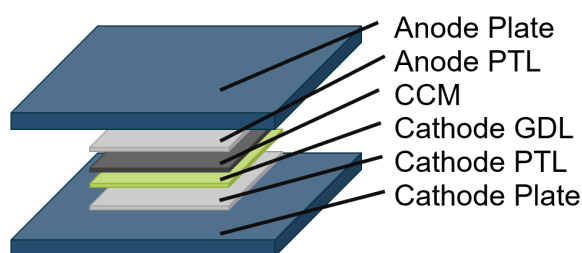


Figure 5.3.1: Schematic representation of the different MEA single cell setups.

carried out on an *E40-ETS* (Greenlight Innovation) test station using the 4 cm² cell for all measurements in 6.2 and 6.3. Pure water was supplied at 80 °C and 500 mL min⁻¹ to the anode side, while the cathode was operated with a dry N₂ or H₂ stream, depending on the measurement with 500 mL min⁻¹. The cells were left to equilibrate at this temperature without galvanostatic control for at least 30 min to ensure sufficient membrane hydration. Electrochemical measurements were recorded on an external solatron potentiostat with a 20 A booster (Ametek). Before CCM conditioning a CV measurement was carried out in order to determine the ECSA for Ir black catalysts before the CCM was exposed to any elevated potentials above 1.4 V vs. RHE. This was carried out under N₂-saturated water/H₂ conditions and five CVs were recorded from 0.05 to 1.2 V vs. RHE with a scan rate of 50 mV s⁻¹. A typical conditioning procedure consisted of a galvanostatic

hold at 0.1 A cm⁻² for 10 min and then 1 A cm⁻² for an additional 30 min under N₂-saturated water/H₂ conditions. For this, a N₂ stream with 500 mL min⁻¹ was added to the water stream in order to purge O₂ from the water. After initial conditioning, another CV was recorded with the same conditions to examine the influence of the conditioning. Then, five polarization curves were recorded by increasing the current density in different intervals up to a maximum current density of 5 A cm⁻² or a maximum uncompensated potential of 2 V was reached. In the first interval between 0 and 0.8 A cm⁻², the current density was increased in 0.005 A cm⁻² steps with a dwell time of 20 s. Afterward, the step size and dwell time were increased to ensure steady-state conditions to 0.05 A cm⁻² and 130 s, respectively up to 1 A cm⁻². Until 5 A cm⁻², the step size was increased to 0.25 A cm⁻² with the same dwell time and the back scan was carried out in the same intervals. After the initial dwell time, the cell potential was measured to be within 5 mV over 30 s intervals until stable conditions were achieved. As the polarization measurements were concluded, the CCM was assumed to be in stable conditions and end-of-test characterizations were carried out in N₂-saturated water/H₂ operating conditions. Here, galvanostatic EIS was recorded at current densities of 0.025, 0.05, 0.1, 0.15, 0.5, 1.0, and 2.0 A cm⁻² with an amplitude of 20 % of the applied current while not being under 0.01 A cm⁻² to ensure sufficient system perturbation. Each spectrum was recorded three times after an initial dwell time of 5 min was applied for each current density in a frequency range of 100 kHz to 1 Hz and averaged between individual measurements. These EIS measurements were used to determine the HFR as the x-axis intercept of Z' of the spectrum and utilized to correct the polarization measurements. The rate of HFR decrease with increased current density was calculated and included in the potential correction according to equation 5.4.

$$U_{corr} = U - \left(\frac{\Delta HFR}{\Delta i} i + HFR_0 \right) \quad (5.4)$$

Here, $\frac{\Delta HFR}{\Delta i}$ is the slope of the HFR decrease with current density and HFR₀ is the y-intercept of that regression. The spectra included for regression-based HFR correction were taken when the applied current density was above 0.5 A cm⁻². The determination of ionic conductivity was achieved with a measurement of potentiostatic EIS at 1.2 V after an initial dwell time of 10 min in a frequency range of 50 kHz to 300 mHz and perturbation amplitude of 10 mV. Each spectrum was recorded thrice and averaged. DRT analysis of the impedance data was carried out according to recommendations by Giesbrecht *et al.* with a $\lambda_{Tikhonov}$ of 10⁻⁴ and a m of 0.6 for PEMWE MEAs with Ir catalysts as was used here. The discretization

was done with a Gaussian function of first order derivative and inductive spectra portions also used in the analysis. The calculation was done with DRTtools in a modified Python script.^[149,150]

5.4 Physical Characterisation

Electron microscopy TEM characterizations were performed on a standard resolution device, an *EM900N* (Zeiss) with 80 kV acceleration voltage. High-resolution (HR)-TEM images were recorded with a *JEM-2100F* (Jeol) with a ZrO/W (100) Schottky field emission electron emitter at 80 to 200 kV acceleration voltage. The samples were prepared by suspending the powder catalysts in ethanol and depositing a drop (3.0 μL) on a polyvinyl butyral-coated copper mesh (*Polioform*, Plano GmbH). Microscopy on the standard TEM was performed by Jasmin Schmeling from DLR and microscopy on the HR-TEM was performed with assistance from Ute Friedrich from the electron- and light microscopy service unit of the Carl von Ossietzky University Oldenburg.

SEM images were recorded on a *S 3200N* (Hitachi) device with a W cathode and equipped with a back-scattering electron (BSE) detector. The SEM was operated with an acceleration voltage of 20 kV and currents between 1.3 pA and 22 nA to achieve optimal resolution at different scales and to avoid excessive damage on the samples.

The samples were prepared by placement between plastic sheets, which were wetted with acetone, in order to dissolve its surfaces and adhere to each other. This assembly was then cut in its cross-section with a razor and fixed on a Al sample holder with carbon tape. In order to facilitate electronic connection between the CL and sample holder, Ag suspension was applied between them.

X-ray photoelectron spectroscopy All measurements were carried out on an *ESCALAB 250Xi* (Thermo Fisher Scientific). A 1486.6 eV Al K_{α} monochromated X-ray source was used with a ray diameter of 650 μm . Powder samples were compacted in an Al sample holder and a charge compensation was employed during measurement. Survey spectra were recorded across the whole binding energy spectrum with a pass energy of 10.0 eV, 50 ms dwell time, and a step size of 1 eV. Element-specific high-resolution spectra were recorded subsequently with a pass energy of 50 eV, 50 ms dwell time, and a step size of 0.025 eV for all elements except Ir, which was recorded with a step size of 0.01 eV. Deconvolution of Ir XP-spectra was performed in *Unifit* (Unifit Scientific Software GmbH) with a Shirley

5.4 Physical Characterisation

background correction. Fit parameters can be found in Table 5.4.1 and the deconvolution was performed with parameters taken from Pfeifer *et al.*^[151] The values for satellite lines are given relative to the main line as a shift regarding E_B or a multiple of the value for the main line in the case of full-width half-maximum (FWHM). All 4f $5/2$ lines are shifted by 3 eV from the main line and Gaussian-Lorentzian sum (SGL) asymmetry specifies the Lorentzian character of the fit function with 100 indicating purely Lorentzian and 0 a purely Gaussian.^[151]

Table 5.4.1: Deconvolution parameter limits for XPS in adherence to parameters from Pfeifer *et al.*^[151]

Parameter	Ir ⁰	Ir ^{IV}	Ir ^{IV} sat.1	Ir ^{IV} sat.2	Ir ^{III}	Ir ^{III} sat.
E_B / eV	60.4–60.9	61.4–62.0	+ 1	+ 6	62.2–63.0	+ 1
FWHM / eV	0.8–1.2	0.8–1.6	x 2	x 2	0.8–1.6	x 2
Asymmetry	0.13, SGL(100)	0.20, SGL(55)	0	0	0.20, SGL(55)	0

X-Ray diffraction X-ray powder diffraction measurements were carried out on an *EMPYREAN* diffractometer (PANalytical) in a Bragg-Bretano geometry. The samples were irradiated by K_α X-rays emitted from a copper anode under 40 kV voltage and 40 mA current. The powder was deposited on an amorphous silicon disk sample holder with a minimal and uniform film thickness to avoid diffraction angle shifts. Standard measurements were recorded in a 10 to 90° 2θ range with a dwell time of 300 s per step and a step size of 0.013°. Analysis of diffractograms was performed with *HighScore Plus* Software (PANalytical) and the diffractograms background was corrected. Comparison to known crystal structures was performed with the crystallography open database and a version of the inorganic structure database of the FIZ Karlsruhe (PAN-ICSD version 3.5). *In-situ* high-temperature XRD measurements were performed with the addition of an *XRK900* stage under pure nitrogen or synthetic air atmosphere. The measurements were performed in 7 °C intervals starting at 350 °C up to 441°C and with a dwell time of 30 minutes after each temperature was reached.

Mass spectrometry All measurements to determine the elemental composition of materials were carried out on an ICP-MS (*XSERIES 2*, Thermo Fisher Scientific). An aqueous solution is inserted into the device, where it is ionized in an Ar plasma and subsequently separated by a quadrupole according to the element's

mass-charge ratio. Ir-containing samples were first dissolved in an aqua regia digestions by the addition of concentrated HNO_3 (1.56 mL, ROTIPURAN Supra, Roth) and concentrated HCl (3.45 mL, ROTIPURAN Supra, Roth) to 5 mg catalyst powder in a PTFE autoclave-liner. The mixture was then sealed in a steel autoclave and heated to 220 °C for 18 h. The sample solutions were diluted in a HNO_3 matrix (2 vol.%) and an internal Lu recovery standard was added to an aliquot and for the measurement. Device calibration was performed with multiple standard solutions of various concentrations for each element (Carl Roth) and a minimum correlation coefficient of 0.999 was used. The device was operated by Jana Ewert from DLR.

Thermogravimetric analysis For an analysis of the behavior of catalysts and catalyst layers under thermal treatment, TGA was performed on a *TGA4000* (Perkin Elmer) in a ceramic crucible. The measurements were performed under O_2 atmosphere to decompose the ionomer with a gas flow rate of 40 mL min^{-1} . The temperature was then increased from 30 to 950 °C with 5 °C min^{-1} and a hold time of 10 min at the top temperature. Analysis of catalyst materials was done directly with the powder, while the analysis of coated CLs required the scratching of the catalyst material either of the membrane or a PTFE sheet.

6 Results and Discussion

6.1 Comparative Analysis of Ir Catalyst Syntheses

Parts of this section have already been published open access in Adv. Mater. Interfaces 2023, 2300036. Reproduced in part with permission, copyright 2023 Wiley-VCH GmbH.

The most commonly used Ir catalysts in the PEMWE field are for the most part unsupported bulk catalysts or core-shell structures, where the resulting CCM thickness depends directly on the catalyst loading. This is the result of the packing of spherical catalyst particles that form the primary structure of the CL. In contrast, the primary structure of a CL with a supported catalyst mainly depends on the support material, assuming that the support material is significantly larger than individual catalyst particles. This contraposition is represented in Figure 6.1.1, where the CL thickness for bulk catalysts is correlated with the catalyst loading but it is independent of the catalyst loading for supported catalysts.

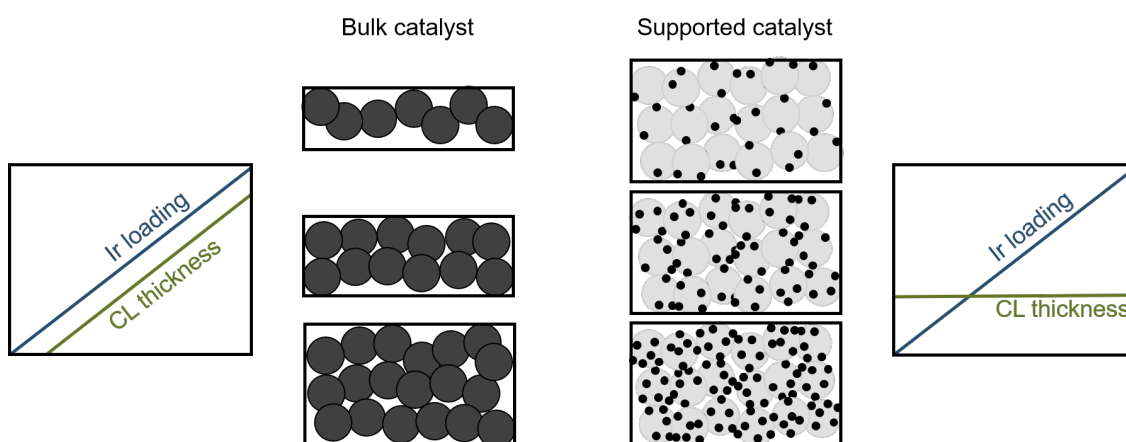


Figure 6.1.1: Schematic representation of the resulting CCM thickness per catalyst layer depending on unsupported or supported catalyst usage.

For this thesis, the use of a supported catalyst is imperative since the CL's thickness strongly influences the electrochemical performance and a variation of catalyst loading across the CLs z-axis would simply stack multiple of the same layers with varying thicknesses but result in an overall homogenous catalyst loading. Thus, the choice of a suitable supported Ir catalyst was essential for the success of an investigation into catalyst loading gradient CCMs. Commercially available supported Ir catalyst with different Ir loading but otherwise similar properties posed a challenge and since this field is still not fully explored for PEMWE catalysts the

6.1 Comparative Analysis of Ir Catalyst Syntheses

synthesis of in-house made catalysts was crucial. The most important properties of this catalyst would be a reproducible and precise deposition of Ir particles on the support material to minimize variation across different batches. Additionally, a low variation of electrochemical performance depending on the Ir loading is crucial since this would influence the performance of the overall resulting layer and obscure effects stemming from the gradient design. The catalysts were synthesized in three different Ir loading, namely 15, 40, and 65 wt.% ($m_{\text{Ir}}/m_{\text{total}}$), to allow for a wide variation of loadings to exacerbate effects ensuing from the gradient design, while ensuring a sufficient size difference between the support material and Ir particles to avoid an increased CL thickness with high Ir loadings.

As support material, ATO was chosen for all methods based on its relatively high electrical conductivity (2 S cm^{-1}) compared to other support materials.^[84,85,87,152] The main hindering factor for support materials is the stability in the highly corrosive PEMWE anode environment and thus mainly oxidic supports like TiO_2 or SnO_2 can be used. Four different methods were investigated for a comprehensive approach to identify suitable supported Ir catalysts. These resulted in different Ir species present on the support material and can be roughly separated in metallic Ir or IrO_x and rutile- IrO_2 species. The catalysts with metallic Ir particles were then further heat treated to convert them into IrO_2 catalysts. The methods used were (i) a reduction synthesis (RS) with NaBH_4 , (ii) a colloidal deposition (CD) with a reduction in ethylene glycol, (iii) a hydrothermal deposition (HTD) of a colloid in *tert.*-butanol and (iv) a modified Adam's fusion (MAF) synthesis with oxidation in NaNO_3 .

An overview of synthesis pathways with resulting Ir species is displayed in Figure 6.1.2. These methods are commonly used to deposit Ir particles on a support and are therefore also evaluated based on their ease of adoption in terms of necessary reaction optimization.^[84,98,140,144,146] The reaction parameters and reactant ratios were used as described by the original authors to estimate the method as anyone would adopt them to comply with the goal of this study.

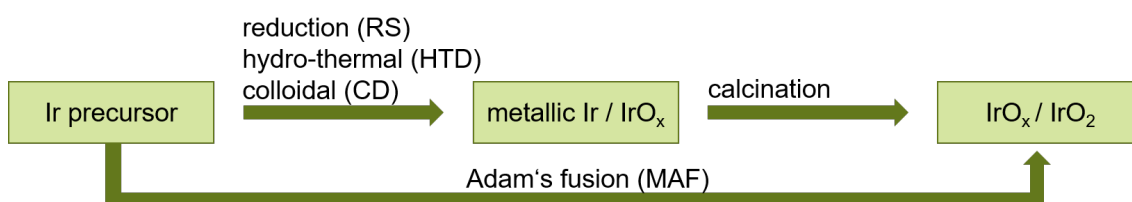


Figure 6.1.2: Schematic representation of synthesis pathways with the indicated method and proposed formed Ir species.

The resulting catalysts are then assessed based on their suitability for catalyst loading gradient CCMs and then used in further work in this thesis. The catalysts are characterized in-depth pertaining to structure-performance correlations and considered in the larger literature context. Furthermore, the synthesis methods themselves are evaluated in regard to their scalability to industrial processes and viability in a laboratory setting for further research in this area. Thus, this project provides an overview and categorization of different synthesis methods and Ir target species, a detailed analysis of their chemical properties, and a recommendation for both laboratory- and industrial-scale applications.

6.1.1 Ir Deposition Reproducibility and Precision

The deposition yield of the synthesis is an important parameter when comparing different methods, as an incomplete reaction can lead to loss of precursor material or involve complex recovery steps. This is especially important for noble-metal catalysts as these are particularly expensive and their relative scarcity makes efficient usage even more valuable. The yield of the reaction can be estimated by analysis with ICP-MS with the catalyst dissolved in a medium. Due to the stability of Ir, a dissolution with very harsh conditions is necessary, in this case the reaction in aqua regia under elevated pressure and temperature. All four reactions were carried out twice to estimate the reproducibility of the reaction with the exception of the MAF method, which was modified slightly between synthesis attempts to increase its deposition yield. The reproduction syntheses of the HTD and CD catalysts for 15 and 65 wt.% also resulted in little material, which was insufficient for ICP-MS analysis and these were thus omitted. Results of this analysis are displayed in Figure 6.1.3. The overall best deposition yield and reproducibility can be seen by the RS method with an Ir loading within ± 2 wt.% of the desired loading between both attempts for all loadings. Compared to the same method carried out in different studies, the yield here is higher than the one reported by Wang *et al.*^[140] They observed an Ir loading of 24 wt.% with an intended 30 wt.% on a Magnéli phase Ti_4O_7 support. This difference could be due to a preferable impregnation of the support material with the precursor in this study and therefore greater adherence of Ir particles on the support. Alternatively, the conversion of Ir^{III} to metallic Ir could be higher here, however, the added amount of NaBH_4 was already in excess which most likely leads to a complete reduction of the precursor in any case. Thus a stronger adhesion of the Ir on the support seems more likely to cause the increased deposition yield, which could either be due to the used support material or minute differences in synthesis execution.

6.1 Comparative Analysis of Ir Catalyst Syntheses

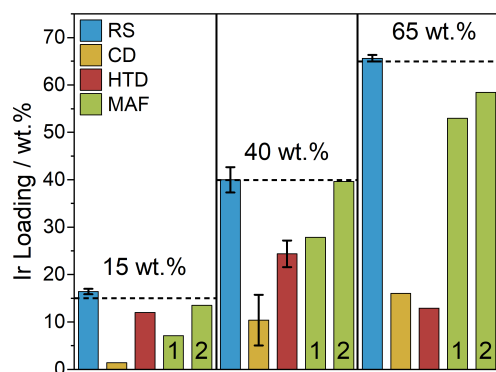


Figure 6.1.3: Ir loading for each synthesis for the three different desired loadings with indicated error bars pertaining to the median between both attempts and designated first and second attempts for the MAF method.

The first attempt at the MAF method resulted in catalysts with lower than desired Ir loadings with differences of 5 to 10 wt. % from low to high loadings. This lower-than-expected loading most likely results from low adherence of Ir particles on the support. In the second attempt, a longer impregnation time was implemented from 30 min to 3 days and an additional tip-sonication. As seen here, the Ir loading increased to comparable levels compared to RS after the reaction adaption, which supports insufficient impregnation as the reason for lower deposition yield in the first attempt. This method is thus also fairly precise for a targeted Ir loading. Both the CD and HTD methods were carried out using the same Ir colloidal suspension and are thus both dependent on the first reaction step forming the colloid. Especially, the CD method shows very low Ir loadings across all loadings. Compared to results from other studies this catalyst loading is particularly low as Hartig-Weiss *et al.* achieved about half the desired Ir loading on the support, while the loading here is about 25 % as high in the best case for the 40 wt.% catalyst.^[84] Abbou *et al.* even got an Ir loading fairly close to the desired one, indicating no intrinsically low deposition yield.^[144] This deposition method thus seems to be very dependent on specific reaction parameters and might need more optimization for each system. For example, the specific support surface area could play a big role as the area for the ATO here is about $28 \text{ m}^2 \text{ g}^{-1}$ compared to the ATO aerogels used by Abbou *et al.* with 40 and $80 \text{ m}^2 \text{ g}^{-1}$. A recovery of undeposited Ir would also require substantial effort, as the Ir is already in nanoparticle form and would most likely need a reconversion to the precursor. The HTD method, however, shows adequate deposition yields, at least for 15 and 40 wt.% Ir loadings, indicating an insufficient deposition of the colloid on the support in the case of CD

opposed to an incomplete colloid formation. Low deposition yields for both CD and HTD methods might indicate incomplete colloid conversion, which might occur at higher colloid concentrations. The high yield for HTD at 15 wt.% promises a fairly good capacitance for quantitative deposition of Ir particles as this was also observed by Böhm *et al.*^[146] The lower yields at higher loadings, however, indicate the need for reaction optimization most likely both the HTD and the colloid formation in the first step. Overall these two methods seem to be unreliable as not only the deposition across different loadings is very inconsistent but also between attempts. Especially, the CD method needs a fair amount of optimization for the specific catalyst system.

6.1.2 Physical and Morphological Characterization

Different Ir species formed during each synthesis significantly influence its electrochemical properties and thus their specific crystalline structure is of utmost importance. Figure 6.1.4 depicts the XRD patterns for all synthesized catalysts before their calcination. Most prominently, the ATO diffractions dominate the diffrac-

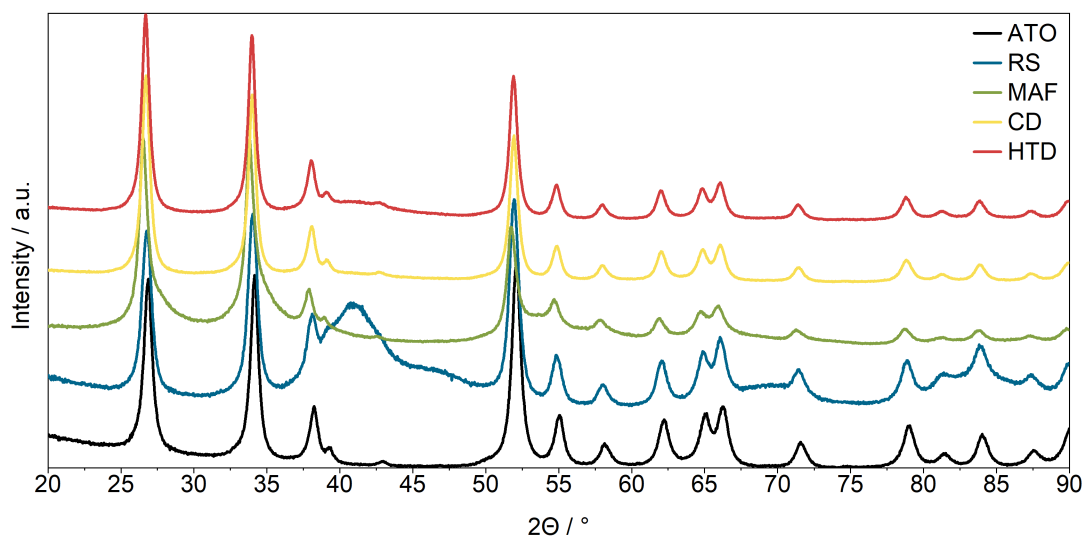


Figure 6.1.4: X-Ray diffractograms of all catalysts as-synthesized with unloaded ATO as reference.

togram for each catalyst with the two major diffractions at 26.6 and 33.9° 2θ , corresponding to the (110) and (011) facets. Further signals are apparent at 38.0 , 51.8 , 54.8 , 61.9 , and 66.0° 2θ with lower intensities and depict the (020), (121), (220), (130), and (031) facets, respectively. The most dominant Ir signal is apparent in the RS catalyst around 41.0° 2θ , which appears fairly broad, indicating a small crystallite size and, thus, most likely, small particle size. Scherrer analysis

of this peak suggests a particle size of 1.7 nm, however, due to the obfuscation of cubic Ir⁰ signals with ATO signals, this values presents a rough estimate as the Scherrer analysis becomes non-trivial. This diffraction corresponds to the (111) facet of cubic Ir⁰ and therefore hints at the presence of metallic Ir in this catalyst.^[140,146,153] Because of the broadness of this signal, another cubic Ir⁰ diffraction at 46.5° 2 Θ becomes protruded with further signals appearing at 67.7, 81.9, and 86.3° 2 Θ . The absence of signals suggesting oxidic forms hints at the presence of only metallic Ir or amorphous oxidic forms. Signals suggesting cubic Ir⁰ are also present in the HTD catalyst, albeit at a much lower intensity. This implies either a very small crystallite size, a low amount of formed Ir species, or an amorphous character of the latter. With the Ir loading of HTD at a desired 40 wt.% being around 30 wt.%, as seen in Figure 6.1.3, a low signal intensity due to low loading becomes improbable. Böhm *et al.* also observed a very broad peak for the HTD method at 41° 2 Θ , indicating the Ir species here might have formed in very small crystallites, becoming indistinguishable from the ATO signals.^[146] No apparent signals are visible for the CD catalyst, hence are at least indistinguishable from the ATO reference. This was also observed for other catalysts with the same synthesis route.^[144] The absence might implicate no crystalline Ir species has formed during the synthesis, where in-part a IrO_x mixed oxide was expected. This species would show a diffraction at around 33° 2 Θ , as was observed for a different colloid synthesis by Böhm *et al.*^[146] The lack of a crystalline species could be caused by incomplete condensation of intermediary Ir(OH)₆ during the reaction as discussed by Zhao *et al.*^[145] However, since only a very small signal can be seen for the HTD method it could be suggested, that low crystallinity or at least small crystallites are due to the colloidal synthesis as both of these methods use it.

The MAF catalysts show signals, that are hard to identify as distinct signals from the ATO, mainly at 28.0 and 34.8° 2 Θ . Further signals appear at 40.0, 54.0, 57.9, 65.5, and 66.1° 2 Θ , identifying the (020), (121), (220), (130), (112), facets, respectively The main signals at lower 2 Θ , corresponding to the (110) and (101) facets of tetragonal IrO₂, overlap almost completely with the (110) and (011) ATO facets and only appear as shoulders of those peaks. However, in comparison to mainly cubic Ir⁰ catalysts, like the RS method, the difference becomes more pronounced, especially when observed in relationship to different loadings, as depicted in Figure 6.1.5. Here the shoulder of those two signals becomes more pronounced as the loading degree goes up. However, the crystallite sizes also go down from 2.9 to 2.0 to 1.7 nm. Higher oxidation of the IrCl₃ precursor and subsequent crystallization could be the reason for this increase since the ratio of NaNO₃ oxidant

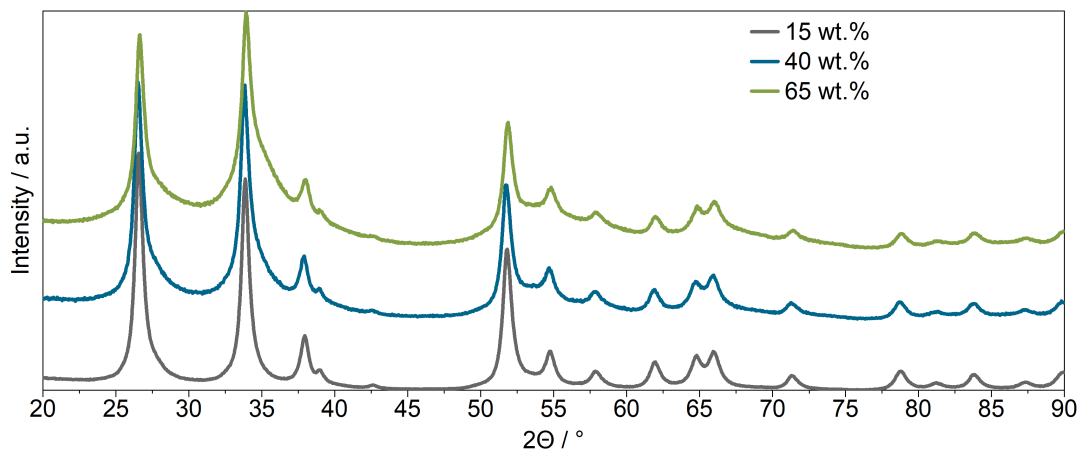


Figure 6.1.5: X-Ray Diffractograms of different loadings of MAF catalyst.

to precursor increases with loading. This phenomenon of decreasing crystallite size only occurs in the MAF method and none of the others, as seen in Table A.5. The variation between the crystallite sizes is however fairly small along with the overlapping with ATO signals and thus might be ambiguous as a direct correlation to oxidant ratio in the MAF catalyst. This small crystallite size is most likely due to the relatively low reaction temperature of 375 °C, as similar methods across the field range from 350 to 500 °C.^[142,143,154] As the reaction temperature increases, more pronounced particle ripening occurs and the IrO₂ becomes more crystalline to form needle-shaped rods. The crystallite size observed here increases only slightly from 1.7 nm as observed at 350 °C by Abbot *et al.*^[142] They also discussed the emergence of individual IrO₂ facets at lower temperatures, as no (110) and (211) facets, at 28.0 and 54.0° 2 θ , respectively, are visible at 350 °C but they start to form at 375 °C. Tetragonal IrO₂ rods form along the (110) plane, which might cause the small crystallite size for the catalyst observed here since the growth in this direction is only at its on-set at 375 °C.^[142,143] Going to higher reaction temperatures crystallite sizes increase more, but remain fairly small as the particle growth is most likely limited due to reduced O partial pressure in the NaNO₃ melt, as discussed by Böhm *et al.*^[98,154]

The calcination process of three of the catalysts in air was investigated by an *in-situ* XRD measurement, where the temperature of the synthetic air atmosphere was increased and measurement sequentially taken. These results are depicted in Figure 6.1.6. Each step consisted of a 7 °C ramp with a dwell time before measurement to allow for oxidation of the sample and stable conditions during the recording of the diffractogram. Overall, it becomes apparent, that the main diffraction at 41.0° 2 θ , indicating cubic Ir⁰ first narrows and then decreases in in-

6.1 Comparative Analysis of Ir Catalyst Syntheses

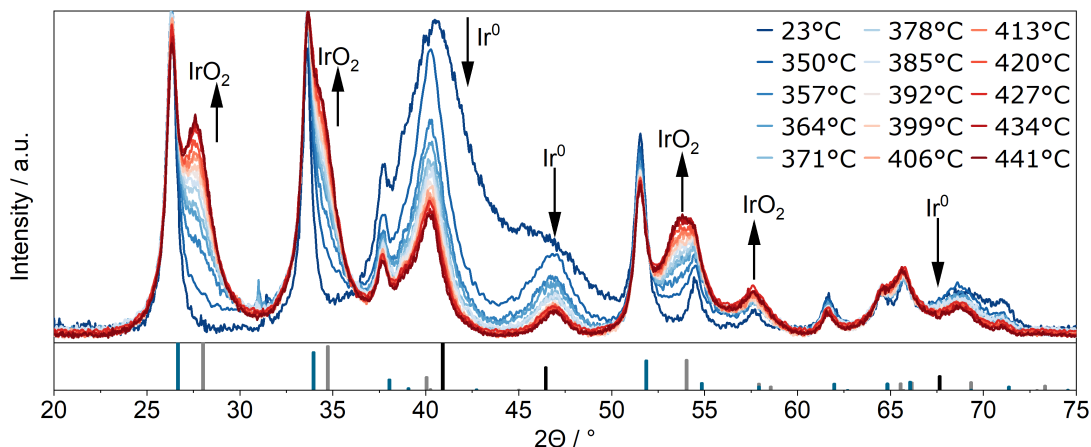


Figure 6.1.6: *In-situ* high-temperature diffractogram for 65 wt.% loaded RS catalyst with indicated peaks corresponding to cubic Ir and tetragonal IrO_2 and intensity trends with indicated diffractions for cubic Ir (black, ICDD: 00-046-1044), tetragonal IrO_2 (gray, ICDD: 00-015-0870) and ATO ($\text{Sb}_{0.1}\text{Sn}_{0.9}\text{O}_2$, blue, ICDD: 98-015-5956) Color grading indicates the calcination temperature for blue at room temperature to red at 441 °C with 7 °C steps from 350 to 441 °C.

tensity, while signals for tetragonal IrO_2 , as depicted, increase. The narrowing of the cubic Ir^0 (111) facet mainly occurs between room temperature and the first calcination temperature of 350 °C, implying a particle and crystallite growth of the metallic Ir particles. The second most intense diffraction for the cubic Ir^0 (200) facet at 46.5° 2θ also becomes more distinguished as they narrow. Here, the crystallite size doubles from 1.7 to 3.8 nm, with a further increase to 5.3 nm at 375 °C. This signal mainly decreases in intensity at higher temperatures while not significantly narrowing further. One explanation could be the surface oxidation of metallic Ir particles, which hinders further particle ripening and would only allow for crystal growth inside particles. The majority of intensity reduction occurs up to approximately 380 °C with it decreasing slower at higher temperatures. Most of the oxidation might have occurred here at lower temperatures with further metallic Ir only being oxidized at a lower rate. This might be caused by the surface oxide layer shielding lower metallic Ir atoms from the air atmosphere and only being exposed after the surface crystallizes further, thus uncovering more metallic Ir. It was also observed before, that complete oxidation of metallic Ir particles does not occur even after hour-long oxidation at 400 °C.^[155] This strengthens the assumption of a shielding oxide layer as this phenomenon also occurs in electrochemically treated metallic Ir particles, where only the surface gets oxidized.^[84]

Already at 350 °C oxidation occurs with an emergence of the (110) IrO_2 facet, as opposed to the observations discussed before by Abbot *et al.*, where this facet

growth was limited to higher temperatures in NaNO_3 medium.^[142] This confirms a growth limitation to be specific for this medium as it does not occur in air atmosphere at the same temperature. The growth of diffractions corresponding to tetragonal IrO_2 also increases at a higher apparent rate than the cubic Ir^0 ones decrease. A higher degree of crystallization at higher temperatures would narrow the diffraction and thus appear more distinct from the ATO signals. Higher degrees of crystallinity of tetragonal IrO_2 increase its electrochemical stability but also lower its activity.^[67,156] A balance between sufficient surface oxidation of the metallic Ir particles and preserving low crystallinity thus has to be struck when calcining these catalysts. With the chosen calcination temperature of 375°C , the majority of the decrease in metallic Ir intensity can be observed here while the tetragonal IrO_2 signals are still quite broad.

Differences between other thermally treated catalysts in their pristine and calcined form are shown in Figure 6.1.7. The same trends as observed in the *in-situ* XRD

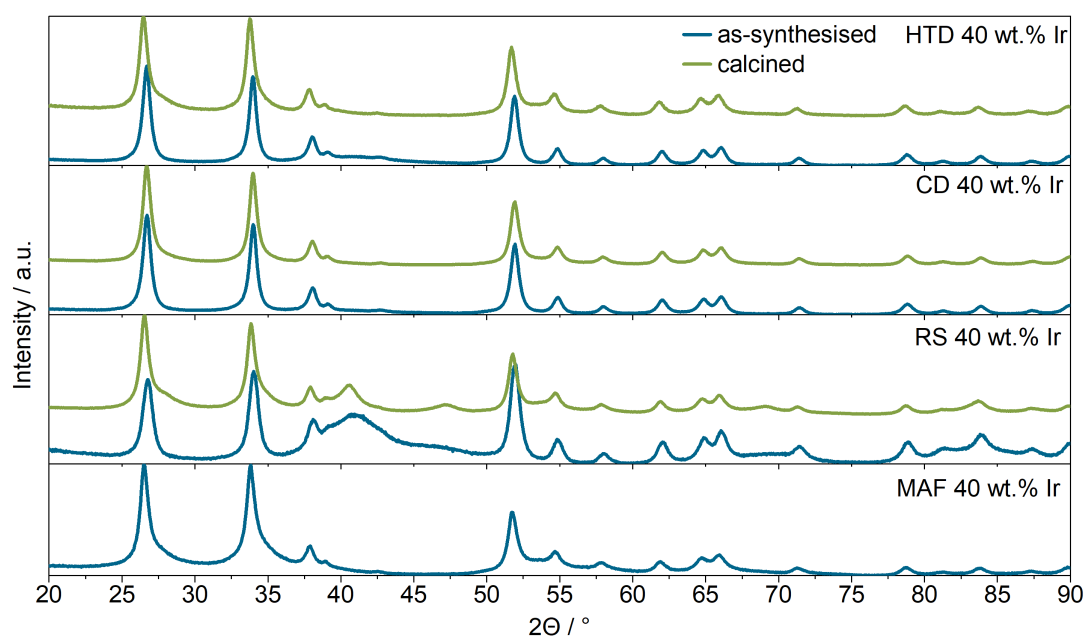


Figure 6.1.7: X-Ray Diffractograms of all catalysts both in as-synthesized and calcined form.

can also be seen here with cubic Ir^0 decreasing in intensity for both the RS and HTD samples. Shoulders on both major ATO signals become visible for these two catalysts in addition to the CD one. The emergence of tetragonal IrO_2 signals for CD suggest the presence of Ir species after synthesis but in either non-crystalline or nanocrystalline form. This could also be caused by further oxidation of intermediary $\text{Ir}(\text{OH})_4$ as discussed before. After calcination, the diffractograms of both CD

and HTD become quite similar to the MAF one with no apparent cubic Ir^0 signals visible.

The morphology of Ir particles deposited on ATO can be assessed by TEM. Micrographs of uncalcined and calcined RS catalysts are shown in Figure 6.1.8. At

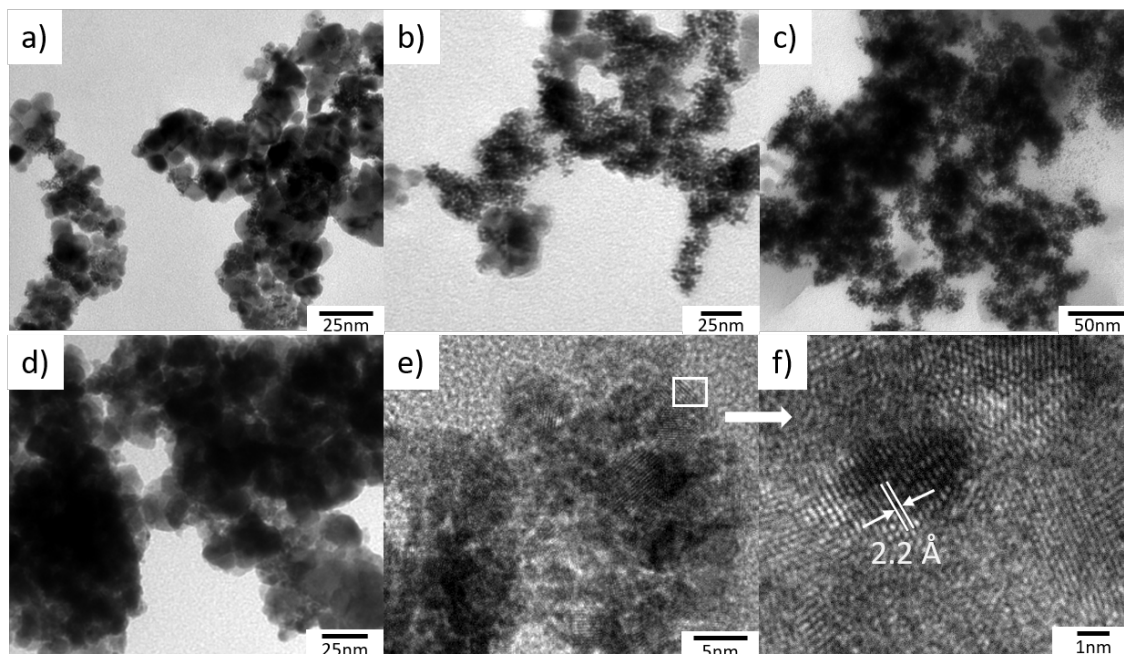


Figure 6.1.8: TEM micrographs of a) 15 wt.% Ir, b) 40 wt.% Ir, c) 65 wt.% uncalcined RS catalysts and d) 15 wt.% Ir calcined RS catalysts. Additionally, e) and f) depict the calcined 65 wt.% RS catalyst with enhanced resolution and indicated lattice spacing in f).

a low Ir loading of 15 wt.% particles are distinctly visible but appear in patches across the ATO particle. Individual particles are also clearly visible at a medium loading of 40 wt.% Ir, while some patches of particles touch and form a network of interconnected particles. This network is, however, not uniformly coating the ATO particle, as uncovered parts are still visible. A percolating network of Ir particles across the ATO support can be beneficial for PEMWE performance, as Ir is more electrically conductive, and electronic pathways can form along the particle network.^[98,146] This effect might even increase the catalyst's overall performance when considering that the ECSA of Ir particles is lowered when they touch and form patches. The particle patches seen in the lower loading catalyst with 15 wt.% Ir might not gain a substantial benefit in terms of electrical conductivity as these are too disconnected from each other. At a higher loading of 65 wt.% Ir, the support seems to be completely covered in Ir particles. This could result in an overall reduced ECSA without the performance-increasing effect of the percolating network. A support with a higher surface area might thus increase the capacity for

Ir loading without lowering dispersment of Ir particles. Upon calcination, the Ir particles oxidize and become more difficult to identify in TEM micrographs since the electron density declines and the contrast to the ATO support subsides.^[152] No apparent difference is visible on the particles once they are calcined. The identifiable Ir particles seem to retain their patch-like overall structure. This suggests, that the percolating network observed in the uncalcined samples is intact. However, the electrical conductivity is still lowered, due to the surface oxidation of the particles and thus increased interfacial resistance. High-resolution images of the calcined sample also show lattice spacings of Ir particles, as depicted in Figure 6.1.8.f. The reported spacing of 2.2 Å; however, is not specific to one Ir lattice as both metallic Ir (111) and tetragonal IrO₂ (110) facets show this spacing.^[88,97,146] One could argue, that the darker part of the particle hints at a metallic Ir core, due to the higher electron density, with an oxide shell but these micrographs do not provide rigorous evidence for this. TEM micrographs of the MAF samples at all Ir loadings are shown in Figure 6.1.9 Here, the electron density in catalyst and

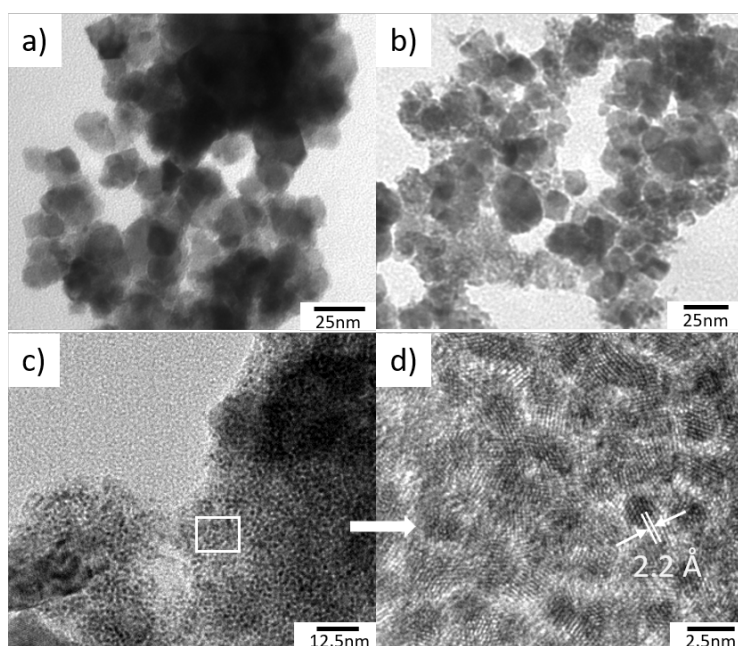


Figure 6.1.9: TEM micrographs of a) 15 wt.% Ir, b) 40 wt.% Ir, c) 65 wt.% MAF catalysts with d) showing enhanced resolution and indicated lattice spacing.

support material makes identifying individual particles difficult, as their contrast becomes comparable. Small particles on the bigger support can nonetheless be seen, especially at higher loading. These are thus most likely IrO₂ particles as the primary ATO particle size is fairly consistent over all catalysts. These particles seem to create loosely packed patches, similar to the RS catalyst, as some ATO particles are covered in smaller particles while some others are not. This be-

6.1 Comparative Analysis of Ir Catalyst Syntheses

comes even more apparent at 65 wt.% Ir loading with enhanced resolution, where individual IrO_2 particles become visible. These are roughly arranged around the ATO particle without forming tightly packed clusters, which might lower the available Ir surface area. They seem almost film-like in nature, which might be due to fairly small particles as indicated by the broad diffraction shape in the XRD. Again, the lattice spacing indicates the presence of either IrO_2 or Ir species as discussed before, while the particles more likely consist of IrO_2 . Less contrast to the ATO material and no indication of cubic Ir phases in the XRD underline the sole presence of IrO_2 particles. In contrast to the patch-like nature of the RS and MAF catalysts, the HTD catalysts show finely dispersed particles as seen in Figure 6.1.10.a and 6.1.10.b. A uniform distribution of particles as seen here is normally

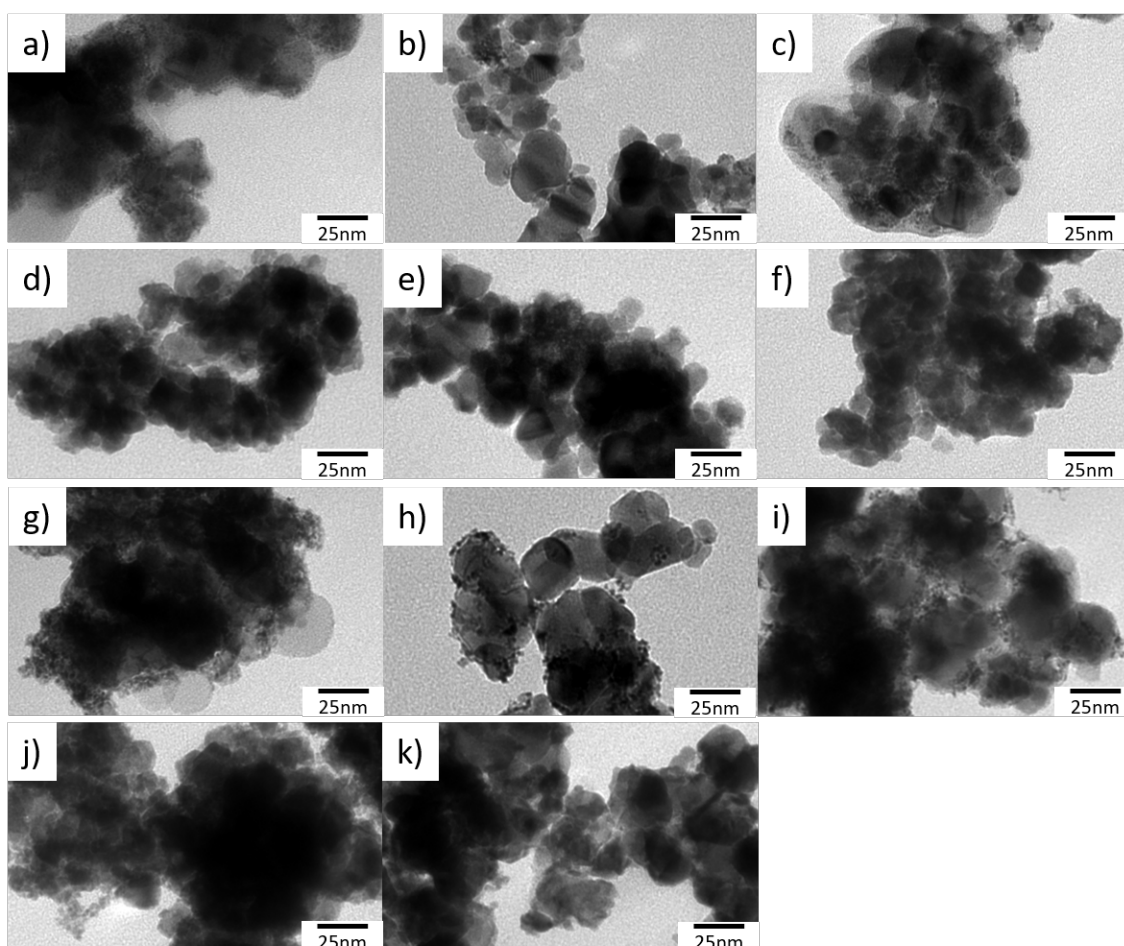


Figure 6.1.10: TEM micrographs of a) 15 wt.% Ir, b) 40 wt.%, c) Ir 65 wt.% Ir uncalcined CD catalyst, d) 15 wt.% Ir, e) 40 wt.% Ir, f) 65 wt.% Ir calcined CD catalyst, g) 15 wt.% Ir, h) 40 wt.% Ir, i) 65 wt.% Ir uncalcined HTD catalyst and j) 15 wt.% Ir, k) 40 wt.% Ir calcined HTD catalyst.

beneficial to available Ir surface area, as adjacent particles do not touch and thus lose available surface but the lack of a percolation network could be detrimen-

tal for MEA performance. With this arrangement of Ir particles on the support, its electronic conductivity becomes more important compared to the RS or MAF methods. However, as support material is still visible between the dispersed Ir particles, the capacity for additional Ir particles might be higher compared to the RS method as a higher loading there could lead to more clustering and thus available surface area loss. The micrographs for the CD method, shown in Figure 6.1.10.c and 6.1.10.d resemble the morphological structure of HTD with individual dispersed Ir particles. The loading here is lower than for the other catalysts, which is why the particles are sparsely distributed on the support. Both of these catalysts show the same phenomena as RS, once calcined. Individual particles become harder to identify due to the contrast loss but their relative position seems to stay the same.

The chemical composition of the Ir particles plays an important role in both the catalyst's performance and its durability under operation conditions. For further investigation, XPS was carried out and the results of different atomic ratios for Ir oxidation environments are depicted in Figure 6.1.11 and the corresponding XP spectra in Figure 6.1.12. The uncalcined RS catalyst is composed almost entirely

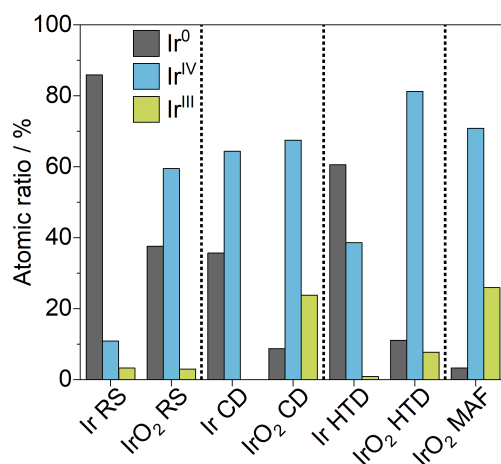


Figure 6.1.11: Comparison between the chemical composition of Ir4f species detected by XPS and indicated in the atomic ratio between different oxidation states for uncalcined and calcined catalysts.

of Ir⁰, as suggested by the XRD in the metallic fcc phase. Negligible amounts of both Ir^{III} and Ir^{IV} are present in the deconvoluted spectra but this could be due to small inaccuracies during the analysis and inherent errors and surface oxidation in ambient air.^[140] The almost exclusive presence of Ir⁰ also indicates only a small or no presence of unreacted precursor, which is present as Ir^{III} and thus a complete reaction. The amount of Ir^{IV} increases substantially, once the catalyst is calcined in air, which confirms the formation of an oxide phase in the catalyst.

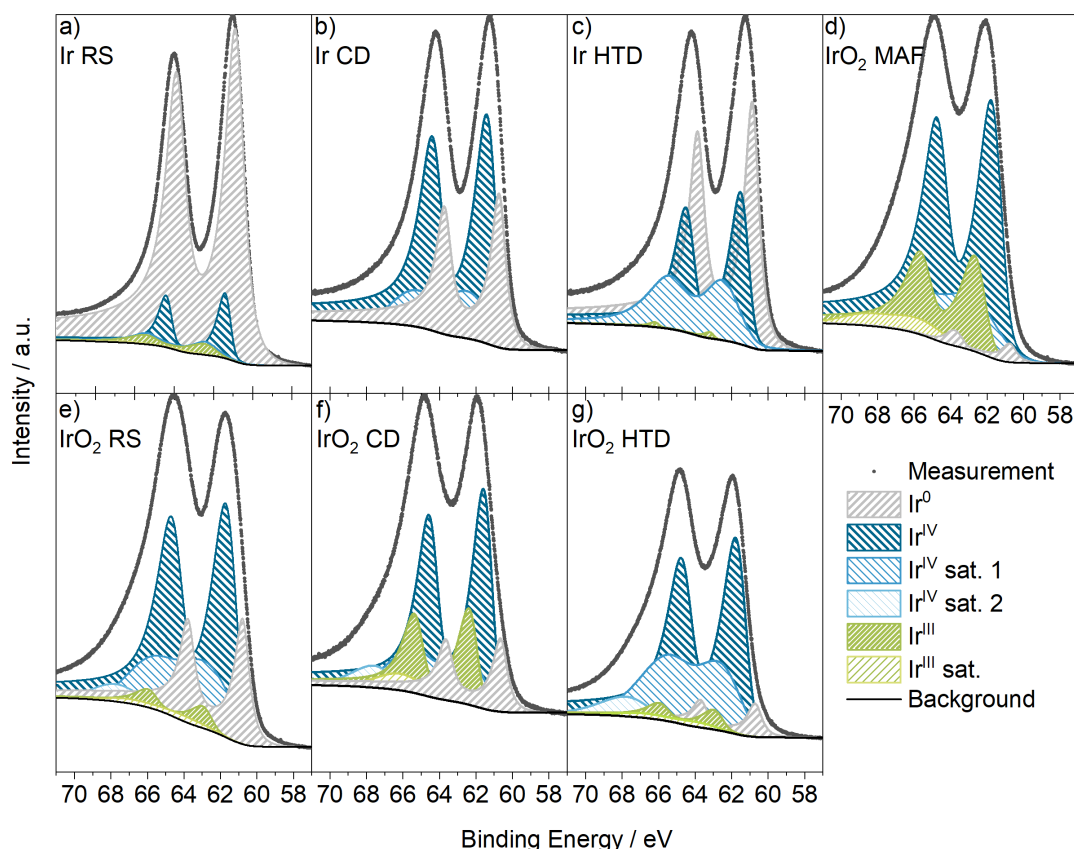


Figure 6.1.12: Ir 4f high-resolution XPS spectra of uncalcined (a-d) and calcined (e-g) catalysts.

However, not all detected Ir^0 disappears, which hints at an oxide surface layer with Ir^0 still present underneath. Even though XPS is a surface-sensitive technique the electrons' mean free path is around 7 nm in Ir and thus still larger than the whole particle, which means that not only surface oxide layers can be detected but also an Ir^0 core if present here.^[84,157] The amount of Ir^{III} stays fairly low even after calcination and might indicate a direct oxidation to crystalline IrO_2 that can also be seen in the diffractograms. The HTD synthesis also shows metallic Ir in its diffractograms and Ir^0 is also the main component in the XPS analysis. However, around 40 at.% of the whole Ir content in the sample is present as Ir^{IV} , which is substantially higher than for the RS method. The oxidized Ir most likely stems from the colloid formation, which was reported to produce IrO_x . Ir^{III} is however not present in the HTD catalyst, which might indicate a complete reduction of Ir^{III} during the hydrothermal treatment with the Ir^{IV} containing species being more resistant to reduction. A strong presence of Ir^0 can; however, also be seen for the uncalcined CD catalyst, which shows a substantial Ir^0 presence in addition to

the Ir^{IV} majority. When considering the uncalcined CD sample might have unreacted colloid intermediates present, which are also present in the HTD reaction mixture, the difference in Ir^{IV} in both catalysts indicated a rather small amount of Ir^{IV} was reduced to Ir⁰ in the HTD. The Ir^{IV} present in HTD catalysts might also be present as Ir(OH)₄, as no crystalline IrO₂ was detected in the diffractograms.^[84] Additionally, IrO_x phases instead of IrO₂ also necessitate the presence of Ir^{III} that can not be identified here.^[155] Böhm *et al.* report higher amounts of Ir⁰ for this method, which might be caused by different colloid synthesis methods.^[146] For the colloid synthesis, a higher amount of solvent was used here compared to the method reported in the literature and that might impact the reduction capability of the *tert.*-butanol due to lower overall concentration. The Ir⁰ found in uncalcined CD catalysts is not represented in the diffractograms, where no cubic Ir diffraction could be identified. This could indicate the Ir⁰ being present in very small crystallites but it is nonetheless present. IrO_x, which was postulated to be formed by Hartig-Weiss *et al.* can not be found here as no Ir^{III} is being detected.^[84] In their analysis even more Ir⁰ was found but it could also be caused by differences in deconvolution of the XP spectra.

When compared to other support materials, it was reported that ATO can induce lower oxidation states during the polyol method, which could be the reason this high amount of Ir⁰ was formed rather than IrO_x.^[88,158] When calcined, both HTD and CD catalysts show a strong decrease in Ir⁰ and an equal increase in Ir^{III}. The CD method shows almost equal amounts of Ir^{IV} in both calcined and uncalcined states, which hints at a direct oxidation of the Ir⁰ to Ir^{III}. The composition of this catalyst would indicate a IrO_x presence in addition to tetragonal IrO₂, as depicted in the diffractograms. Pfeifer *et al.* described, how the presence of Ir^{III} is explained in an amorphous IrO_x phase, where Ir^{III} is formed through oxidation of lattice O atoms due to Ir lattice defects.^[151] The cationic lattice thus further oxidizes adjacent Ir^{IV} atoms, forming Ir^{III}. The presence of two different O species proportional to the amount of Ir^{III} is; however, not possible in these samples as the O signals due to the ATO support superimpose any differentiation between O⁻ and O²⁻ lattice atoms. Ir^{III} only occurs in small amounts in the calcined HTD sample, compared to CD with a more comparable composition to the RS method. The amount of Ir⁰ is also very small here, indicating almost complete oxidation of all Ir species to IrO₂. A higher amount of Ir⁰ oxidation of the HTD method compared to RS might be due to a smaller particle size or more exposed Ir⁰ surface. This assumption is also supported by TEM images, where the HTD catalysts show more evenly dispersed Ir particles and thus allow for more oxidation. The difference between the calcined HTD and CD catalyst might hint at an incomplete colloid formation as the

relatively high amount of Ir^{III} in this sample could be formed through the thermal treatment of Ir(OH)₄ intermediates since Ir^{III} is not present in significant amounts in RS and HTD catalysts. A fairly comparable composition to the calcined CD catalyst is shown for the MAF catalyst. Here, a majority of the Ir is present as Ir^{IV} with a fairly high amount of Ir^{III}. IrO_x in addition to IrO₂ could have formed during the synthesis due to the low reaction temperature of 375 °C compared to other works using higher temperatures.^[74,142,143] The oxidative reagent in the form of NaNO₃ also lowers the O partial pressure during the reaction and thus decreases crystal growth but could also retain lower oxidation states for the Ir.^[98] It was also postulated, that surface Ir atoms might form hydroxo species as Ir^{III} since these are lattice terminated.^[142] Commercial IrO₂ catalysts also show a much lower content of Ir^{III}, which might be due to higher crystallization compared to the MAF catalyst synthesized here.^[158]

6.1.3 Electrochemistry

The suitability of a catalyst for a specific application not only relies on certain physical properties but also their electrochemical activity. Especially the relationship between features observed with different physical techniques and their emerging electrochemical properties is of great interest. The catalysts are here tested for their electrochemical performance towards the OER but also their stability against performance decay. To evaluate the catalysts based on their intrinsic catalytic activity, without the addition of more complexity, an aqueous model system in form of a half-cell RDE setup was chosen. When compared to an application setting, where the catalysts are applied in an MEA, different electrochemical features are pronounced differently in an RDE cell. Especially the mass-transport and electronic conductivity phenomena are expressed differently.^[134,159] The effects of the conductivity as discussed above for different catalysts are almost negligible in an RDE setup as the catalyst film thickness is very small as described by Lazaridis *et al.*^[134] With a sufficiently thin catalyst coating, the transport of product gases should also not lower the activity at high current densities as compared to an MEA setup where this effect can become much more pronounced. In general, the measured electrochemical activity of catalysts towards the OER is transferable to the activity observed in an MEA setup. However, stability determinations in RDE can lead to fairly different results when compared to MEAs.^[134,148,159] The formation of microscopic bubbles at catalytic sites can lead to an increased experienced potential at other sites during the stress test, which in turn leads to higher degradation rates. This might be one of the factors why the stability of catalysts in an

RDE setup is up to four magnitudes lower than in an MEA setting.^[134] This phenomenon also occurs independent of the chosen stressors, i.e. in galvanostatic as well as potentiostatic stress tests.^[148] Thus, the results from stability tests presented here do not necessarily reflect the catalyst's behavior in the electrolyzer application but they nonetheless serve as a guideline and a rough estimate of the stability compared to each other.

For an estimation of the activity of the synthesized catalyst towards the OER, all catalysts in addition to a reference catalyst for metallic Ir and one for tetragonal IrO₂ were characterized in a liquid electrolyte cell. The results of the mass-normalized polarization are presented in Figure 6.1.13 both over the whole potential range and the kinetic potential area. The highest mass currents of all tested

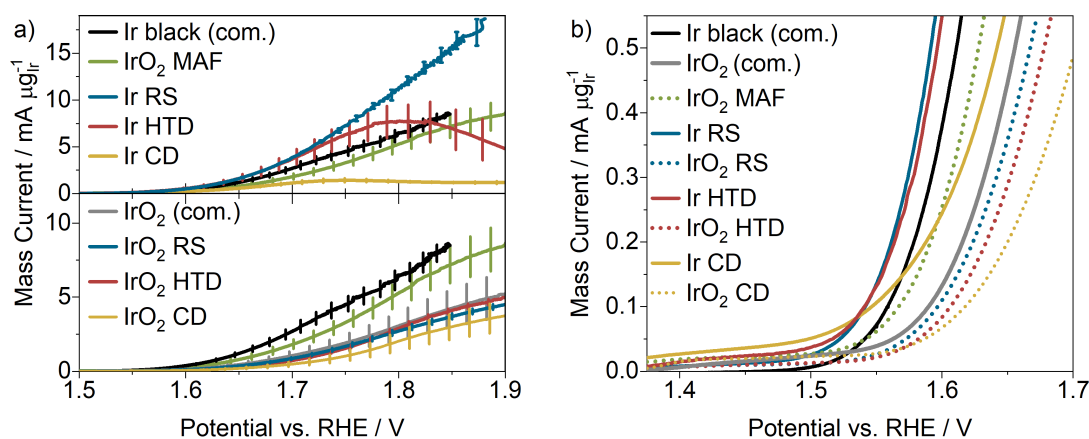


Figure 6.1.13: Mass normalized polarization curves a) of the (upper) uncalcined catalysts and (lower) calcined catalysts with 40 wt.% desired loading and Ir black and MAF catalyst as a reference and b) at a low overpotential of Ir (solid line) and IrO₂ (dotted line) catalysts with the desired 40 wt.% Ir loading.

catalysts are displayed by the uncalcined RS catalysts, which even exceed the reference Ir black with a similar composition of Ir species. The comparison between the RS and benchmark catalyst can be explained by the effect of supported nanoparticles, which show a higher accessible surface area due to their geometry, dispersion, and particle size.^[146,147] A possible different explanation is presented by Lettenmeier *et al.*, where the synthesis of metallic Ir nanoparticles leads to the formation of defects and low-coordinated sites, which enhance the performance and thus might explain the difference between the RS and reference catalyst.^[160] A similar onset potential, as seen in Figure 6.1.13.b, between both catalysts however indicates comparable kinetic properties. The initial oxidation of metallic Ir at OER operation potentials to a superficial porous IrO_x film also weakens this hypothesis as the defects present on the metallic Ir surface are quickly removed.

At lower potentials, the HTD catalyst shows a similar performance compared to RS, however, it experiences a steep decline in mass current at higher potentials. The initially similar performance is most likely due to similar Ir species, which is mostly metallic Ir as shown by XPS analysis. Even though the overall loading of this catalyst is much lower than the expected one, the similar mass normalized performance indicates a comparable overall catalyst. The higher amount of Ir^{IV} has no apparent effect on the performance at least at lower potentials. This may be caused by the electrochemical oxidation of metallic Ir upon the introduction to operating conditions to IrO_x, which is mainly composed of Ir^{IV} and Ir^{III}.^[147] However, the decline in performance at higher potentials marks a big difference to the other metallic Ir catalysts. A deviation from linear performance increase with higher currents is normally attributed to hindered mass transport of either the educts or products, in this case, most likely the product gases. A limitation of the diffusion of products typically leads to a plateau in the polarization curve but the decline observed here might indicate a blockage of active sites, probably by O bubbles. The difference in apparent mass transport properties in comparison to the RS catalyst is surprising since the same support material was used and the performance at low potentials is comparable. A possible explanation for this behavior is also not apparent in TEM micrographs as the morphology for both catalysts is similar. The effect however persisted over several measurements and thus can not be attributed to a flaw in the electrode preparation.

The CD catalyst shows significantly lower performance than the other ones, even when normalized for the mass of Ir species. They seem to follow the same shape of the polarization curve as the HTD catalyst with an increase at low potentials but stagnation and then a decrease at higher potentials but at much lower mass currents overall. This low performance could be an indicator of an incomplete reaction as hypothesized previously where the Ir present in the catalyst is at least in part not in an OER active form. Furthermore, the similarity in curve shape between the CD and HTD catalysts hints at some common mechanism at play even exacerbated through the synthesis where the same Ir colloid was used. Since both supports were treated very differently in the deposition of Ir particles, a common property pertaining to the support is unlikely to explain the probable site inhibition at high potentials. Some species present as Ir^{IV} could thus be responsible for this behavior, which could remain from the colloid synthesis, as seen in previous results determined by XPS.

The MAF catalyst is the only one synthesized here that is majority IrO₂ without a thermal post-treatment. In general, crystalline IrO₂ is less active than metallic

Ir or more accurately electrochemically oxidized IrO_x .^[67] The performance displayed here by the MAF catalyst is however comparable to the Ir black benchmark catalyst and is only slightly less active than the RS and HTD catalysts. Its onset potential is slightly higher than the metallic Ir catalysts. This high activity could be the result of its small particle size and good dispersion, probably producing a high ECSA. A relatively high presence of Ir^{III} might also promote the electrochemical activity as this could be the result of O defects in the tetragonal IrO_2 structure as described by Pfeifer *et al.*^[151,161] These defects in the lattice can be electrochemically active through the formation of electrophilic O^- that partake in the OER.^[66–68,151] Another explanation was suggested by Abbot *et al.*, where an Ir^{III} presence is an indicator for superficial Ir–OH species, which promote the OER.^[142,162] This catalyst also exceeds the performance of the thermally treated metallic Ir catalysts and the benchmark IrO_2 catalyst.

Once calcined the metallic Ir catalysts show a quite uniform performance, on par with the benchmark catalyst. Even the CD catalyst displays a not only comparable but improved performance compared to its uncalcined state. This increase might in fact be evidence of an initially incomplete colloid formation with the inactive intermediate being oxidized in the thermal treatment to form an OER active species thus improving the performance. The effect of a decreasing mass current at high potentials also disappears once the CD and HTD catalysts are calcined. The cause for this seems to be eliminated through the thermal treatment which might be leftover intermediates from the colloid formation as discussed before. The similar performance of the calcined catalysts indicates surface species that are uniform in nature. Even the catalysts with Ir^0 present seem to be fully oxidized on the surface with crystalline IrO_2 since their performance is similar to the fully oxidic benchmark catalyst. This is also implied by the shift in onset potential compared to the uncalcined state and in line with both references. Since Ir^0 is still present in the XP spectra of mainly the RS catalyst, it would seem the surface got oxidized and a metallic Ir core remains, which was also observed in TEM micrographs. This structure is further substantiated by the analysis of CVs presented in Figure 6.1.14. Here the H_{upd} area from 0.05 to 0.3 V vs. RHE is shrinking during the first introduction to elevated potentials even during the first few scans in Figure 6.1.14.a. This indicates the oxidation of metallic Ir species. Once the catalyst underwent the full activation procedure with prolonged exposure to oxidizing potentials, the H_{upd} area is no longer observable implying no more accessible metallic Ir presence. The activated RS catalyst's CV is comparable to that of the calcined one with the exception of a redox peak around 0.6 to 0.7 V vs. RHE. This signal is probably attributable to the $\text{Ir}^{\text{III}}/\text{Ir}^{\text{IV}}$ transition, regu-

6.1 Comparative Analysis of Ir Catalyst Syntheses

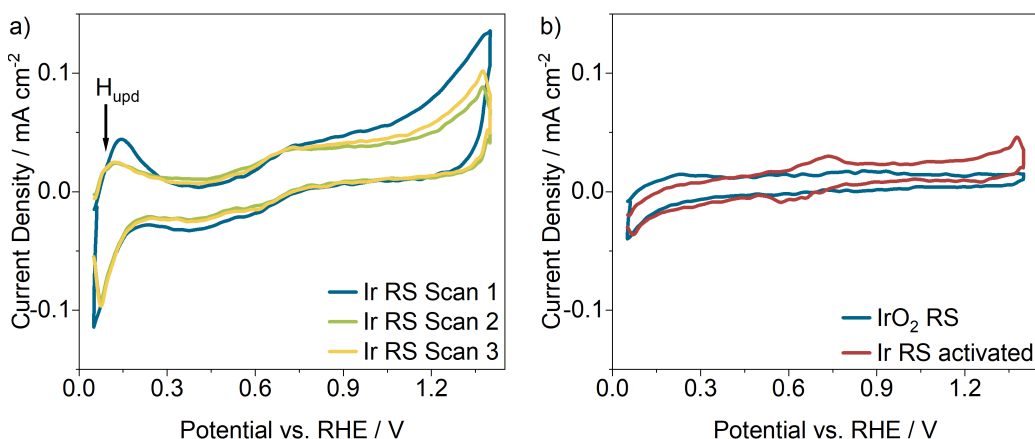


Figure 6.1.14: Cyclic voltammograms of 65 wt.% Ir RS catalyst, during initial electrolyte immersion (blue) and after electrochemical activation procedure (green).

larly observed in electrochemically produced IrO_x catalysts.^[163,164] The lack of this signal in the calcined catalyst further illustrates the sole presence of IrO₂ on the surface. The metallic core could remain even after the electrochemical oxidation through a metal-support interaction, preserving the Ir in a low oxidation state as discussed by Trogisch *et al.*^[84,88,148]

A determination of the ECSA could in principle shed more light on the difference between these chemically similar catalysts however for supported Ir catalysts this is non-trivial.^[59,147] Available techniques include the determination of the H_{upd} charge in a CV or CO-sorption experiments, as done regularly for Pt-based fuel cell catalysts but this phenomenon only occurs on metallic Ir sites.^[91,137,147] The introduction of different Ir species like IrO_x renders this approach thus ambiguous, even for mostly metallic Ir catalysts.^[137] Additionally, the ECSA of metallic Ir sites changes once oxidizes during the activation procedure as the oxidic Ir shows a different structure and is most likely porous including additional uncertainties.^[148] A comparison to IrO₂-based catalysts is also not possible since this species does not experience H_{upd}. Another approach based on the redox behavior of IrO₂ was proposed by Zhao *et al.* but this is only valid for IrO₂ based catalysts and does not translate well to other other techniques for metallic Ir catalysts.^[138] The application of active species-independent techniques like the comparison of specific capacitance and thus the surface area of the catalyst also only applies to non-supported catalysts as the contribution of the support material to the overall capacitance can not be estimated accurately.^[137,147,165,166]

Overall, the catalysts synthesized here show comparable performance to commonly used benchmark catalysts, i.e. Ir black and the Umicore IrO₂ / TiO₂ catalyst.

Even compared to other state-of-the-art research catalysts their activity is adequate. In comparison to a novel IrO₂-coated catalyst based on TiO₂ supports, the MAF catalyst displays a specific activity of 996 A cm⁻² compared to 1048 A cm⁻² from Böhm *et al.* with comparable Ir loadings.^[98] Its high specific activity, while consisting of mainly IrO₂ and probably being more stable, positions it as the apparently most suitable catalyst here. The electrochemical activity across different loadings was also investigated since this is a very important parameter for the choice of catalyst in this thesis. The results are displayed in Figure 6.1.15.

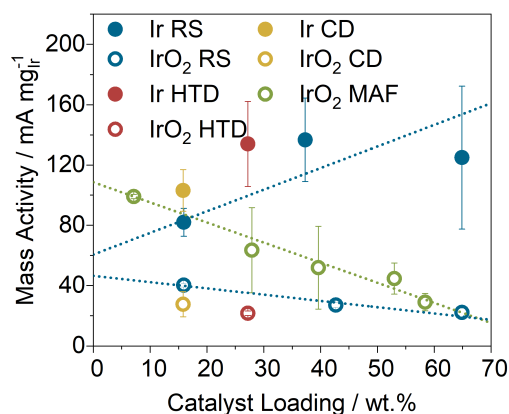


Figure 6.1.15: Mass activity regarding the catalysts' actual loading with (full) uncalcined catalysts and (hollow) calcined catalysts.

Most catalysts display a linear relationship of mass activity with its loading. A decreasing trend to higher loadings can be explained by particle dispersion on the support. As the number of particles increases relative to the supports surface area, the probability of adjacent touching particles increases and thus diminishes the relative accessible surface area of the Ir. This trend is however reversed for the uncalcined RS catalyst which might be caused by differences in electrical conductivity through the formation of a percolative Ir network. Even though the catalyst's conductivity is not too impactful in an RDE setup this might still explain this divergence. If this is the case, the difference is most likely even more pronounced in an MEA setting. In contrast, the calcined RS catalyst shows a decreasing mass activity with Ir loading but is still very stable. The oxidation could rearrange some of the clustering exhibited by the uncalcined catalyst and thus result in a uniform behavior in all loadings. For the characterization of the HTD and CD catalysts of different loadings, not enough material was available and thus they have been omitted here, especially since they are most likely not considered for further work here due to their irreproducible loading. The measurements that are available of

6.1 Comparative Analysis of Ir Catalyst Syntheses

these catalysts are in line with the respective other catalysts for each calcined and uncalcined state. The MAF catalysts show a declining mass activity with loading as well as the calcined RS one but display overall higher activity. Additionally, this catalyst displays a very predictable behavior even with more data points available.

The stability of three selected catalysts was estimated with a galvanostatic stress test and the electrolyte subsequently analyzed for dissolved Ir. Even though a determination of application-level stability is not possible through an RDE test, as discussed before, this test was carried out to provide a rough estimation of their longer duration behavior and especially their relative susceptibility to Ir dissolution. To this end, the S-number was determined for the uncalcined and calcined RS catalyst as these show the highest activity for metallic Ir catalysts in addition to the MAF catalyst, which shows superior performance compared to other IrO_2 catalysts. The S-number provides a reliable metric for the turn-over frequency (TOF) number for Ir catalysts as it is independent of the type of active species, catalyst loading, and ECSA.^[66] It was first introduced by Geiger *et al.*, is since then widely accepted in the community and basically describes the number of produced O atoms during the test in relation to each dissolved Ir atom.^[13,66,167,168] The results of this stress test are displayed in Figure 6.1.16. The general understanding is, that crystalline rutile-type IrO_2 is more stable under operation conditions than amorphous IrO_x . This is mainly due to activated or electrophilic O^- atoms inside the IrO_x lattice, which participate in the OER but can thus leave vacancies and lead to the dissolution of adjacent Ir atoms.^[66,169] Recently, comprehensive evidence was presented, that the activity differences can also be attributed to surface-bound intermediate O-species (O^*) that repel each other in adsorbate-adsorbate inter-

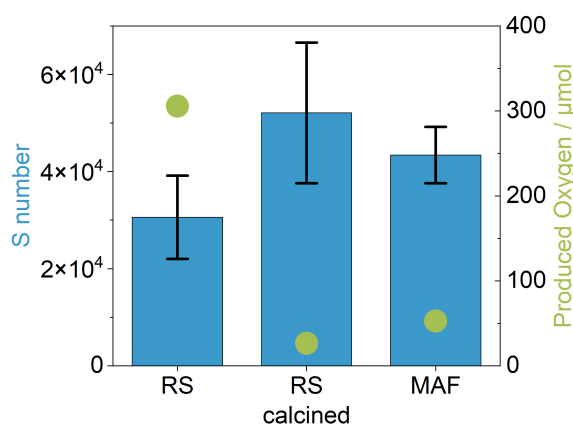


Figure 6.1.16: S-number (blue) and the amount of produced O atoms (green) during the AST for three selected catalysts.

actions, leading to a weaker Ir-O* binding and accelerated desorption of O₂.^[170] On IrO_x, the reaction participation of active sites penetrated deeper into the material, leading to a higher geometric activity due to more active sites present. This then leads to a higher O* coverage on the material, compared to rutile-IrO₂ and easier desorption of the product. The catalysts containing rutile-IrO₂ should then be more stable and show a higher S-number, since a lower amount of activated lattice O^{-l} atoms are present, which can in fact be observed here, where the calcined RS and MAF catalyst exceeds the uncalcined RS one. The dissolution rate of the uncalcined RS catalyst is about 10-20 fold higher than the IrO₂ containing ones but it shows a very high OER activity and thus its S-number is only slightly lower than the more stable catalysts as the S-number is defined as the ratio of produced O to dissolved Ir.

The calcination process leads to a vast increase in dissolution stability as seen here, most likely due to the complete surface oxidation to rutile-IrO₂ as also seen in XPS and XRD analysis. The absence of Ir^{III} and thus activated lattice O atoms leads to a less generated O compared to the MAF catalyst, which contains some Ir^{III}.^[66,151] Higher amounts of Ir^{III} could lead to a higher amount of lattice participation in the MAF catalyst, increasing the O* coverage without excessively destabilizing the lattice.^[170] The values for S-numbers presented here are also in line with the ones presented in recent studies with comparable materials. They match the ones reported by Daiane Ferreira da Silva *et al.* for a mix of IrO_x and IrO₂ catalysts.^[13] The S-number of the uncalcined RS catalyst even exceeds all reported values for supported metallic Ir and even IrO₂ based catalysts (up to 2.0 x 10⁴), which is most likely due to its high activity, hence a large amount of generated O₂.

These results indicate a trade-off between the stability and activity of the catalytic species and the desired catalyst may need fine-tuning depending on the desired properties. For example, a lower reaction or calcination temperature could be used in order to generate less crystalline rutile-IrO₂, which shows a higher activity at the expense of stability or in turn a higher temperature for the reversed result. It seems that a rutile-IrO₂ lattice with Ir defects, inducing higher activity through electrophilic O atoms, could be advantageous as it shows a significantly higher stability compared to amorphous electro-oxidized IrO_x. Especially in a water electrolysis application the longevity of the catalyst is paramount since these devices need to operate for a long time in order to assimilate the high CAPEX of the system.^[9,11,171]

6.1.4 Evaluation of the Synthesis Methods

As stated initially in this chapter the choice of catalyst for further work in this study depends on several factors as the reproducibility of Ir loading, a linear and possibly low variation of electrochemical activity in relation to Ir loading, and the ease of adaption to larger batches. When considering the use of a catalyst for industrial use the Ir loading yield grows in importance along with the efficiency of scale-up and inherent costs of scale-up due to synthesis conditions. This includes the choice of solvents, additives and general reaction procedure. In terms of reaction yield or the efficiency of conversion of initially used Ir to the final catalyst is fairly high for the RS and MAF catalysts used here. The RS shows a complete conversion of the precursor to deposited Ir, just as the MAF after an initial optimization. In contrast, the HTD and CD not only deplete the used Ir precursor with the incomplete conversion but also do not show a linear behavior of the reaction yield with desired Ir loading on the support. The recirculation of unspent Ir precursor or reaction intermediates would require additional effort and would thus drive costs. The adaptability of the synthesis to larger batches is especially easy for the MAF as it employs a salt melt reaction, which is already applied in industrial settings.^[67] This reaction also seems to be applicable to different support materials with little modification and can the catalysts properties can be influenced through simple variations of reaction temperature and time.^[67,74,98]

A different reaction path is taken with the RS, where a wet-chemical approach employs ethanol and CTAB in addition to the Ir precursor. These materials are readily used in industrial processes with an easy evaporation and recirculation option for the ethanol solvent.^[172,173] However, this reaction also uses NaBH_4 as a reduction medium, which often requires water-free solvents in order to yield high precursor conversion. This adds extra complexity if carried out in water-free conditions but this step can also be substituted by the addition of a base. NaBH_4 was shown to be rather stable under alkaline conditions with its half-life increasing exponentially with the pH value of the solution.^[174] It could be shown here that the Ir loading of catalysts synthesized in water-free conditions is as high as the same reaction carried out in atmosphere-exposed ethanol just with the addition of some NaOH to the NaBH_4 -containing solution. This could make steps to remove water from the solvent obsolete and reduce the complexity of the reaction. The two remaining syntheses first employ the formation of an Ir colloid, which utilizes ethylene glycol as the solvent. Its high boiling point makes the removal of the solvent non-trivial and adds additional required reactor volume as the formation is dependent on the ratio of solvent to precursor. Simple evaporation under reduced pressure

complicates the separation of the final product as either fairly low pressures or a high temperature are required. An easier scale-up could be achieved with a different colloid-forming method instead of the one reported here. HTD additionally employs a pressure vessel, which can pose dangers, especially at larger scales.

These considerations eliminate both the HTD and CD method for the chosen catalyst in this thesis as their irreproducible reaction conversion is not reliable enough for the small differences in catalyst layers investigated here. The RS catalyst shows a substantially higher electrochemical activity than the other catalysts investigated and even higher than the benchmark ones. Additionally, it converts the entire precursor to active species, making the Ir loading very reliable and targetable. However, the mass activity in relation to its Ir loading is non linear, most likely due to an effect of a percolating Ir network. This behavior is rather favorable in an MEA setting for PEMWE application but it renders the analysis of loading gradient CLs rather difficult. Its calcined form avoids these downsides but also lowers its electrochemical activity. Finally, it was decided the MAF catalyst would be used moving forward as it employs a very easy and scalable reaction in addition to the high specificity of the Ir loading and high activity.

6.2 Ionomer Gradient CCMs

6.2.1 Influence of Ionomer Content on CCMs

The ionomer in a CL serves both as a binder and as an electrolyte, conducting charge carriers from the membrane to the active sites of the catalyst and the TPB. In most cases, the ionomer forms a thin film around the catalyst particles, providing charge carrier conduction while also being penetrable for educt and product transport. As the ionomer content is varied, the film varies in its coverage of the catalyst particles, its thickness and subsequently also the ion conductivity. Through its varying thickness, the available void volume between catalyst particles as the layers rigid structure is influenced as well. The interplay between these different properties directly influences all different types of overpotentials and thus the overall performance of the PEMWE cells. In general, the performance of a CCM can be described in terms of the total potential as the sum of overpotentials in addition to the reversible cell voltage according to equation 6.1.^[12]

$$E = E^0 + \eta_{act} + \eta_{Ohm} + \eta_{Ion}^{Cat} + \eta_{Ion}^{Ano} + \eta_{MT}^{Cat} + \eta_{MT}^{Ano} \quad (6.1)$$

Here, E is defined as the sum of E^0 , η_{act} , the ohmic overpotential (η_{Ohm}), the ionic overpotential (η_{Ion}) for each electrode individually, and mass transport overpotential (η_{MT}) for each electrode. The contribution of the Ir loading to the overall performance lies mainly in η_{act} , as the amount of active sites vary with different loadings, influencing kinetic parameters of the CL. Additionally, a large contributor is η_{Ohm} , as the Ir loading on the support material contributes large portions to its overall electrical conductivity and thus directly influences the HFR. Individual contributions of the overpotential terms are crucial to understand the CL's properties and individual changes based on different materials and compositions.

The assessment of the influence of ionomer content on these individual contributions was accomplished with homogeneous ionomer composition CCMs between 5 and 30 wt.% ionomer loading to provide a substantial difference between each contributing factor in each CCM. For a wide variety of Ir catalysts, the optimal ionomer loading was reported to be between 8 and 15 wt.% Nafion[®] with various different factors influencing it.^[12,96,135,175] Even though an optimal overall performance can be observed at lower ionomer loadings, higher loadings may be beneficial in certain areas, such as ionic conductivity and thus might be valuable in gradient designs.

In order to evaluate overpotential contributions of the ionomer loading at different Ir loadings and thus overall CL mass, homogeneous 10 and 30 wt.% CCMs were characterized at 1 and 2 $\text{mg}_{\text{Ir}} \text{cm}^{-2}$. As the ionomer contents that were chosen for the gradient designed CLs, these are of special importance. Ionomer contents of 5 and 20 wt.% are discussed further down at just one overall Ir loading of 1 $\text{mg}_{\text{Ir}} \text{cm}^{-2}$. The results of the overall cell performance are displayed in Figure 6.2.1. The impact on performance is not linearly dependent on the Ir loading as becomes

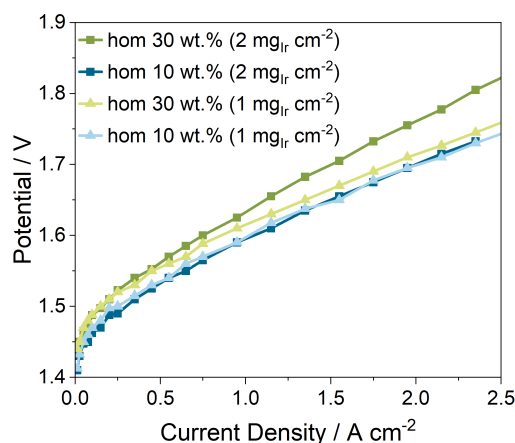


Figure 6.2.1: Polarization data for homogeneous CCMs with 10 wt.% and 30 wt.% ionomer loading at a catalyst loading of 1 $\text{mg}_{\text{Ir}} \text{cm}^{-2}$ and 2 $\text{mg}_{\text{Ir}} \text{cm}^{-2}$.

evident through the not too different performance of the CCMs. The performance difference between the CCMs with 10 wt.% is negligible across the whole current range, which indicates no impact of the loading for uncompensated polarization. It differs for the 30 wt.% CCMs, where the lower loading one performs better than the higher loading one. The difference becomes clear at higher current densities, which hints at higher η_{MT} at the higher loading. This can be explained by the different thicknesses of the CCMs, where product gas has to be transported and longer diffusion paths increase the cell voltage through a hindrance of subsequent products.^[12] If the products cannot be transported quickly enough, the partial pressure of the product at the catalytic site increases and thus reduces the electrochemical reaction rate. This is then expressed as an additional overpotential contribution as the reaction rate requires a higher potential to reach the same value compared to that without the product transport hindrance. Even at an high ionomer loading, the performance of the 30 wt.% CCMs comes quite close to 10 wt.% ones, indicating only small contributions of the ionomer loading to the overpotential seen here. An optimal ionomer loading was determined for different Ir and IrO₂ catalysts to be close to the 10 wt.% used here, where different studies found large performance differences between variable ionomer loadings.^[12,96] The smaller difference here

might be due to the catalyst used, namely Ir black nanoparticles, where other groups have used IrO_2 -based catalyst with different structural properties.

The ionomer's performance impact and mass transport contributions are a function of the ionomer pore filling and differs for different catalyst densities. As Bernt *et al.* describe completely filled pores at 25 wt.% ionomer loading for an $\text{IrO}_2/\text{TiO}_2$ catalyst, the one used here shows filled pores at 28 wt.% as displayed in Figure 6.2.2 with values calculated from equations A.1 and A.2. The pore volume of the

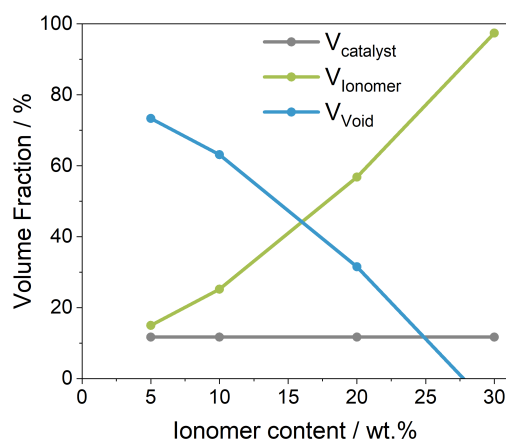


Figure 6.2.2: Calculated volume fractions for an Ir black catalyst based on the calculations and reference values presented by Bernt *et al.*^[12]

catalyst layer is not only a function of the catalysts density but also its packing density as the catalyst here occupies roughly 15 % of the void volume, whereas the mentioned $\text{IrO}_2/\text{TiO}_2$ catalyst takes up around 30 %.^[12] This difference leads to a higher void volume at low ionomer loadings but declines more rapidly, still resulting in a slightly higher ionomer content when approaching zero void volume. Even though this is just a rough estimation of the void volume fractions, it hints at severe gas transport hindrance through the pores at high ionomer contents. The high performance of the 30 wt.% CCMs with lower loading suggests an additional effect to the mass transport as no clear difference to both of the 10 wt.% CCMs can be observed at high currents. The transport by diffusion through pores and ionomer can be accompanied by transport through cracks and pinholes in the CCM as Bernt *et al.* proposed even for CCMs with very low void volume as seen here.^[12] Mandal *et al.* also observed severe volcano shaped cracks on the CLs surface after testing without sufficient pore volume inside the CL, which are also likely here but no *post-mortem* analysis was carried out.^[91] This could also explain the difference between the different 30 wt.% loadings, as the transport through cracks is still impeded by a thicker CL and thus longer convection paths.

Since a large fraction of the CL is ionomer, this could also rapidly fill CL cracks or hinder their formation as the ionomer also acts as a binder between catalyst particles.

The performance difference between Ir loadings seems to only occur at higher ionomer loadings, mainly determined by mass transport contributions. In order to further analyze the impact of the ionomer loadings to better understand the contribution of a gradient structure, CCMs with varying ionomer loadings at the same Ir loading have been characterized. The Ir loading was held constant between CCMs with the assumption, that the catalyst particles are determining the overall CL structure and ionomer mainly filling the pore space between particles. Thus, the CL thickness and any other properties stemming from structural parameters should be the same indifferent of the ionomer content. Performance data in terms of uncompensated polarization curves for ionomer contents of 5, 10, 20, and 30 wt.% are displayed in Figure 6.2.3.a. The overall performance differ-

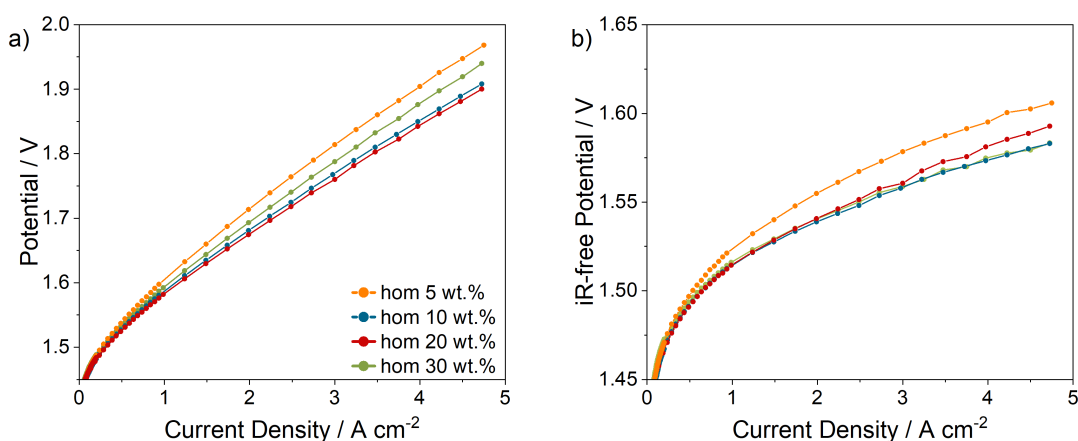


Figure 6.2.3: Polarization curves for homogeneous and gradient CCMs with a) uncompensated and b) HFR compensated potential.

ence between the varying ionomer loadings is quite low but generally rather high and comparable to results from other studies.^[12,91,93] In contrast to other works showing an optimal ionomer loading of 10 wt.%, an optimum can be observed here at 20 wt.% with the overall lowest potential across the whole current density range.^[12,96,135,175] A difference in optimal ionomer loading could be caused by different CL structure and pore-size distribution due to the coating process. At low current densities, all CCMs show a comparable performance indicating similar kinetic properties of the layers. This is expected as the same catalyst is used across all ionomer loadings and it should have little impact on kinetic aspects of the layer. In the high current densities range, the polarizations deviate more, which

can be attributed to a combination of ohmic resistance, stemming from contact resistances, ionic transport within the layer and mass transport contributions.^[12,176] Varying the ionomer contents further from the optimum of 20 wt.%, namely to 5 and 30 wt.%, yields a lower performance in both directions. However, the CCM with only 5 wt.% shows the lowest performance with a quite high margin to the optimum. Even though void pore volume should be quite high at this ionomer loading, it might be insufficient to provide acceptable ionic conductivity and the ionomer coverage of catalyst particles could be much lower than the other CCMs. The individual contributions to the overall overpotential are discussed in detail further on.

Compensated of iR -free potential polarization represents the overall cell potential with the ohmic resistance deducted and shows more detail about the performance of a CCM. This data is displayed in Figure 6.2.3.b and shows almost no difference between the 10 and 30 wt.% CCMs, which was observed in the uncompensated polarization data. The difference stems from varying HFRs between the two with the 30 wt.% one showing a higher ohmic resistance than the 10 wt.% one ($77.3 \text{ m}\Omega \text{ cm}^2$ vs. $72.5 \text{ m}\Omega \text{ cm}^2$ at 0 A cm^{-2}). The higher η_{Ohm} increases the cell potential and when deducted, indicates a similar performance between the two CCMs. The CCM with 20 wt.% ionomer content shows a lower performance and higher compensated potential in contrast to the uncompensated potential compared to the 10 and 30 wt.% CCMs, which is due to an even lower HFR of $68.2 \text{ m}\Omega \text{ cm}^2$, increasing the remaining potential above the other two. Differences in the HFR can be attributed to electrical contact resistances between catalyst particles, the CL and PTL, and PTL and current collector.^[12,176,177] As the same cell setup is used for all CCMs, different contact resistances between the PTL and current collector can be neglected, leaving only inter-particle and CL-PTL resistances. The ionomer in the CL was reported to be able to isolate catalyst particles at high contents, as the void pore volume is exceeded and the ionomer film gets thick enough around particles to completely envelop them, thus rendering individual particles or particle agglomerates inert for the electrochemical reaction.^[96,99] Jang *et al.* observed this effect to its maximum degree with the HFR increasing to $500 \text{ m}\Omega \text{ cm}^2$ at an ionomer loading of 40 wt.%, which can not be perceived here with an only slight increase in HFR.^[96] This might very well be the case for the high HFR in the case of the 30 wt.% CCM where the highest ionomer content leads to the highest HFR. When considering this, the lowest HFR at 20 wt.% is unusual as 10 wt.% ionomer would induce even less isolation issues; however, a second phenomenon could come into effect, where a low ionomer content might not cover all available catalyst particles, leaving some without an

ionic conduction pathway. As the reaction in an electrolysis cell is reliant on the availability of TPBs, an impaired ionic connection can also isolate particles from the reaction and increase the HFR. This is especially visible when considering the compensated polarization of the 5 wt.% CCM, which shows the lowest performance even after correction for its quite high HFR ($81.2 \text{ m}\Omega \text{ cm}^2$). Insufficient ionomer coverage is the most likely cause for this high HFR but the compensated potential is still higher than for the other CCMs, stemming from additional overpotentials such as a hindered ionic conductivity due to the low amount of ionomer, which can influence the ionomer films thickness and thus ionic transport properties. The ionomer content of 20 wt.% might thus be the optimal value for the HFR in this regard, striking a balance between both HFR-increasing effects. Another contribution to the increased contact resistance might be the contact between the CL and PTL. Even though the same cell setup was used for all measurements, different surface compositions of the CCM could induce additional resistance as the ionomer might be pushed out of the layer and agglomerate on the surface. This would especially affect the CCM with an ionomer loading higher, than the void volume and can be a contributing factor to the high HFR of the 30 wt.% CCM. However, since the cell is compressed, the CL-PTL could experience sufficient pressure for the PTL structure to pierce a relatively pliable ionomer film on the catalysts surface and come into contact with the particles and establishing electrical contact. Thus this effect is unlikely or only contributes small resistances to the overall HFR and the hypotheses mentioned before are favored to explain the perceived phenomena.

Generally speaking, the difference between compensated and uncompensated potential is fairly important when considering CCM compositions for application-level usages with the caveat of paying special importance to the source of the HFR differences. When the HFR variations are due to the electrical contact between the CL and PTL, different catalyst and PTL materials for application electrolyzers can affect the cell potential differently and the compensated potential can indicate a more favorable setup as Bernt *et al.* discuss in their analysis of CL electrical conductivity.^[93,178] But when the differences, as observed here, are mostly due to inter-particle contact resistances, the uncompensated potential is more important when considering a CCM composition. Thus the 20 wt.% ionomer content displayed here as the most performant one can be used as a benchmark for later consideration of large scale production with Ir black catalysts and as a comparison for the gradient CCMs.

Tafel plots can be constructed from the compensated potential in the low current

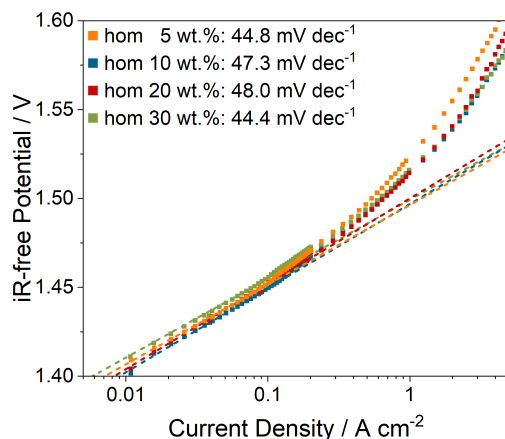


Figure 6.2.4: Tafel analysis of homogeneous and gradient CCMs of iR -free potential with Tafel slopes determined between 10 and 100 mA cm^{-2} .

density range, where solely kinetic aspects of the OER determine the potential. These are displayed for the homogeneous CCMs with varying ionomer loadings in Figure 6.2.4. The Tafel slope indicates the overpotential due to the kinetics of the OER stemming from catalyst properties are generally take values between 40 and 70 mV dec^{-1} .^[135,179] It is apparent, that all CCMs show a comparable Tafel slope, while the 30 wt.% CCM shows the lowest one with 44.4 mV dec^{-1} , compared to 48.0 mV dec^{-1} of the 20 wt.% one. Small variations in this value can be due to uncertainties in the determination of HFR and thus the compensated potential. The lower Tafel slope might indicate a higher ionomer coverage of catalyst particles, which results in more catalytic surface area, which would be in-line with the proposed benefits of a higher ionomer loading, namely increased ionic conductivity and higher ionomer coverage. This is however in contrast to the trend on ECSA, where a linear decrease with ionomer content can be observed with 14.7 and 10.8 $\text{m}^2 \text{g}^{-1}$ for 10 and 30 wt.%, respectively (see Figure 6.2.12 for ECSA values). In general, 10 wt.% ionomer content should display the lowest Tafel slope as observed in other studies but its value is close to the one with 20 wt.% and still higher than the one of 30 wt.%.^[135] This would also be in-line with the ECSA observed but is not reflected in the Tafel slopes. Thus, no clear correlation of the Tafel slope with the ionomer content can be made here and the assumption of similar Tafel slopes for these CCMs with only small variations in its value seems to be most likely. The low Tafel slope of the 5 wt.% CCM is almost as low as the 30 wt.%, which could be a hint at a correlation of the HFR with the Tafel slope as the HFR increases the Tafel slope gets lower. This could be caused by a slight overcompensation of the cell potential at these low currents or an undercompensation with a lower HFR resulting in the different Tafel slopes. Still, the CCMs

characterized show an overall low Tafel slope when compared to other studies, indicating a kinetically very active catalyst and low η_{act} with little impact of the ionomer loading on it. The relative impact of the HFR thus seems to be more pronounced on the overall cell potential than the differences in the Tafel slope or kinetic aspects of the catalyst, providing similar properties of the catalyst between CCMs and only adjusting the ionomer content.

When operating an electrolyzer, the applied current density can induce different kinds of overpotentials and impact them differently. To evaluate the CCMs at different operational points, Figure 6.2.5.a depicts the uncompensated potential depending on the ionomer content of the CCM. As seen in the polarization curves, an

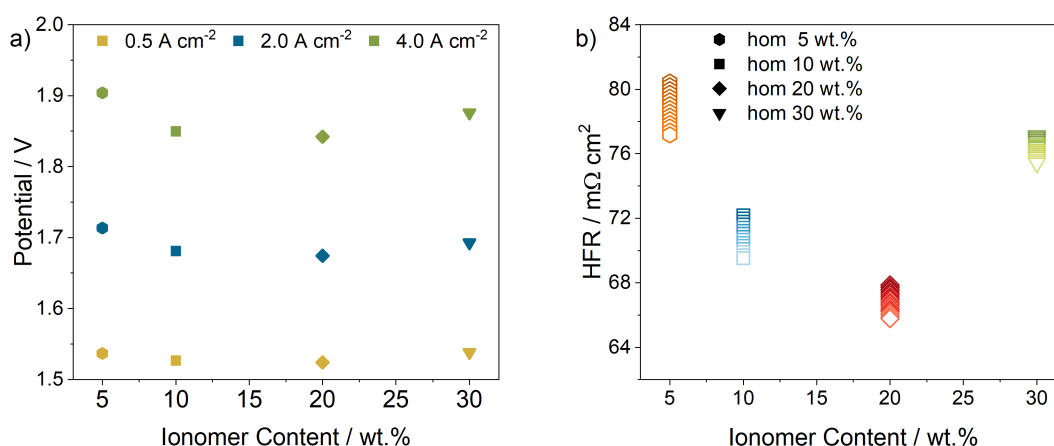


Figure 6.2.5: Parameter comparison depending on the total ionomer content of the homogeneous CCMs of a) uncompensated potential at different current densities and b) HFR values with color gradient indicating the current density (0.0-4.0 A cm⁻²) at which it was calculated (darker color indicating low current density and lighter color indicating high current density).

optimum at 20 wt.% ionomer content appears with 10 wt.% showing only slightly higher potentials. This effect gets exacerbated at higher current densities with the 5 wt.% CCM showing notably lower performance. The potential differences do not increase linearly, but they become more pronounced at higher current, stemming from the current dependent character of the resistance values associated with each overpotential term. However, no apparent jump is visible precluding any additional overpotential terms becoming discernible such as pronounced mass transport or particle detachment. As discussed before, the HFR value has a large impact on the overall cell performance as η_{Ohm} is the largest overpotential term. Figure 6.2.5.b displays the HFR dependence on the ionomer content with the addition of its trend from low to high current densities, displayed as color gradients. The optimal value at 20 wt.% is here even more apparent, than in the polariza-

tion data with differences of more than $10 \text{ m}\Omega \text{ cm}^2$ from the highest to the lowest. The trend following an inverted volcano shape is derived from different structural phenomena in the CL depending on the ionomer content. Some of these were discussed before but the changing HFR value depending on the applied current density is not constant for different ionomer contents. In general, the HFR value is a combination of the electrical contact resistances and the membrane resistance. The membrane resistance should be constant across all measurements as the same membrane was used in all CCMs. In the case for a fully hydrated Nafion[®] 212 membrane at $80 \text{ }^\circ\text{C}$, the membrane resistance is in the range of $41\text{-}54 \text{ m}\Omega \text{ cm}^2$, depending on the expansion direction, whether it is assumed to be isotropical or through-plane.^[12] The electrical contact resistance due to the cell setup and electrical connections can simply be measured by compression of the cell without a CCM in between the PTL and GDL. This leads to a potential difference of 23.9 mV at 3 A cm^{-2} , which corresponds to a resistance of $31 \text{ m}\Omega \text{ cm}^2$, totaling to a resistance range of $72\text{-}85 \text{ m}\Omega \text{ cm}^2$, which is well within range of the measured values, when considering isotropic membrane swelling and thus the lower membrane resistance value. Small differences from these predicted values can occur such as better contact area between the CCM and the PTL / GDL compared to the PTL and GDL directly. Only the 20 wt.% ionomer CCM shows a HFR lower than the predicted value, probably due to the aforementioned effects. Values higher than that of the 20 wt.% CCM then are probably caused by electrical contact resistance between catalyst particles and at the CL/PTL interface. Higher HFR values at lower ionomer loading was so far not reported in literature but it could be caused by inhomogeneities in the CL as the ionomer binder is not sufficiently distributed across all particles as was observed for very low loading CL.^[180]

The dependence of the HFR with the applied current density was observed before and is most likely the result of increased local temperatures with higher reaction rates at higher current densities, which leads to a higher membrane conductivity.^[176,180] Since the decrease of the HFR value here is higher than in similar studies, it can be assumed that the membrane might not be sufficiently equilibrated and slightly lower in temperature than the set $80 \text{ }^\circ\text{C}$. This dependence on the current density is approximately the same for all CCMs with -0.06 to $-0.07 \text{ m}\Omega \text{ A}^{-1}$ while the 30 wt.% CCM displays a HFR dependence of $-0.03 \text{ m}\Omega \text{ A}^{-1}$. An increasing HFR with current density was observed by Bernt *et al.* in an electrolyzer and by Springer *et al.* in a fuel cell.^[180,181] They explained the phenomenon with a decrease in local water content near the CL-membrane interface. Here, the electroosmotic drag of the membrane from the anode to the cathode transports water

quicker than it can diffuse through the CL creating water starved areas within the CL and thus increasing the HFR. In conjunction with the higher water consumption rate in an electrolyzer, the reactant starvation becomes more likely. This effect is especially prevalent for thicker CLs as the water has to diffuse through longer paths in order to reach the membrane. The water consumption does not only increase at high current densities but the product gas formation also increases, which hinders the water transport even further. When increasing the operation pressure, leading to lower O₂ volume inside the CL, Bernt *et al.* observed the disappearance of this phenomenon, strengthening their hypothesis.^[180] Since the void pore volume of the 30 wt.% CCM approaches zero, the water transport is further diminished, probably leading to this effect. It is also independent of the water flow rate, which is quite high in this work at 500 mL min⁻¹, as the water only flows over the CL and is not forced into it. While the increasing temperature increases the membrane conductivity, the water starvation in the 30 wt.% CCM lower electrical conductivity and results in an overall decreasing HFR but at a lower rate compared to the other CCMs.

The protonic transport resistance is a key metric for the variation of ionomer observed here as it is directly dependent on the amount of ionomer and its film thickness along with catalyst particle coverage. Calculated R_{Ion}^{CL} values are presented in Table 6.2.1.

Table 6.2.1: Contributions of anodic R_{Ion}^{CL} for the different homogeneous ionomer loading CCMs.

Ionomer loading	$R_{Ion}^{CL} / m\Omega \text{ cm}^2$
5 wt. %	4.7
10 wt. %	3.1
20 wt. %	1.7
30 wt. %	2.3

Since the ionomer content influences the coverage of catalyst particles with polymer and the thickness of the ionomer film, the ionic conductivity is generally dependent on this parameter.^[115,177] This dependence is exemplified by the values for R_{Ion}^{CL} observed in the homogeneous CCMs. It is initially high for low ionomer loadings and again follows the trend of an optimum at 20 wt.%. Unexpectedly, R_{Ion}^{CL} increases again at higher ionomer loadings at 30 wt.% as the additional ionomer should only contribute to a thicker film, which at least is as conductive as in the

20 wt.% CCM. DeCaluwe *et al.* investigated thin Nafion[®] films and observed, that the initial film is composed of a lamellar structure that is a few nanometers thick but transitions to a bulk-like phase at higher loadings.^[182] This bulk-phase is similar in properties to a membrane and should not increase in ionic resistivity at higher thicknesses. One possible explanation for this phenomenon is diminishing water content inside the polymer, leading to a lower conductivity. It was observed before, that the water content might decrease at higher current densities during operation but the values measured here were taken at 1.2 V vs. RHE, where no faradaic processes occur and the CL is at maximum hydration level. Other studies report a pressure-dependent water uptake of Nafion[®] membranes, where not only the water content inside the polymer but also its diffusion coefficient decrease under increased mechanical pressure.^[183] This is explained by the structure of Nafion[®] ionomer, which is comprised of a hydrophobic polymer backbone and hydrophilic sulfonic acid groups, which form channels upon water uptake. The acid groups lead to the conduction of protons along these channels. Upon mechanical compression, the water-rich channels might be compressed and discharge water leading to an overall lower water uptake and thus also lower protonic conductivity. As the void volume of the CL approaches zero already at ionomer loadings below 30 wt.% one can assume the pores are completely filled with ionomer at this loading in a wet state of the CCM. When introduced to the electrolyzer cell and hydration of the water, the ionomer inside the pores swells further but might be constrained in the pores due to the rigid structure of the catalyst. This effect could lead to the same phenomenon as observed by El Kaddouri *et al.*, where the ionomer is put under mechanical compression and the water uptake is hindered.^[183] This is also corroborated by the conclusions, that ionomer films form bulk-like structures akin to a membrane, which explains its behavior even inside the pores. If one assumes, the comparatively lower HFR decrease with current density of the 30 wt.% CCM is caused by local water starvation, the hypothesis of limited water transport through the ionomer seems more likely. Even though the differences in R_{ion}^{CL} are small, these two independently observed phenomena point to the same conclusion. The void pore volume of roughly 35 % for the 20 wt.% ionomer content CCM might present the optimum as the ionomer is not put under mechanical compression inside the pores but leads to an overall thicker film on the particles compared to the CCMs with a lower ionomer content.

The overall breakdown of the overpotentials in a given CCM can visualize the magnitude of each loss and show additional losses not considered in the overpotential analysis. The protonic conductivity of the CL can be considered as a significant overpotential contribution. However, there is a distinction between the

measured R_{Ion}^{CL} due to in-plane hindrance of the protonic transport through the ionomer and the overpotential contribution to the cell potential.^[12,184] The effective ionic CL resistance (R_{Ion}^{eff}) can be calculated according to equation 6.2 with the kinetic correction factor (ξ) calculated from the ratio of the ionic sheet resistance and the kinetic resistance (b) represented by the Tafel slope. Mathematical derivation of equation 6.2 has been shown by Neyerlin *et al.* and describes the potential gradient in the CL, due to proton conduction as a function of the local OER current.^[184]

$$R_{Ion}^{eff} = \frac{R_{Ion}}{3 + \xi} \quad (6.2)$$

With ξ being represented by equation 6.3.

$$\xi = \frac{i R_{Ion}}{b} \quad (6.3)$$

Values for η_{Ion} are thus calculated using the R_{Ion}^{eff} in dependence of the applied current density. The breakdown for all homogeneous CCMs is displayed in Figure 6.2.6. Some of the overpotential contributions have already been discussed

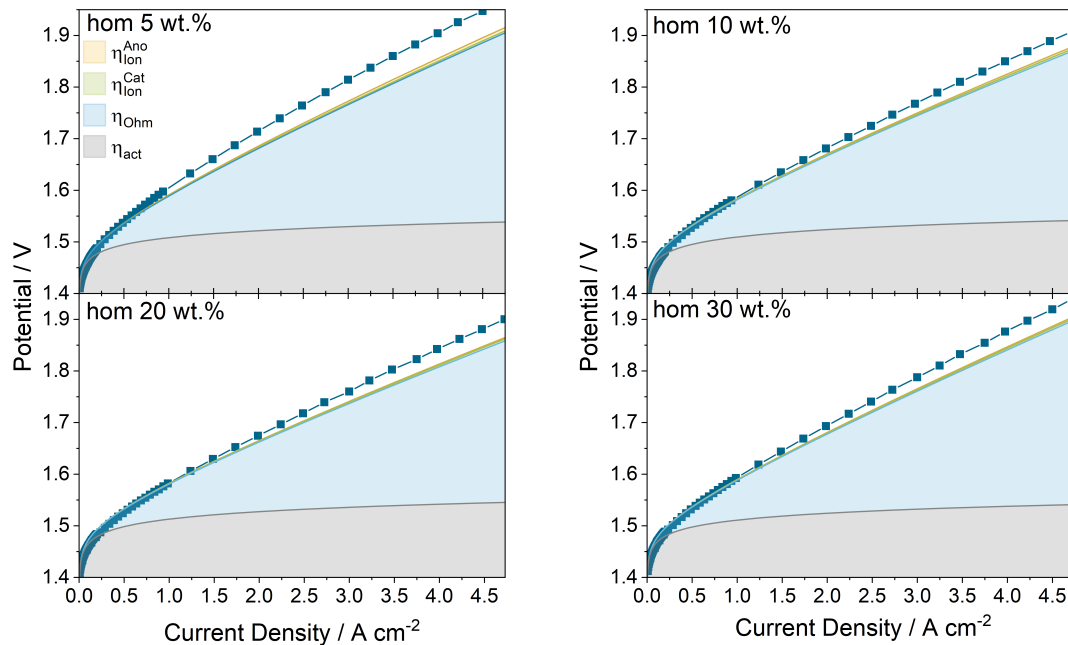


Figure 6.2.6: Overpotential breakdown of homogeneous CCMs with different overpotential contributions indicated. Cathodic η_{Ion} is an estimation of $2.5 \text{ m}\Omega \text{ cm}^2$ according to Bernt *et al.*^[12] and is constant in all CCMs.

in the differences in the HFR and Tafel slopes influencing the η_{act} for all different ionomer loadings. The η_{act} was calculated according to equation A.3, which is a rearranged form of equation 3.8.^[48] The kinetic OER parameters i_0 and the Tafel slope were determined in the low current density areas, where no other overpotential contributions are present besides η_{act} and the overpotential term calculated for the whole current density range. The contribution from the cathode is generally smaller than those of the anode as the HER is considered to be much faster and contribute less than 1 mV at 3 A cm⁻² or about 0.29 mΩ cm².^[12,42,180] This amount of resistance is negligibly small considering the additional overpotentials originating from different effects. The remaining overpotential terms of the cathode come down to ionic and mass transport contributions as the electrical conduction losses are already present in the HFR measured on the whole cell. With the use of a reference electrode a dissemination of individual HFR proportions can be made but is not possible with the setup at-hand and thus out of scope for this work.^[185] The contact resistance for Pt/C catalyst is usually very small as the C support particles are good electrical conductors and a proven material in fuel cell applications. Ionic conductivity inside the cathode CL can increase the potential slightly as Bernt *et al.* found an R_{Ion}^{CL} of 2.5 mΩ cm² in their work. This contribution is on-par with the overpotential terms of the anode and are shown in green in Figure 6.2.6.^[12]

The R_{Ion}^{CL} is usually accredited as a contribution to η_{MT} as the ionic transport can vary with operation conditions and can result in a hindrance at large current densities.^[10,177] The unassigned overpotential is considered to be stemming from the η_{MT} without η_{Ion} , as this was obtained separately and can thus be deducted. Bernt *et al.* also analyzed the contribution of the cathodic η_{MT} to the cell potential and found approximately 20 mV at 3 A cm⁻², which matches the values observed here for unassigned overpotential.^[12] The exact contribution of the cathodic η_{MT} can not be determined here as the technique requires a pressurized operation, where the volume of the H₂ gets lower and differences between the polarizations can be used to estimate the pressures influence on the unassigned overpotential and thus η_{MT} . As the apparent anodic η_{MT} is negligible for almost all ionomer contents, the hypothesis of Bernt *et al.* gets more favorable, where anodic η_{MT} only gets dominant at higher layer thicknesses and loadings.^[180] They observe tangible contributions at Ir loadings of 4-5 mg_{Ir} cm⁻², which is noticeably higher than the loadings used here at 1 mg_{Ir} cm⁻². Interestingly, at lower ionomer contents of 50 wt.% an increase in η_{MT} can be observed. This might be caused by a larger void pore volume which is filled with water and gas transport is more dampened here as the gas pressure is not sufficient to crack the CL but rather experience slow transport through water-filled pores. However, the behavior of two-phase

flow inside CL pores is still poorly understood and definite hypotheses are difficult to formulate without more data.^[95,180] O₂ transport probably mostly takes place in pores at low ionomer contents but shifts to cracks in the CL as discussed before as the pore volume decreases and this effect is already noticeable in the HFR, which is why the anodic η_{MT} does not change significantly with ionomer content.

6.2.2 Influence of Ionomer Gradient Design

The proposed gradient design with an ionomer variation along the thickness of the CCM can yield several advantages by combining positive aspects of the homogeneous loadings. Properties could thus be distributed throughout the layer where they can offer the most performance increases and can generate additional insights of the ionomer content in CCMs. In order to provide a substantial difference between the ionomer contents, two different gradient CCMs were coated in alternating directions. First a 30 wt.% layer was coated onto the membrane and then a subsequent layer with 10 wt.% was applied on top. The higher ionomer content near the membrane is supposed to improve ionic conductivity where the reaction rate is highest and offer additional void pore volume near the PTL to facilitate water and gas transport. The same setup in reversed order was also coated to facilitate insights into the proposed effects when considering the reversed setup.

The actual ionomer content inside a CCM can not only be assumed from the ink composition and the ionomer mass fraction. Even though this is already a quite good estimate for a homogeneous and stable ink, the final ionomer content can vary and thus need to be externally validated, for example by determining the relative ionomer mass through thermal decomposition.^[99] This can be achieved through TGA, where the ionomer is fully oxidized to gaseous products under O₂ atmosphere. Each CCM component is oxidized at different temperatures, hence the relative weight of each material can be calculated. The decomposition profile for CCMs with homogeneous and gradient ionomer contents are presented in Figure 6.2.7. Decomposition of Nafion[®] ionomer takes place up to a temperature of 400-450 °C, when the majority of the ionomer has left the sample. The relative weight loss for each CCM correlated well with the desired ionomer content, where the minimum relative weight is approximately its weight fraction. At the minimum relative weight, not only the ionomer decomposition but also oxidation of Ir under addition of O₂ can be observed, which is superimposed on the Nafion[®] weight loss. The bulk of the Ir oxidation is visible at higher temperatures, which implies a low to negligible amount of O₂ mass addition before complete ionomer decomposition. Interestingly, it can be observed, that the gradient 10|30 wt.% CCM shows

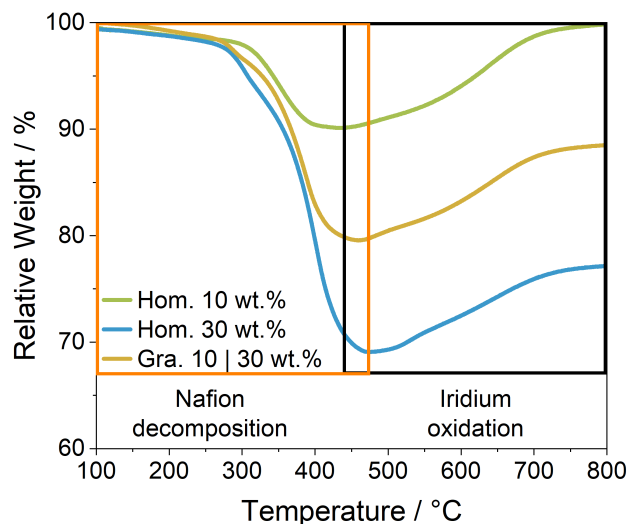


Figure 6.2.7: TG analysis to determine the ionomer content of Ir black CCMs through ionomer decomposition in O_2 atmosphere.

an average ionomer content of roughly 20 wt.%, which is the expected average for the whole layer and thus in good agreement with the desired overall content.

In order to validate not only the overall ionomer content of the gradient layers but also its distribution, SEM and EDS images were recorded, to map elemental contents across the layers thickness. The recordings for the gradient 10|30 wt.% CCM are presented in Figure 6.2.8. The overall Ir content can be seen to be well distributed across the whole CCM with a total thickness of $3.8 \mu\text{m}$. Both the line-profile and composition mapping show an even distribution with only slight variations, that can be caused by either or a combination of noise in the measure-

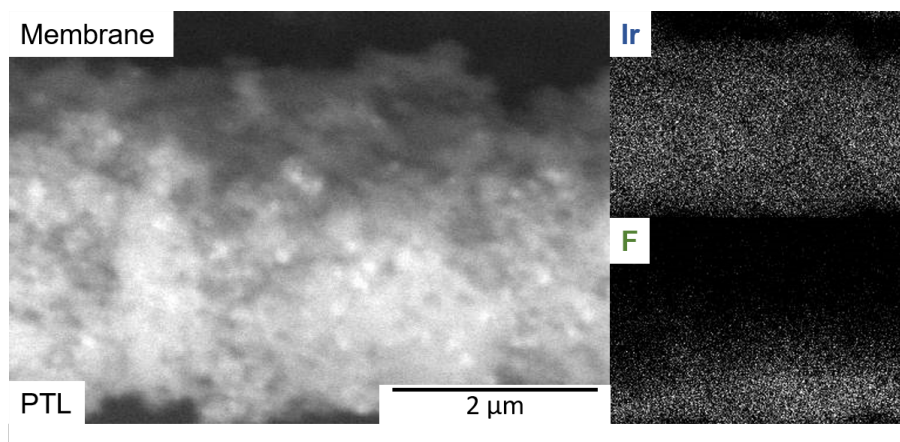


Figure 6.2.8: Cross-sectional SEM and EDS images depicting the 10|30 wt.% gradient CCM with Ir and F elemental mappings in arbitrary units along with the SEM image.

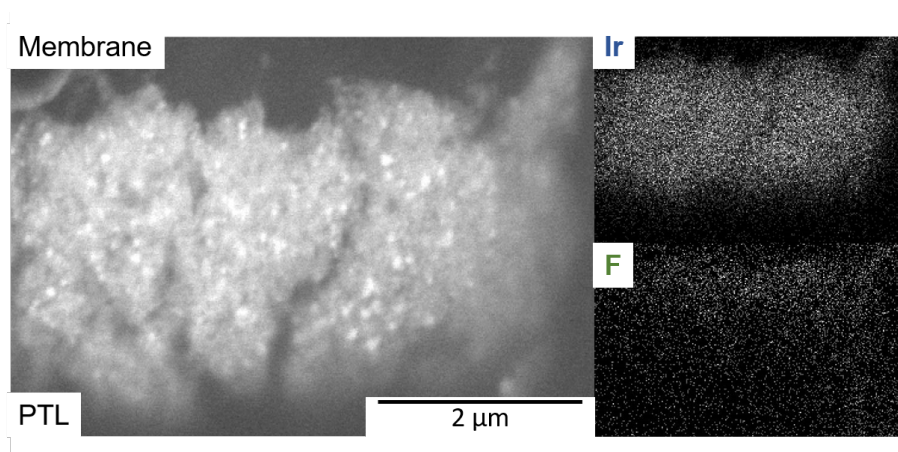


Figure 6.2.9: Cross-sectional SEM and EDS images depicting the 10|30 wt.% gradient CCM with Ir and F elemental mappings in arbitrary units along with the SEM image.

ment data or minor differences in cross-section height and thus more material at one point. In contrast, the elemental mapping of F shows a clear increase of material towards the PTL side of the CCM, which is in good agreement with the desired composition. F acts as a proxy for the ionomer in this case, as it is comprised of F to a large amount. This distribution of the F intensity confirms the composition gradient that was attempted to be made realized. A quantitative analysis of the specific contents of F and Ir is not possible here, as the adjacent membrane also contributed to the detected F signal. The mass contents for each were determined to be 31 wt.% F and 59 wt.% Ir, resulting in an overall CCM composition of 43 wt.% ionomer and 57 wt.% Ir, which is not in-line with previous results and thus deemed not reliable due to the aforementioned reason.

Polarization data are presented in Figure 6.2.10.a of both gradient CCMs in addition to the homogeneous ones to exemplify the impact of the gradient effect. The unanticipated difference can be seen clearly in the performance as the 30|10 wt.% CCM with the 30 wt.% sublayer at the membrane, shows a lower performance than its 10|30 wt.% CCM counterpart. The cell potential is also higher than the homogeneous 10 and 20 wt.% CCMs, whereas the 10|30 wt.% CCM demonstrate the highest performance among all measured CCMs. This is unanticipated as the proposed positive effect of the grading appear in reversed order. It is further remarkable, that a gradient CCM shows even lower cell potential than the previously presumed optimum ionomer loading at 20 wt.%, even though the average content of the gradient CCMs is 20 wt.%, thus indicating additional effects present when a gradient design is applied. Additional insight can be derived from the compensated polarization data in Figure 6.2.10.b, where the 10|30 wt.% CCM eclipses all

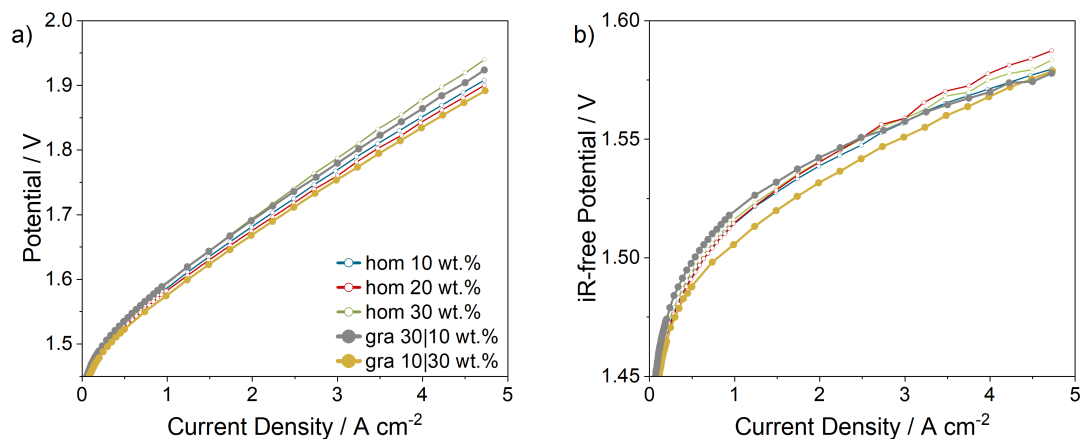


Figure 6.2.10: Polarization curves for homogeneous and gradient CCMs with a) uncompensated and b) HFR compensated potential and gradient CCMs highlighted.

other samples in performance, especially at lower current densities. At higher current densities, the potential reaches that of 10 and 30 wt.% CCMs, which hints at a lower HFR, that does not lower the iR-free potential sufficiently at very high current densities. This behavior is also exemplified by the 20 wt.% CCM, suggesting similar layer properties between the two in terms of HFR. A higher performance at lower current densities might suggest a lower η_{act} but this difference can not be observed in Tafel slopes as it shows a slope of 45.5 mV dec^{-1} and matches well with the others. However, its i_0 is higher than for the others which might explain the difference at low current densities (refer to Table A.6). The iR-free performance of the 30|10 wt.% CCM is again lower as one would expect with the caveat of an equal cell potential at 4.5 A cm^{-2} compared to the 10|30 wt.% CCM. This again is caused by the higher HFR of the 30|10 wt.% CCM, becoming more pronounced at higher current densities.

The difference in performance at certain current densities is again depicted in Figure 6.2.11.a. Difference between the gradient 10|30 wt.% and the optimal ionomer loading at 20 wt.% is even apparent at low current densities, even though small. This shows the kinetic advantages of the gradient CCM, observed in the uncompensated polarization. The difference between the two does not significantly increase at higher current densities, suggesting similar additional overpotential terms, such as η_{Ion} and η_{Ohm} . 30|10 wt.% gradient loading is on-par with the 30 wt.% homogeneous CCM, suggesting a larger impact of the ionomer loading near the membrane, compared to just the average value. Lower performance of the 30 wt.% sublayer is thus indicative for the overall performance. When comparing the HFR values for the different gradient and homogeneous CCMs, it be-

6.2 Ionomer Gradient CCMs

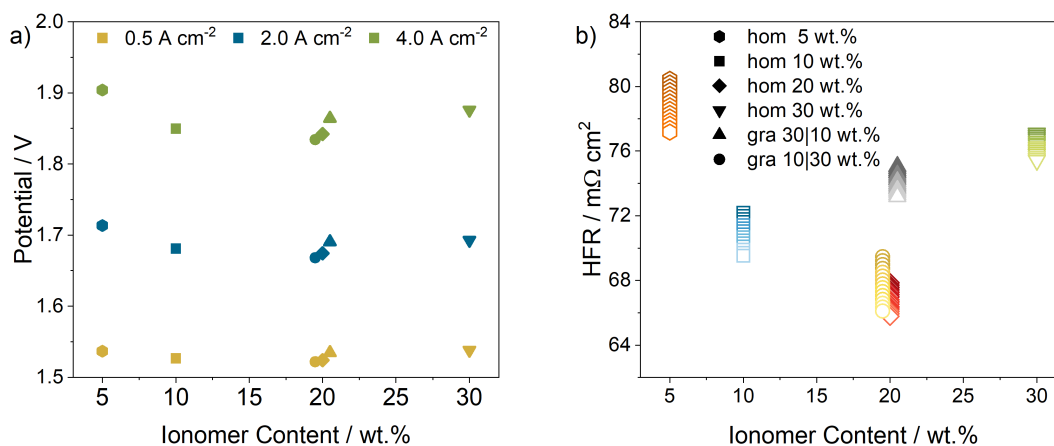


Figure 6.2.11: Parameter comparison depending on the total ionomer content of the homogeneous or gradient CCMs of a) uncompensated potential at different current densities and b) HFR values with color gradient indicating the current density at which it was calculated (darker color indicating low current density and lighter color indicating high current density).

comes apparent, that the lower HFR of the 10|30 wt.% CCM is comparable to the 20 wt.% one with it decreases more depending on the current density. This suggests, that the effect of water starvation near the membrane, as discussed before, does not occur to such an extent here as with a homogenous loading of 20 wt.%. The higher void pore volume near the membrane could thus lead to a better water transport and diminishes the effect of an increasing HFR. In contrast to this, the 30|10 wt.% CCM shows an current density dependency akin to the homogeneous 30 wt.% one, suggesting a similar ionomer morphology near the membrane. This might also explain the relatively high HFR overall as it is about 8 mΩ cm² higher compared to the average ionomer content. A higher ionomer content near the membrane might isolate catalyst particles, leading to lower electrical contact. This phenomenon might however not occur in the 10|30 wt.% CCM as the HFR is almost as low as the 20 wt.% one, which could be caused by better distribution of the ionomer during the coating process. Some of the polymer might be transported into the 10 wt.% sublayer as the void pore volume is still about 60 %, hence avoiding isolating parts of the catalyst layer with excess ionomer. This process could generally be beneficial for spray-coated CCMs with a more accessible sublayer near the membrane, getting intruded by material from higher sublayers.

One of the proposed benefits of a high ionomer loading in a sublayer is the increased ionic conductivity, represented in Figure 6.2.12.a. In contrast to the observations made before in regards to the 30|10 wt.% CCM experiencing negative

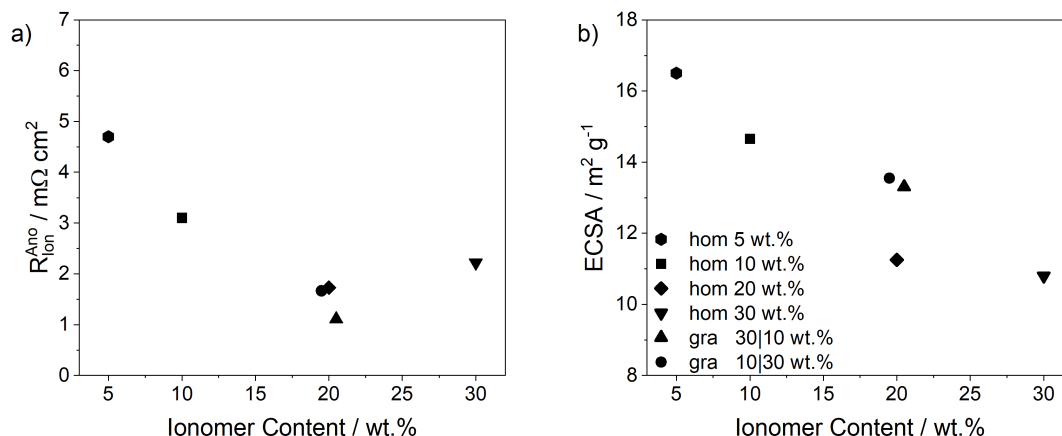


Figure 6.2.12: Ionomer loading dependent visualization of a) the anodic R_{ion}^{CL} and b) the ECSA, calculated before the conditioning period.

effects of the higher ionomer loading near the membrane, the anodic R_{ion}^{CL} does not increase substantially to the value of the homogeneous 30 wt.% CCM. In fact, it shows an even lower value than the 20 wt.% CCM and the other gradient one. As discussed before, the effect of ionomer compression probably leads to the high R_{ion}^{CL} of the 30 wt.% layer but this does not occur here. The accessible void volume of the 10 wt.% sublayer might provide enough volume for the ionomer to expand into as it swells, avoiding excessive compression and water discharge. Here, the high ionomer content provides additional ionic conductivity compared to the 20 wt.% without the detrimental phenomena. The 10|30 wt.% CCM shows an R_{ion}^{CL} of the average ionomer loading, indicating to additional benefits in this regard from the grading of ionomer. It is remarkable, that R_{ion}^{CL} of the 30|10 wt.% CCM is increased by a relatively large amount compared to the other gradient one, but an overall small benefit compared to all other overpotential contributions. This shows a clear benefit of a higher ionomer content near the membrane in terms of R_{ion}^{CL} but does not improve the overall performance observed here, since other effects are larger.

ECSA can be used as an estimate of the accessible catalytic sites inside a CL as it describes the sites exposed to the electrolyte and in electrical contact. For metallic Ir catalysts, the H_{upd} can be used as a proxy to calculate the ECSA.^[91,186] Here, H gets adsorbed on the metallic Ir surface sites and the charge resulting from this process can be used to calculate the ECSA. This however, only occurs, when the surface is not oxidized, thus the measured ECSA gets reduced once the catalyst is exposed to electrolysis operation potentials. The calculated ECSA for all CCMs, depending on its ionomer content is depicted in Figure 6.2.12.b. It

is apparent, that the ECSA is proportional with the increasing ionomer content, with the lowest amount of ionomer, representing the highest ECSA. This is expected behavior, as an increasing ionomer content can lead to more electrically isolated particles, which then are not participating in the adsorption process. As the catalyst is in contact with liquid water even, when no ionomer is present on the particle, a H_{upd} should still take place as protons can be provided by the liquid water, which are still present even in ultrapure form. The ECSA is thus no indicator for a ionomer coverage of the catalyst. Normally, a higher ECSA is associated with higher kinetic performance of the CCM as more catalytically active sites simply lead to higher reaction rates but this correlation can not be observed here as it would suggest the 5 wt.% CCM shows the lowest potential at low current densities. No clear trend can be observed between the ionomer loading and kinetic parameters, hence no causation with the ECSA established. This might be caused by surface adsorbed species in the unconditioned CCM, which inhibit the H_{upd} but the ECSA is already reduced after the conditioning period, when surface species might be removed, due to the oxidation of the catalyst. The decreasing ECSA with ionomer content is however in line with the observed differences in HFR at least to point, without considering the additional HFR impacting effects. The overall breakdown of individual overpotential contributions are presented in Figure 6.2.13. The unassigned potential, which could be considered as a η_{MT} con-

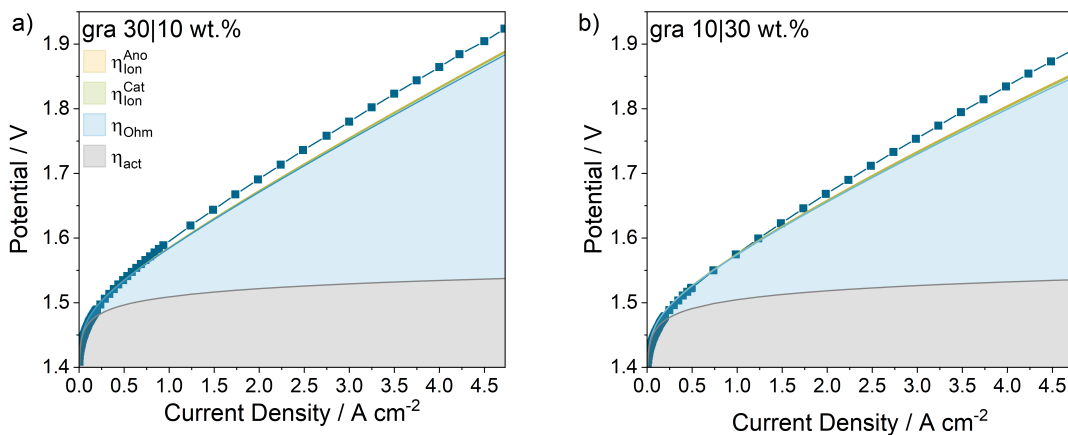


Figure 6.2.13: Overpotential breakdown of gradient CCMs with different overpotential contributions indicated. The cathodic $R_{\text{ion}}^{\text{CL}}$ is an estimation of $2.5 \text{ m}\Omega \text{ cm}^2$ according to Bernt *et al.*^[12] and is constant in all CCMs.

tributions, both from H_2 and O_2 transport at both electrodes, seems to take effect at different current densities for both gradient CCMs. It the cell potential starts to deviate from the calculated potentials at roughly 1 A cm^{-2} for the 30|10 wt.% and around 2 A cm^{-2} for the 30|10 wt.% CCM. The mass transport hindrance might be

caused by the lower void pore volume near the membrane, where the maximum reaction rate is situated. Additionally, the inhomogeneous distribution within the CL could induce additional η_{MT} as both gradient CCMs show higher unassigned potentials than the homogeneous 10 and 30 wt.% ones. In general, the unassigned potential is rather small in comparison to the other losses observed but are slightly higher for the gradient CCMs. This might also be caused by inconsistent determination of the other overpotential terms, as the inhomogeneous CL could influence the accuracy of the measurement protocols.

The spatial reaction rate distribution of a CL is dependent on the electrical conductivity of the catalyst, as Moore *et al.* described.^[95] Considering, the highly conductive Ir black catalyst here, the reaction rate maximum occurs near the membrane. On one hand, CL areas near the membrane can benefit from higher ionic conductivity at a higher ionomer loading but on the other hand negative effects of the high ionomer content are here even more detrimental. This is especially true for the 30|10 wt.% CCM, where the ionomer filled pores induce more potential losses and are negatively affecting the performance. These include losses in electrical conductivity as the ionomer can block some catalyst particles and possible water starvation in near-membrane areas of the CL. The highest performance among all CCMs was observed for the gradient 10|30 wt.% CCM, even higher than the optimum homogeneous ionomer loading at the average of the two sublayers. This is a definite advantage for the gradient design, even when the observed advantages are small. It could indicate benefits from a gradient-based coating process where some of the detrimental effects of one sublayer's ionomer loading are counteracted by the other sublayer. When an ionomer gradient is considered, the exact loadings of each sublayer should be carefully optimized as the chosen 30 wt.% here could be dampening the positive effects of the gradient design due to the phenomena observed in a low void pore volume CCM.

6.3 Catalyst Loading Gradient CCMs

The concept of a CL gradient with a variable Ir loading along its thickness is the first design to be evaluated here. With a variable content of active catalyst particles, distributed on an inert support material the influence of the reaction rate can be optimized along the CL's thickness with ideally identical dimensions and properties of the CL's rigid structure. For this three different catalysts have been synthesized according to the results presented in section 6.1 with an Ir content of 15, 40, and 65 wt.% (m_{Ir}/m_{total}) on the ATO support. Thus the catalyst resulting from the MAF synthesis was chosen and is scaled up to produce sufficient material for the coating of CCMs. For this, the mass of ATO is held constant in all CCMs, in order to keep the structure the same across different characterizations. After the optimization of the ionomer content with a single Ir loading catalyst, this amount of ionomer is referenced to the amount of ATO in the CL and then held constant across different Ir loading CCMs.

6.3.1 Optimization of Ionomer Content

The ionomer content of a CCM has a large impact on the performance of the CL, mainly due to its influence on the protonic conductivity and thus η_{ion} but also its role in the ratio of occupied to void pore volume, hence impact on mass transport and water distribution.^[10,12] As different catalysts form varying structures in a CL, the content of ionomer has to be carefully optimized in order to not only produce high performance but also to highlight differences in other properties of the CL. This is of special importance when considering the impact of a gradient loading of catalyst mass. Considering previous works, the optimal ionomer loading for IrO₂-based catalysts was found to be roughly 10 wt.% in regard to the total mass of the CL for comparable catalysts.^[12,96] Differences to previously discussed optimal ionomer loadings for Ir black-based catalysts might lie in the denser nature of metallic Ir, where the ionomer might have a similar film thickness and catalyst coverage at different relative weight amounts. Nonetheless, this optimal ionomer loading for IrO₂ catalysts has to be reproduced and re-optimized for individual catalyst systems, especially when a support material is added as is the case here. Considering previous works in this field, the different amounts of ionomer content were chosen to be 5, 10, and 15 wt.%. Uncompensated polarization data of these CLs is displayed in Figure 6.3.1. As previously observed, the 10 wt.% ionomer content CCM shows the lowest potential across the whole current density range and can be reproduced as the optimum loading here.^[12,96] The lower ionomer con-

6.3 Catalyst Loading Gradient CCMs

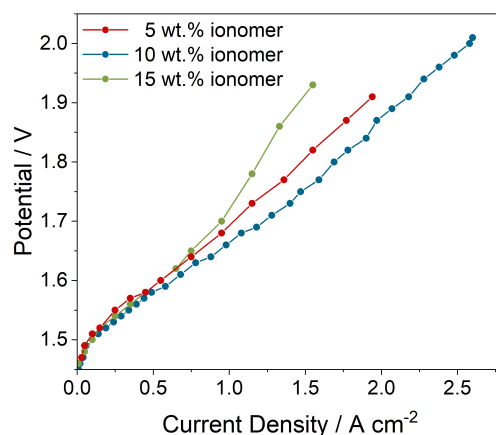


Figure 6.3.1: Polarization of homogeneous 40wt.% IrO₂/ATO CCMs with varying ionomer loadings.

tent of 5 wt.% also shows quite high performance only deviating from the 10 wt.% one slightly. This behavior was also observed by Bernt *et al.*, where their loading of even 3.9 wt.% shows almost identical performance to their 11.6 wt.% one, which was the optimal loading. Only at higher ionomer loading the performance starts to deteriorate, which is attributed to an increase in HFR at contents above 20 wt.%. An increase likely stems from electrically isolated catalyst particles, due to a thick ionomer film. This trend could not be observed here, as the highest ionomer loading was 15 wt.% and no substantial difference between the HFR at 5 and 15 wt.% ionomer can be observed, see Figure 6.3.2. The CCM with 15 wt.% shows an

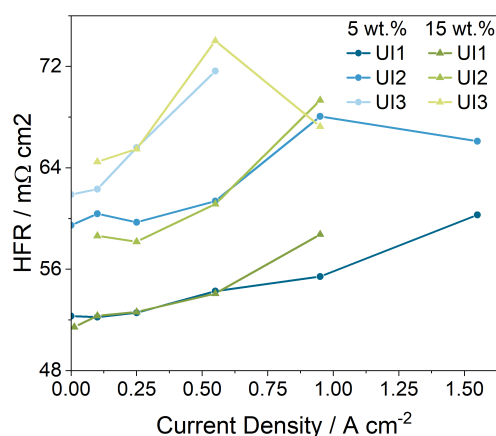


Figure 6.3.2: Influence of sequentially recorded polarization curves on the HFR for 40 wt.% IrO₂/ATO CCMs with 5 and 15 wt.% ionomer loading ($m_{ion}/m_{ion} + m_{cat}$).

upward arc around 1 A cm⁻², which might be attributed to a jump in η_{MT} but these measurements have to be carefully evaluated, due to non-optimal operation with the insufficient water purification during their measurements. A relatively high con-

tamination of the water supply in the testbench leads to a decrease in the HFR, as the Nafion[®] ionomer in both the membrane and CL gets deactivated with metal cations, especially alkali metals.^[64] This increase can be observed in the HFR in Figure 6.3.2, as the HFR rises even after a short measurement time between multiple polarization experiments within 30 minutes. Thus the observed increase in the 15 wt.% ionomer CCM could very well be caused by inactivated ionomer.

Nonetheless, the performance data for the different ionomer contents reproduced the behavior observed in other studies, even with non-supported catalysts. As the optimal performance can be observed at 10 wt.% ionomer content, this value is then taken as the optimum. For these measurements a 40 wt.% Ir on ATO catalyst was used and the ionomer content referring to the whole CL at 10 wt.% corresponds to 18.5 wt.% referring just to the ATO. This ionomer loading is then used in all further experiments involving the IrO₂/ATO catalyst.

6.3.2 Influence of a Varied Ir Loading in IrO₂/ATO CCMs

Prior to the characterization of gradient design CCMs, individual contributions of overpotentials by homogeneous CCMs with the same catalysts have to be carefully evaluated. In order to provide comparability and references to the gradient CCMs, the homogeneous CCM are coated with the same catalyst in two different overall catalyst loadings to one provide a comparison to a CL that is identical to each sublayer of the gradient CL and two is comparable to the total loading of the gradient one with both sublayers combined. This leads to a sample setup of CCMs with 0.6 mg_{ATO} cm⁻² and 1.2 mg_{ATO} cm⁻² for each catalyst.

In a first approach, these CCMs are characterized in the testbench and the uncompensated polarization data for these presented in Figure 6.3.3. It becomes apparent, that the performance of these CCMs is sub-par compared to Ir black catalysts with significantly higher potential across the whole current density range. Especially, the CCM with the 15 wt.% IrO₂/ATO catalyst shows very poor performance without reaching 0.5 A cm⁻² below 2 V. Performance of both catalysts at 40 wt.% Ir loading is comparable with the one with lower loading showing slightly higher potentials. This might indicate that a higher Ir loading in these layers leads to an enhanced performance. Generally, the performance is quite low and most likely not representative of these catalysts. This big increase in cell potential is probably caused by a large HFR, which stems from electrical inter-particle resistance. Impedance spectra of these layers are depicted in 6.3.3 and show impedance arcs at very high resistance values. This behavior was observed by Bernt *et al.*

6.3 Catalyst Loading Gradient CCMs

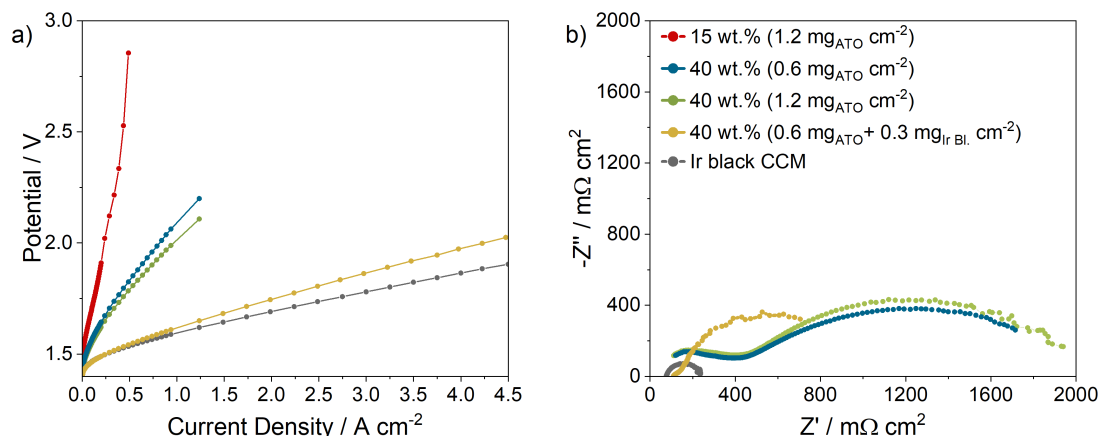


Figure 6.3.3: Performance of homogeneous IrO₂/ATO CCMs with a Ir black reference CCM in a) uncompensated polarization data and b) EIS spectra recorded at 25 mA cm⁻².

and theorized to be stemming from insufficient electrical contact between the PTL and a low-conductivity catalyst.^[180] Absence of a low-frequency arc in the Nyquist-plot does not allow for an accurate description of the HFR but is speculated to be around 400 mΩ cm², which is a 5-fold increase compared to usually observed values. This substantial difference might be caused by insufficient electrical contact between IrO₂ particles, which is exacerbated at low Ir loadings. The ATO support seem to provide poor electrical conductivity, leading to the low performance overall. Thus the electrical conductivity of the CL needs to be improved and to this end a fixed amount of highly conductive Ir black was added to the CCMs. Ir black addition to the CL dilutes the effect of the variable loading on the ATO but is necessary to provide reliable CLs with enough electrical in-plane conductivity to display differences in other overpotential terms besides the electrical conductivity contribution to η_{Ohm} . Beneficial effects of the addition is clearly visible in both the polarization data and impedance spectra, where the performance of the IrO₂/ATO+Ir black CCM is comparable to that with only Ir black at least in the low current density region and only slightly lower in the higher regions. Additionally, a high-frequency arc can be seen in the Nyquist-plot, that intercepts the Z' axis and shows a moderately higher HFR compared to the Ir black reference but still much lower than the pure IrO₂/ATO CCMs. In addition to the electrochemical benefits of the Ir black inclusion, the coating process is more reliable as the ink is more stable and leads to less agglomeration and clogging of the spray-coater. This also leads to a more homogeneous morphology of the CL, which allows for better comparability between samples of differing IrO₂ on ATO loadings.

All ensuing CCMs consist therefore of the IrO₂/ATO catalyst and a fixed amount

of Ir black, resulting in a constant mass-based ratio of 2:1 (ATO/Ir black). These are referred to as high ($1.2 \text{ mg}_{\text{ATO}} \text{ cm}^{-2}$) and low ($0.6 \text{ mg}_{\text{ATO}} \text{ cm}^{-2}$) loading CCMs in the following results and discussion. This setup of CL compositions leads to a varying Ir loading in the overall CCM according to Table 6.3.1.

Table 6.3.1: Compositions and overall Ir loading of the IrO_2/ATO CCMs.

CCM	$m_{\text{ATO}} / \text{mg cm}^{-2}$	$m_{\text{Ir black}} / \text{mg cm}^{-2}$	$m_{\text{Ir, total}} / \text{mg cm}^{-2}$
IrO_2/ATO 40 wt.% low	0.6	0.3	0.7
IrO_2/ATO 40 wt.% high	1.2	0.6	1.4
IrO_2/ATO 65 wt.% low	0.6	0.3	1.4
IrO_2/ATO 65 wt.% high	1.2	0.6	2.8
Ir black reference	-	1.0	1.0

Performance of the IrO_2/ATO layers is quite comparable to the Ir black reference, confirming the reliance on sufficient in-plane electrical conductivity for good performance in a CL. Polarization data of the variably loaded IrO_2/ATO CCMs are presented in Figure 6.3.4.a. Especially the low current density is comparable across all measured CCMs with not apparently large difference in the uncompensated potential in this range. This indicates, a high kinetic activity of the IrO_2/ATO catalyst, comparable to that of Ir black, especially since it constitutes more than half of the total Ir loading for the 40 and 65 wt.% loaded catalysts. The remaining

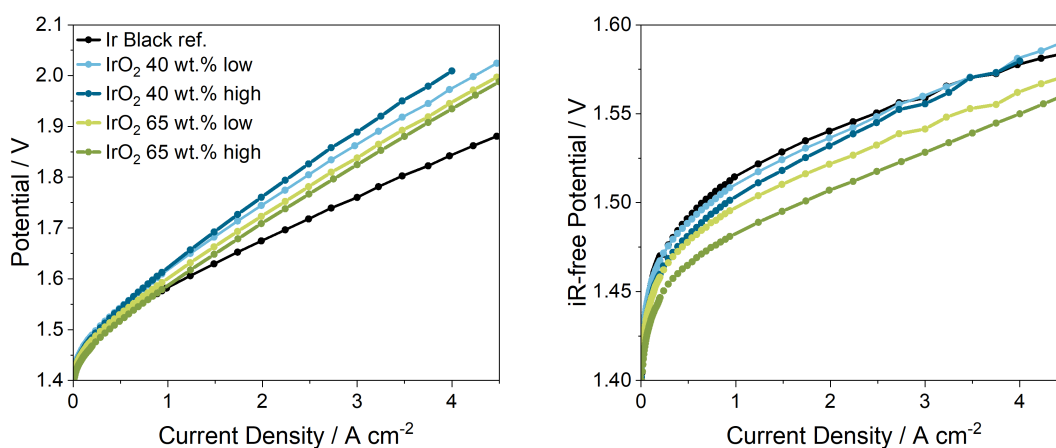


Figure 6.3.4: Performance of homogeneous IrO_2/ATO CCMs with a Ir black reference CCM in a) uncompensated polarization data and b) compensated iR-free polarization data.

difference at higher current densities is thus due to lower in-plane electrical conductivity, resulting in a higher HFR for the IrO₂/ATO CCMs. It also demonstrates a non-zero contribution of the ATO particles to the overall structure and electrical conduction paths, as the observed in-plane resistance would match that of the Ir black reference CCM if the Ir black dominates the CL's structure. Performance of the lower loaded 40 wt.% CCM is actually higher compared to the higher loaded one, illustrating a non-linear correlation between the overall Ir content and the cells performance. Longer electrical conduction paths and diffusion paths through the thicker layer could increase the CCM's HFR and η_{MT} , causing the higher cell potential.^[95,180] However, this trend is reversed for the 65 wt.% IrO₂/ATO catalyst, where the thicker CCM performs better than the thinner one. It could be assumed, that the in-plane electrical conductivity, due to the higher amount of IrO₂ particles is comparable between the two and that more active sites contribute to the slightly lower potential. This might indicate a much higher probability of electrical conduction through the Ir particles, which results in the higher overall conductivity and performance benefits. Still, even at a very high loading of 2.8 mg_{Ir} cm⁻² for the 65 wt.% IrO₂/ATO CCM, the performance above 1 A cm⁻² is lower than that of Ir black, demonstrating, that the total amount of Ir in a CCM is not proportional or deterministic of the cell potential and other factors, such as CL structure, thickness and electrical conductivity, contribute to a larger degree than the loading.

Compensated cell potential, displayed in Figure 6.3.4.b, underlines the differences between the Ir black reference and IrO₂/ATO CCMs, as the IrO₂ catalysts show a lower potential in almost the entire current density range. Here, increased reaction kinetics on the IrO₂/ATO layer comes into play with both 40 wt.% CCMs performing better than the reference and the higher loaded one showing the lowest potential. This confirms that the difference between the low and high loaded 40 wt.% IrO₂/ATO CCMs, mostly stems from an increased electrical resistance in the thicker layer. As the higher loaded CCM offers a proportionally higher amount of active sites, the performance being higher makes sense. This is also reciprocated in the difference between the 65 wt.% IrO₂/ATO CCMs, where the thicker layer performs much better than the thinner one and also all other tested CCMs. The sum of η_{act} and η_{Ohm} seems to be the dominating factor in these layers as these two overpotential terms are the major differences between the two figures. Also, none of the polarization curves show a change in potential increase at higher current densities, indicating a lack of strongly contributing η_{MT} . In terms of overall Ir loading, even the thinner 40 wt.% IrO₂/ATO CCMs is more efficient compared to the Ir black reference with 0.3 mg_{Ir, total} cm⁻² less loading. It suggests one or a combination of faster reaction kinetics of the IrO₂/ATO catalyst, even overcom-

ing a substantially lower Pt-group metal (PGM) mass compared to the reference, or advantageous interaction between the ATO and Ir black. Beneficial interactions between ATO and Ir have previously discussed and are probably caused by SMSI.^[68,187,188] The equalizing and eventually surmounting compensated potential of the 40 wt.% IrO₂/ATO CCMs suggests additional overpotential terms, resulting in a higher potential at higher current densities, like η_{MT} and η_{Ion} in these CLs. But these seem to be rather low compared to the other contributing factors, as these terms only take effect at fairly high current densities.

The apparent increased reaction kinetics of the IrO₂/ATO catalyst can also be observed in Figure 6.3.5 with Tafel slopes about 10 mV dec⁻¹ lower than comparable catalysts, like Ir black, as seen previously in Figure 6.2.4.^[135,179] These low Tafel

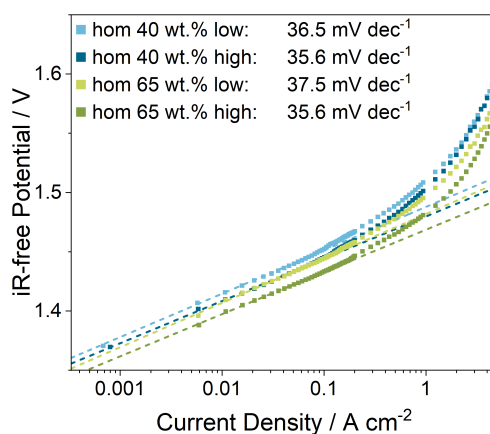


Figure 6.3.5: Kinetic CCM properties calculated by Tafel analysis of differently loaded IrO₂/ATO catalysts at different overall ATO loadings.

slopes along with lower than expected i_0 , suggests an beneficial interaction between not only the IrO₂ on the ATO but also the Ir black and ATO (refer to Table A.7 for Tafel slope and i_0 values). Between the different CCMs, the Tafel slope seems to be rather constant with only i_0 , differentiating the η_{act} . The i_0 here seems to be only correlated with the amount of active sites and decrease with increased overall Ir loading. All differently loaded catalysts thus indicate the same reaction kinetics according to the Tafel slope but overall a more favourable system compared to pure Ir black particles, most likely caused by the ATO support and its interactions with both the IrO₂ and Ir black particles. The semiconductor nature of ATO, was previously discussed to lead to an overall lower oxidation number for the Ir, due to an electron transferring effect, which could increase the OER activity as discussed before.^[88,187] Additionally, the presence of a surface effect of the ATO was argued by Zhang *et al.* in terms of fuel cell catalysts for the oxygen re-

6.3 Catalyst Loading Gradient CCMs

duction reaction (ORR), where O_2 molecules were adsorbing on the ATO surface and migrating to the PGM in a so-called spill-over effect, resulting in higher reaction rates overall.^[188] A similar effect might take place here with O intermediates spilling over to the ATO and causing the apparently higher kinetic properties.

The major contribution to the cell potential is the η_{Ohm} , as the difference between the compensated and uncompensated polarization between IrO_2 /ATO and Ir black CCMs shows. The HFR is quite high compared to the Ir black reference CCM, as depicted in Figure 6.3.6. As discussed in the section before, the HFR of the

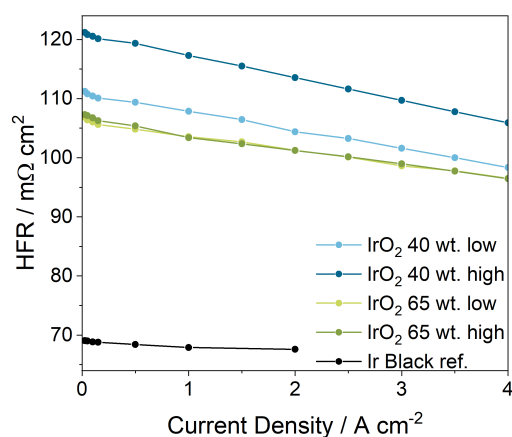


Figure 6.3.6: Dependence of the HFR in comparison to the applied current density for differently loaded IrO_2 /ATO CCMs and Ir black reference CCM.

cell and membrane contribute roughly 72-85 $m\Omega cm^2$, which is in agreement with the Ir black reference but 30-40 $m\Omega cm^2$ lower compared to the IrO_2 /ATO CCMs. Thus, the increased HFR is clearly caused by inter-particle electrical resistance in the ATO. It can also be observed, that the HFR is decreased at higher IrO_2 on ATO loading, causing more likely conduction paths through Ir particles compared to paths through the support material. A higher HFR in the higher overall 40 wt.% loading CCMs with a higher thickness, is also due to the lower electrical conductivity of the support material in the longer conduction paths. Interestingly, the HFR stays constant between the thinner and thicker 65 wt.% IrO_2 /ATO CCM, indicating some kind of threshold being reached, as the HFR is no longer thickness dependent at this loading. This might indicate the formation of a network of IrO_2 particles in some parts of the layer, increasing electrical conductivity but since the HFR is still much higher than the reference CCM, conduction is not fully independent of the ATO as it the electrical resistance would match that of Ir black. Nonetheless, besides the difference in HFR at low current density, an apparent change is visible with the operation conditions, more intense than observed in sections before for

different catalyst materials.

It was previously observed that the HFR could decrease at higher operation current density as local temperatures increase, which increases the membrane's ionic conductivity and in turn decreases the apparent HFR.^[176,180] This effect might also be present here and would explain part of the HFR behavior. It is also well evident in the Ir black reference CCM. As the heating of the measurement cell is only provided through temperature control of the supplied water, the temperature distribution might not be isothermal in the cell, resulting in this rather large decrease of HFR observed. The membrane could thus be at a lower temperature compared to the 80 °C of the supplied water in non-operation state, through heat losses of the current collectors but gets heated with the reaction directly at the membrane. Nevertheless, the effect is even more exacerbated for the IrO₂/ATO CCMs, hinting at more phenomena at play. A key difference between the CCM composition is the ATO support material, which could play a vital role here. It was previously discussed by Giesbrecht *et al.*, that an increased cell temperature might not only benefit membrane conductivity but could also increase electrical conductivity of the material through thermo-ionic emission.^[135] As this effect is not normally occurring in metals, the ATO n-type semiconductor nature could induce this effect here. This is not only dependent on the temperature of the material but also the applied potential between a semiconductor and metal interface. These materials, could form a semiconductor-metal junction, resulting in band positions, that alter the electronic effects of both.^[188,189] Such a junction effect was already presumed to play a role in the reaction kinetic advantages of ATO through SMSI. However, under an applied voltage or reverse bias condition, the conduction band of the semiconductor is bent below the level of the metal and the Schottky barrier, hindering electron transfer across the junction, gets reduced.^[189] The lower Schottky barrier could alleviate electron transfer and lead to an observed benefit in electronic conductivity between ATO and Ir particles. As this effect is dependent on the magnitude of the applied potential, a local increased current density-induced potential increase could intensify this and result in the decreased HFR observed here. A higher electron density in the Ir, as the OER produces electrons in the catalyst, would then allow for more electron transport in to the ATO. Even if the conduction band bending of the semiconductor-metal junction might not reduce the conduction band level of the ATO below that of the Ir, the Schottky barrier is still lowered without reversal of the electron transfer direction, as this would result in a reversal of the SMSI effect, discussed before. Further hints at the influence of the junction effect are found in the smaller decrease HFR of the higher loaded IrO₂/ATO 65 wt.%. As the ATO is covered with more IrO₂ par-

6.3 Catalyst Loading Gradient CCMs

ticles, which are in contact with each other and the Ir black particles, the electrical conduction paths are more likely to flow through the low resistance metal particles without contribution of the ATO, thus decreasing the importance of ATO-Ir junction interfaces. A detailed investigation of this effect is beyond the scope of this thesis and no conclusive evidence can be presented; however, it still remains probable and could spark further research efforts in this phenomenon.

As a measure of the ECSA for oxide-based Ir catalysts, the charge of the redox transition above 0.4 V vs. RHE can be used and is depicted in the whole CV in Figure 6.3.7.a. It is apparent, that this measure increases with overall Ir

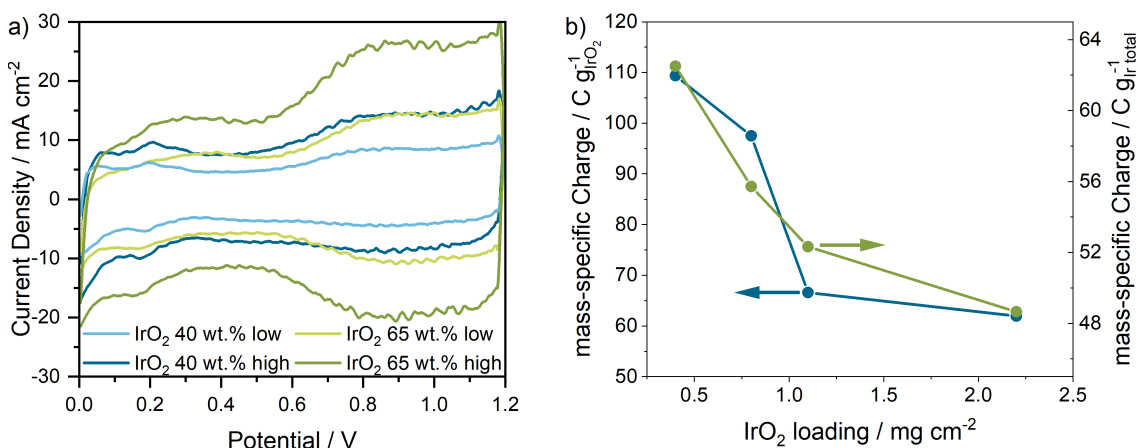


Figure 6.3.7: Depictions of a) CVs for different IrO₂ loadings on ATO in a thinner and thicker CL and b) dependence of the charge attributed to oxidic Ir redox processes (integration of the capacitance-corrected CV above 0.4 V vs. RHE) in relation to the IrO₂ content and total Ir content in the CL.

loading as one would expect and the area is almost the same between the high loading 40 wt.% and low loading 65 wt.% CCM, which both show a Ir loading of 1.4 mg_{Ir, total} cm⁻², as shown in Table 6.3.1. Interestingly, the 40 wt.% catalysts show a more pronounced H_{upd} redox peak below 0.4 V vs. RHE, compared to the 65 wt.% one. As this CV was recorded after the initial conditioning period, meaning some of the Ir black is already oxidized, this difference could indicate a stronger oxidation-inhibiting effect in the lower loaded catalyst. As the Ir black to overall Ir ratio is lower here than in the 65 wt.% IrO₂ loaded catalyst, the support could be at its capacity for electron withdrawing SMSI. The contribution of the Ir black portion in relation to the total IrO charge can also be observed in Figure 6.3.7.b on the right axis. Here the difference between the contribution of each individual Ir species, namely IrO₂ and metallic Ir, are examined to better understand each ones contribution. As seen in the CVs, the difference in charge density in relation to total Ir is almost the same between the two CCMs with the same total

Ir loading. This difference is however much more pronounced, when only considering the IrO₂ portion as a clear drop in IrO₂-based mass-specific charge density can be observed between the 40 and 65 wt.% CCMs with the same total Ir content. This indicates a better catalyst utilization in the lower loaded catalyst, as the obtained charge per invested IrO₂ is higher. At a higher IrO₂ loading, the individual particles might not be fully distributed across the support material, resulting in touching surfaces, which are not accessible as reaction sites. Even though the total amount of active sites seems to be higher in the 65 wt.% IrO₂ catalyst, as observed before, its utilization is lower based on the determined charge density, due to less electrolyte exposed surfaces. The general trend is visible in both mass-specific charge densities, as a higher loading leads to lower utilization and thus lower charge, with caveats for each individual CCM as the composition changes between IrO₂ and Ir black.

The separation of the processes within the electrode into individual contributions can be achieved by deconvolution of EIS data by DRT analysis.^[135] Each different process takes place on different temporal scales and according to the perturbation frequency at which this process can be detected in EIS, its associated resistance value can be calculated. The change of DRT signals with varying current density in the kinetic potential range is depicted for one CCM in Figure 6.3.8. The

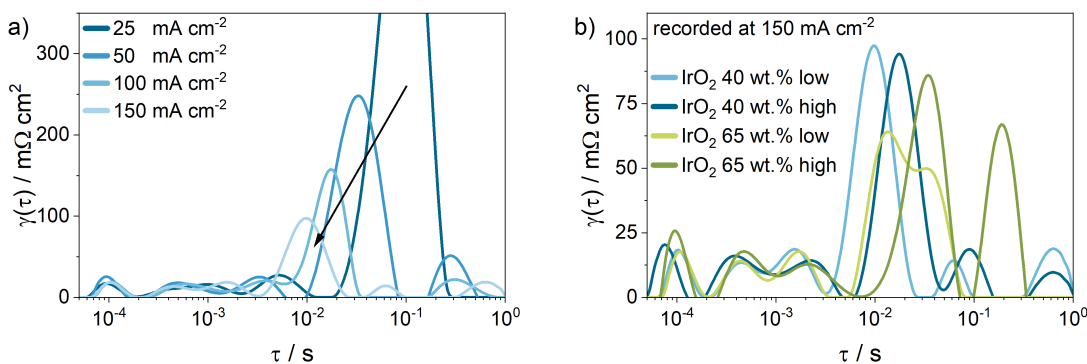


Figure 6.3.8: DRT analysis of a) the homogeneous 40 wt.% IrO₂/ATO low total loading CCM at different current densities with the arrow indicating major shifts in operation change and b) all homogeneous CCMs at 150 mA cm⁻².

most prominent signal occurs around 10⁻² to 10⁻¹ s and is associated with anodic charge transfer processes, according to an in-depth analysis by Giesbrecht *et al.*^[135] As the current density increases, this peak decreases in magnitude, indicating a smaller resistance values associated with it and also shifts to smaller τ value. This behavior of charge transfer processes is well established, as the reaction rate is driven by higher current densities and the individual reactions accelerate.^[135,136] Other signals, especially at lower τ values, stay approximately

constant with the increasing current density, with the exception of new signals appearing at 5×10^{-1} s, that seem to stem from a portioning of the large charge transfer signal after increasing the current density to 50 mA cm^{-2} . The signal at high τ values is frequently associated with mass transport processes, in particular water transport. However, the reliability of EIS data at low current densities is uncertain at low frequencies (high τ values), as shown in the Nyquist-plots of these CCMs in Figure A.1. The evolution of these signals with increasing current density to lower resistance values and higher τ values is however consistent with the observations by Giesbrecht *et al.*^[135] This might be a hint of electroosmotic drag, transporting water according to the potential gradient of the cell and becoming visible even at these low current densities.

When comparing different CCMs, at the same current density, contributions of the CCM composition and morphology become apparent, as depicted in Figure 6.3.8.b. Both the magnitude and position of the anodic charge transfer signal is dependent on the overall Ir loading of the CCM. With increasing total Ir loading, the charge transfer signal shifts to larger τ values, as the ECSA or rather charge associated with the oxidic Ir redox processes, increases, as discussed before. This is caused by the higher capacitance of these catalysts and shifts the signal to larger τ values as the charging of the larger capacitance takes longer.^[135] However, the magnitude of the signal decreases, suggesting a lower resistance associated with the η_{act} , which is consistent with observations discussed before in terms of Tafel slope and i_0 values. The signal shape of the 65 wt.% low loading IrO₂/ATO CCM is different from the others and might be explained by additional processes taking place at close τ values, however this effect is not observable in any other DRT spectrum and could thus be due to uncertainty in the analysis. Nevertheless, the signal position and combined magnitude of both individual signals are consistent with the correlations made before. Signals at high τ values do not follow a clear trend in terms of CCM composition and might thus be caused by unreliable EIS data at these frequencies. Two smaller signals around 6×10^{-3} and 2×10^{-3} s are usually associated with anodic ionic transport processes in addition to cathode operation.^[135] Even though the differences are small, it can be observed that the signal at the lower τ is higher in magnitude for the thicker CCMs, which is consistent with the observed ionic resistivity of the CCMs, as the diffusion paths in the thicker layer are longer, resulting in a R_{ion}^{CL} . The signal at the larger τ value of the two is also correlated with anodic ionic transport but also charge transfer processes.^[135] As before, the higher relative ECSA leads to a shift to higher τ values, which is in accordance to the behavior of this signal in the thicker CCMs compared to the thinner ones. Differences in observed processes are of special interest in

the thicker CCMs, as the gradient layers are composed in the same way and their behavior with increasing current density might yield additional insights when comparing gradient CL. The change in DRT spectra is displayed at 0.5 and 1.0 A cm⁻² in Figure 6.3.9. Magnitude and τ of the charge transfer signal decreases further

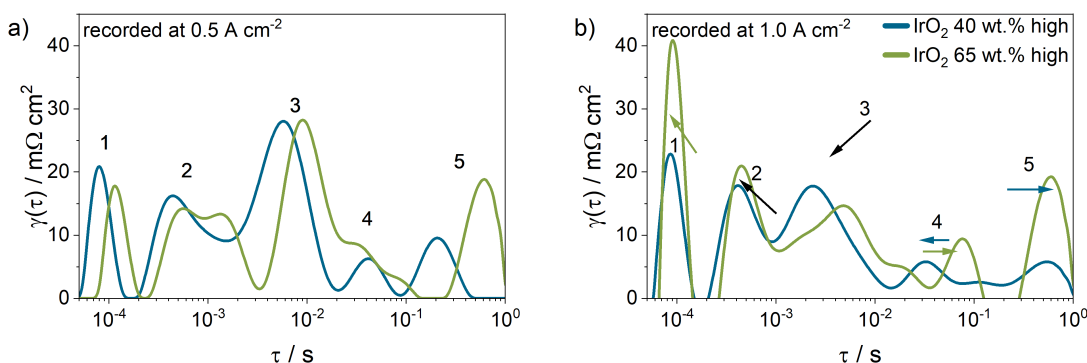


Figure 6.3.9: DRT analysis of a) the homogeneous 40 and 65 wt.% IrO₂/ATO high total loading CCMs at 0.5 A cm⁻² and b) the homogeneous 40 and 65 wt.% IrO₂/ATO high total loading CCMs at 1.0 A cm⁻² with the coloured arrows indicating change in peak position and intensity for either one of the CCMs (blue or green) or both simultaneously (black) from 0.5 to 1.0 A cm⁻².

at 0.5 A cm⁻² and continues at higher current densities. This trend is also observable at very high current densities up to 4.0 A cm⁻², depicted in Figure A.2. As the charge transfer signal shifts to lower τ , the anodic ionic transport signals merge to only one visible, while the one at higher τ merges with the larger charge transfer signal. With increasing current density the signal 2 increases in magnitude, which suggests an increase in ionic transport resistance. While the signal stays constant for the 40 wt.% catalyst, the higher loaded one increases, which can be caused by the higher reaction rate due to increased total Ir loading. With a higher reaction rate the transport of H⁺ could become more limiting as the ionomer film should be identical between the two CCMs. It becomes even more apparent at even higher current densities, where this trend continues. At high τ , the signal of the 65 wt.% IrO₂/ATO catalyst stays constant, while the signal for the lower loaded layer shifts to larger τ and gains in magnitude. It could indicate a limitation in mass transport, that is constant at a certain value for the higher loaded catalyst, due to the higher reaction rate but only becomes evident for the lower loaded one with increasing current density. While these two signals are still distinct at 1 A cm⁻², they are of equal position and magnitude above 2 A cm⁻². As this signal remains constant even up to high current densities, no strongly limiting factor of mass transport is attributed to these CCMs as this would increase to much larger resistance values at 4 A cm⁻². The impact of these individual effects is fairly well differentiated be-

tween different CCM compositions, signifying a profound impact of the IrO₂/ATO loading on these phenomena.

Overall, the performance of these supported-catalysts is very promising, considering sufficient in-plane conductivity with increased reaction kinetics and supposedly beneficial interactions between the support material the deposited IrO₂ as well as the Ir black. Further improvements in the intrinsic electrical conductivity of the ATO could easily overcome the performance detriments and results in a generally higher-performing catalyst compared to Ir black and subsequently also unsupported IrO₂ catalysts. Of special importance are the very low Tafel slope and i_0 , observed here as they are both lower compared to literature results for other IrO₂ or metallic Ir catalysts and can be reliably observed across multiple different CCMs.^[12,41,93,180]

6.3.3 Gradient Ir Loading CCMs

A gradient design based on the catalyst loading along the CL thickness can be promising in combining different aspects of the varying individual loadings to yield a superior CL overall, that performs better than just the average of both homogeneous layers would suggest. The homogenization of the reaction rate is a impactful factor here, where it might improve mass transport effects and affect the electric conductivity of to whole layer, as the reaction can take place in different parts of the CL depending on the conductivity of the catalyst. Polarization data of two gradient layers with 40 and 65 wt.% IrO₂/ATO sublayers in both coating directions is displayed in Figure 6.3.10.a along with the comparison to homogeneous CCMs with the same ATO and Ir black content as the gradient ones. Cell potentials of both gradient layers is between both homogeneous ones with the caveat of a lower total potential than the average of both homogeneous ones. The expected difference is mainly due to the total Ir loading, which is with 2.1 mg_{Ir} cm⁻² right in the middle between the 1.4 and 2.8 mg_{Ir} cm⁻², of the homogeneous ones. Both gradient ones show a fairly comparable performance with the 40|65 wt.% CCM performing slightly better at higher current densities. A higher than average performance of these CLs suggests an additional effect caused by the gradient design, independent on the total Ir loading. The difference between the gradient CCMs becomes more apparent in the iR-free polarization data, displayed in Figure 6.3.10.b, where the 40|65 wt.% CCM shows an even more improved performance compared to the other gradient one. In fact, this CL matches the performance of the higher loaded homogeneous CCM at high current densities. This suggests a small benefit of a higher loaded sublayer at the PTL and a lower loaded one at

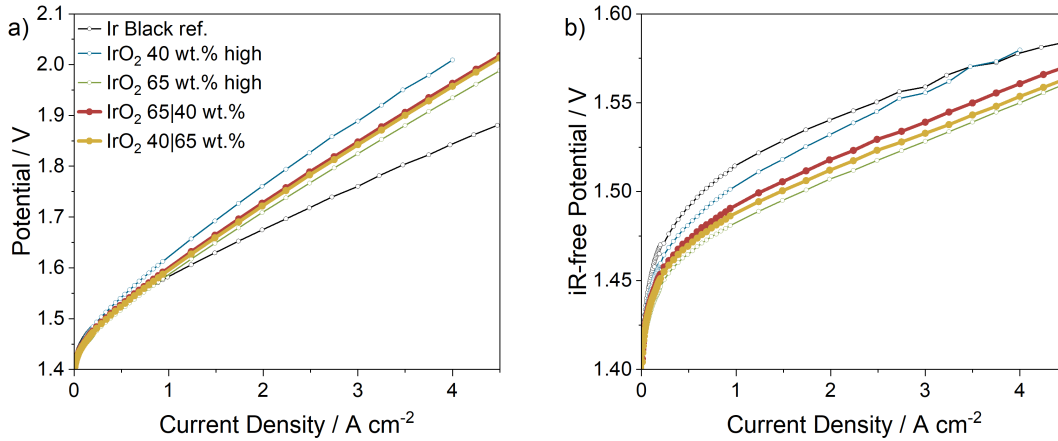


Figure 6.3.10: Performance of gradient and homogeneous IrO_2/ATO CCMs with a Ir black reference CCM in a) uncompensated polarization data and b) compensated iR-free polarization data.

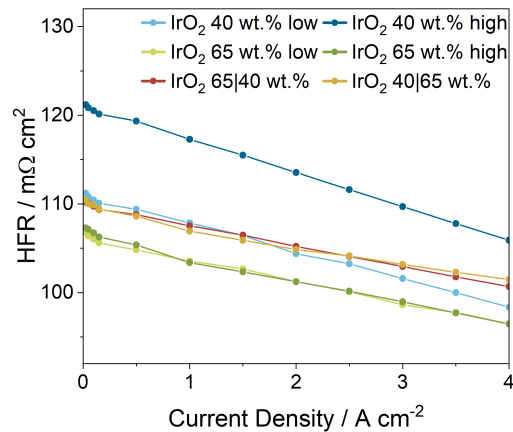


Figure 6.3.11: Dependence of the HFR in comparison to the applied current density for gradient and homogeneous IrO_2/ATO CCMs.

the membrane, resulting in a more efficient CCM compared to the homogeneous one. Both gradient layers show almost no difference in HFR, as shown in Figure 6.3.11, where both show an HFR comparable to the homogeneous low overall loading 40 wt.% CCM at low current densities and slightly higher at high ones. The HFR experienced by the whole CCM is thus not dependent on the setup or the position of individual sublayers with different electronic conductivities. It is only dependent on the total value of the least conductive sublayer. One could argue that the conductivity of the sublayer near PTL being the determining one as all electrical current flows through this but it is clearly not the case as evidenced here. The current density dependence of the HFR does differ from the homogeneous thin 40 wt.% CCM but it shows the average value between the slope of the

6.3 Catalyst Loading Gradient CCMs

40 and 65 wt.% CCMs indicating an equal contribution of each sublayer to the total electrical conductivity along with its dependence on the cells potential and temperature. As the HFR of both gradients is approximately equal, the performance benefit of the lower loaded sublayer near the membrane becomes even more apparent as seen in the compensated polarization data. This shows a clear benefit of the gradient design in contrast to the average total Ir loading as both the compensated and uncompensated cell potential is lower than the average of the homogeneous ones while the HFR is higher, which compounds the performance advantages. It is also evident in the kinetic parameters as both gradient CCMs show the lowest Tafel values and i_0 among all tested CCMs (see Table A.7). Even though the Tafel slope differences are only about 1.0 to 1.5 mV dec⁻¹, its effect is nevertheless visible in the polarization data, indicating an optimal setup in the gradient design.

Considering, the kinetic parameters are dependent on the catalytic sites, an ECSA and q^* analysis was carried out with the results presented in Figure 6.3.12. CVs

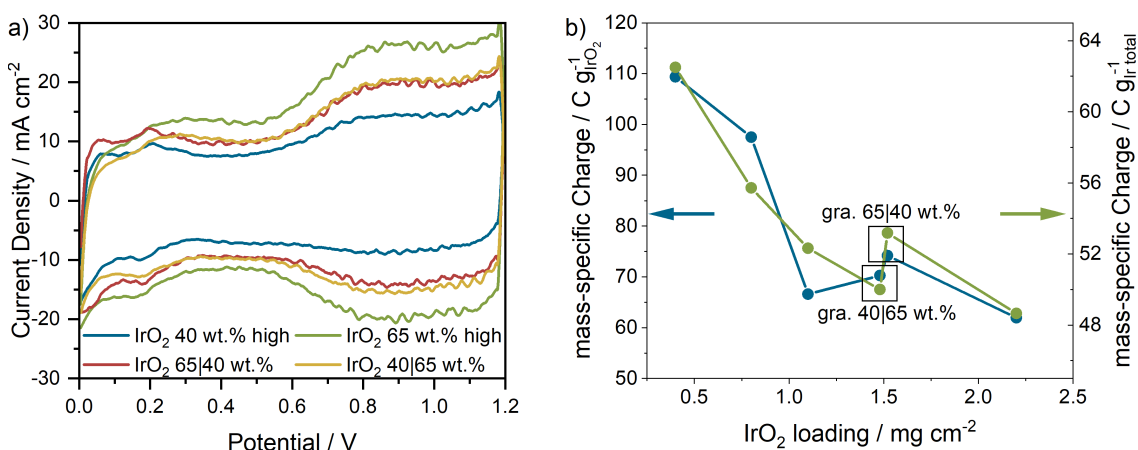


Figure 6.3.12: Depictions of a) CVs for gradient and homogeneous IrO₂/ATO CCMs and b) dependence of the charge attributed to IrO redox processes in relation to the IrO₂ content and total Ir content in the CL.

suggests an averaged charge area of oxidic Ir between the two homogeneous CCM and barely any difference between the two gradient layers. As the charge area is mainly dependent on the total Ir loading this comes as no surprise. However, considering the mass-specific charge area, both gradient layers deviate from a linear correlation with the 65|40 wt.% setup showing higher charges for total Ir and IrO₂-based densities. This in contrast to the higher performance of the other gradient layer and does not seem to be impactful in the kinetic performance as both layers show equal kinetic parameters.

Specific differences in the contribution of processes to the overall performance of a CCM is assessed through the DRT analysis and comparison of individual signals, as shown in Figure 6.3.13. The behavior of the gradient layers is approximately

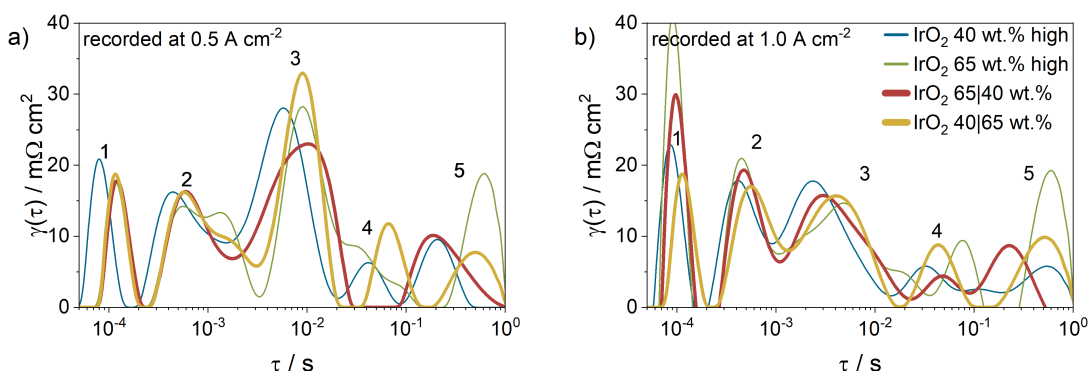


Figure 6.3.13: DRT analysis of a) gradient and homogeneous IrO₂/ATO CCMs at 0.5 A cm⁻² and b) gradient and homogeneous IrO₂/ATO CCMs at 1.0 A cm⁻².

equal in the signal below 10⁻² s and differ slightly at signal 3, which corresponds to anodic charge transfer processes.^[135] Both signals are shifted to higher τ values, comparable to that of the homogeneous 65 wt.% CCM, which correlates with the observations in polarization where the gradient layers are closer to 65 wt.% compared to 40 wt.% performance. However, the 40|65 wt.% gradient CCM shows a higher magnitude of the signal compared to the homogeneous one, which does not fit with the observed kinetic parameters. As the homogeneous CCM shows a shoulder at higher τ values, it could be assumed, that this signal is shifted towards signal 4, diminishing the magnitude of signal 3, which is better separated from signal 4 in the 40|65 wt.% CCM. This convolution of signals can also be the reason for the relatively low magnitude of signal 3 for the 65|40 wt.% CL. Upon increased current density the signal 3 for both gradient CCMs become equal in magnitude, further indicating the difference at 0.5 A cm⁻² stemming from signal overlapping. It also becomes apparent, that signal 5, usually attributed to mass transport and especially water transport effects, show the same τ value for the 65|40 wt.% CCM as the homogeneous 40 wt.% one.^[135] One could assume, this effects stems from the positioning of the sublayers within the overall CL, as the position of signal 5 correlates with the 65 wt.% layer being present at the PTL. This indicates a different distribution of mass transport phenomena, probably due to the distribution of reaction rate within the CL, relative to the PTL. A higher Ir content near the PTL could induce this larger τ as more water reacts in the upper layer of the CL, limiting water transport to near-membrane portions of the CL. With increasing current density this shift in τ diminishes, which could be caused by increasing electroosmotic drag, transporting more water through the cell to

the cathode and thus increasing the water transport rate. Interestingly, the signal 2, usually attributed to ionic transport, is comparable at low current densities but shifts to higher magnitudes for the gradient 40|65 wt.% and homogeneous 65 wt.% CLs, while the other two remain constant even up to 4 A cm^{-2} .^[135] As the higher Ir loading is associated with a higher reaction rate, the ionic transport from the PTL-side 65 wt.% sublayer can induce a higher ionic transport resistance as the transport paths are longer than for the reverse order gradient CCM, where the higher reaction rate is located at the Ir particles directly at the membrane. The difference in path-lengths of conduction processes could thus explain the slight difference in performance between the two gradient CCMs. As R_{ion}^{CL} and the observed DRT signal 2 is lower for the CCM with the higher loaded sublayer near the membrane, the overall performance is higher for the other gradient layer (see Table A.7).

One of the main performance factors is the local η_{Ohm} , as Moore *et al.* discussed, which depends on the in-plane conductivity of the catalyst material.^[95] With a higher loaded and better electrically conductive layer near the PTL, the 40|65 wt.% gradient CCM reduces local η_{Ohm} near the PTL, where the highest reaction rate is induced due to the conductivity terms. Thus the overall performance is slightly higher even though the total HFR observed for the whole CL is similar between both layers.

7 Conclusions and Summary

In this thesis, the concept of a gradient CL design for low-temperature PEMWE anode CLs was explored. The coated gradient layers were investigated alongside their homogeneous counterparts to evaluate the specific properties of the CL and the gradient's impact on them. Gradient CLs, based on differential loading along the layer's thickness, were found to require a supported catalyst. Without the supported catalyst, the gradient would merely vary the layer's thickness without producing the desired effects of keeping most CL properties constant, while varying the Ir loading. Thus, the synthesis of a supported Ir catalyst has been studied to yield a suitable catalyst for a gradient design with variable Ir loading on the substrate.

Four different methods were chosen and appraised for their ability to produce reliable Ir catalysts with a specific Ir content and proportionality of electrochemical performance to the loading. The selected methods produced catalysts with different Ir species, namely metallic Ir or suboxide IrO_x and rutile-type IrO_2 , which demonstrated varied electrochemical performance and stability. To improve comparability, the metallic Ir or IrO_x -based catalysts underwent a heat treatment that converted the bulk of the active species to rutile- IrO_2 . Upon evaluating the individual catalysts, it was found that the RS uncalcined catalyst displayed the highest electrochemical performance with a very reproducible and specific Ir loading. This catalyst primarily consisted of metallic Ir, resulting in high activity but reduced stability, as observed in stability tests where it displayed a lower S-number than its calcined counterpart. When calcined, the catalyst lost a significant amount of activity, but demonstrated a higher S-number due to its improved stability against Ir dissolution, through facilitation of the adsorbate evolution mechanism. The CD and HTD synthesis methods demonstrated lower reproducibility and more importantly, reduced loading specificity, as these catalysts showed loadings of 15 and 25 wt.% Ir, respectively, compared to the desired 40 wt.% loading. This, coupled with multi-step syntheses involving large volumes of solvents, resulted in less desirable methods, especially since the electrochemical activity was lower than that of the other catalysts. The MAF catalyst, consisting primarily of rutile- IrO_2 right after synthesis, emerged as the second interesting catalyst. It was discovered that this catalyst contained a comparatively high amount of Ir^{III} , which is theorized to enhance its performance above the other heat-treated catalysts. Its stability was relatively high but did not match those catalysts containing heat-treated IrO_2 , resulting in a slightly lower S-number, due to its still higher activity towards the OER.

The feasibility of using these synthesis techniques in both a laboratory setting and on an industrial scale was assessed, with the MAF catalyst emerging as the most promising due to its simple salt-melt-based method already in use in large-scale processes. This catalyst also demonstrated good reproducibility and specificity in its Ir loading and was consequently selected for use in further studies of Ir loading gradient CCMs.

The incorporation of a gradient design can be accomplished not only through the variation of Ir loading, but also by adjusting the distribution of ionomer along the CL's thickness. This approach was implemented by coating CCMs with a constant loading of an Ir black catalyst and a varied ionomer loading of 5, 10, 20, and 30 wt.% for homogeneous reference layers. In addition, two gradient layers were created, one with a 10 wt.% ionomer sublayer at the membrane and a 30 wt.% sublayer near the PTL and another in the reverse order, resulting in 30|10 wt.% contents. It was found that the electrochemical performance was optimal at a homogeneous 20 wt.% ionomer content among the other evaluated homogeneous ionomer loadings, contrary to other studies that identified a 10 wt.% optimum loading. For this lower loading layer, a higher HFR was determined, resulting in lower performance compared to 20 wt.%. At 30 wt.% ionomer, an even higher HFR was observed with minimal current density dependence, whereas the other CCMs exhibited a stronger HFR decrease with increasing current density. This was attributed to water starvation in the lower parts of the CL, in part due to the near-zero void pore volume at this high ionomer loading. Some of this effect also led to a higher R_{ion}^{CL} compared to lower ionomer loadings, which would typically decrease with increasing ionomer content. This was likely due to ionomer compression within the pores following water-induced swelling and subsequent water discharge, reducing the protonic conductivity of the CL. Given that the optimum ionomer loading in homogeneous CCMs was found to be 20 wt.%, the gradient layers can be compared and referenced by their average loading of 20 wt.%, emphasizing any differences resulting from the gradient design. Normally, a higher ionomer content near the membrane would increase ionic conductivity and consequently enhance performance as the local η_{ion} is reduced where the reaction rate is highest. However, this effect was not observed in the 30|10 wt.% CCM. Instead, a reversed effect occurred, where this CL led to lower performance compared to the homogeneous 10 and 20 wt.% loadings. Contrarily, the 10|30 wt.% loading CCM displayed the best performance among all measurements. This was attributed to a relatively low HFR, comparable with the 20 wt.% CL and significantly lower than the other gradient CCM. Furthermore, the exchange current density was slightly lower with an average Tafel slope, resulting in better performance at

lower current densities. The detrimental effects of a 30 wt.% ionomer loading were not observed in either gradient CCM, likely due to sufficient accessible void pore volume in the adjacent sublayer. In summary, the gradient design of ionomer had a mixed impact on the performance of the CCM, but it can be beneficial if applied carefully on previously optimized ionomer contents for each specific catalyst. Particularly at relatively high ionomer contents, a gradient design can alleviate some of the negative effects of the higher loading.

The third part of this thesis examined the gradient design based on different Ir loadings along the thickness of the CL. The first step towards optimizing the CL composition involved fine-tuning the ionomer content, which was determined to be approximately 10 wt.% Nafion[®] based on a CCM containing the 40 wt.% IrO₂/ATO catalyst. However, applying pure IrO₂/ATO CLs led to high HFR values and low performance, which was attributed to the low in-plane electrical conductivity of the support material. To mitigate this issue, a fixed amount of Ir black was added, significantly enhancing the performance of the CCMs. Using these optimized layers, various effects were observed. Compensated polarization data for the 65 wt.% IrO₂/ATO catalysts showed substantially lower potentials compared to the Ir black reference. Interestingly, even at lower total Ir loading, the CCMs based on IrO₂/ATO performed better than the reference. This superior performance was partially attributed to rapid kinetics, leading to a substantially lower Tafel slope and exchange current density values than expected. The ATO is likely the cause of these performance benefits, as the probable effect of a semiconductor-metal junction was observed. This not only influences the catalyst's reaction kinetics but also improves the electrical conductivity with increasing operation current density, surpassing the expected behavior due to increased local temperatures observed in Ir black. Despite its low intrinsic electrical conductivity, this catalyst and its support material individually represent a promising novel composite. It not only shows high performance in an aqueous model system in the RDE characterizations but also on a full electrolyzer cell level. With suitable modifications to improve the ATO's electrical conductivity, such as different dopants, or through the addition of a component with very high electrical conductivity to the CL (such as Ir black in this project), CCMs with exceptional properties could be produced. The performance-enhancing effects observed in the homogeneous CCMs were also found in the gradient ones, with most parameters exhibiting an average between the two homogeneous layers that constitute the gradient layers. The HFR was determined to be dependent only on the least electrically conductive sublayer, as both gradient CCMs showed equal values, independent of the sublayer position. Despite the identical total HFR, it was assumed that a slight performance difference between

both gradient layers was caused by variations in local electrical conductivity. The CCM with the higher electrically conductive sublayer near the PTL showed a lower cell potential. Given that the position of the reaction rate maximum is dependent on the catalyst's electrical conductivity, the position of the higher-loaded sublayer near the PTL was deemed optimal. This resulted in a performance enhancement of the gradient layers relative to the homogeneous ones that surpassed what the average total Ir loading would suggest. Additionally, a minor contributing factor of the sublayer position to R_{ion}^{CL} was identified, where the higher-loaded sublayer near the membrane was found to decrease R_{ion}^{CL} , suggesting a correlation between ionic transport paths through the CL and R_{ion}^{CL} . The improved performance of the loading gradient CCMs, with one displaying even lower cell potentials, makes this design an intriguing choice for increased efficiency in anodic CLs, thus achieving higher Ir utilization. A clear performance-enhancing effect stronger than that induced solely by total Ir loading was observed, which depends on the location of individual sublayers, resulting in more efficient CLs than their individual constituents.

Overall, the gradient design was found to enhance the electrolyzer cell performance in two independent ways: both the ionomer gradient and the Ir loading gradient showed increased efficiency relative to their homogeneous counterparts. Individual contributions of the gradient design strongly depend on careful consideration of CL composition but show potential for ways to lower the Ir content in anodic electrolyzer CLs.

8 Outlook

In the evaluation of catalyst and support materials, as well as their assembled CLs, several novel effects were observed and challenges encountered in material characterization due to some inherent limitations of those materials. Further efforts are necessary to optimize the materials and identify new strategies for mitigating the disadvantages. A primary concern is the low electrical conductivity of the ATO support. Hence, synthesis methods that can enhance its conductivity, such as different dopants or dopant concentrations or modified crystal structures, could be extremely beneficial. This material demonstrated significant potential, particularly in enhancing the kinetic activity of Ir in both RDE and MEA setups. Introducing novel support materials, offering higher conductivity, could also be advantageous when combined with the demonstrated synthesis methods. However, it is important to note that some effects that promote reactions might be due to the semiconductor nature of ATO and may not be present in other material classes.^[73,76,77,79] These effects could also provide further insights through in-depth calculations and characterization into the nature of the SMSI. This knowledge could prove substantially beneficial for future support materials. The band structure of the support-metal interface is of particular interest, as it might not only enhance catalytic activity, but also affect the electrical conductivity of the CL under reverse bias conditions. In addition to the exploration of novel support materials, the structure of Ir species could be further refined to yield more stable and active catalysts. Recently, it was described how the interaction between rutile-IrO₂ and IrO_x impacts the catalyst properties, as a design based on a thin surface layer of fully oxidized rutile-IrO₂ and lower IrO_x layers could improve its stability while maintaining the reaction participation of lower layers, resulting in a higher volumetric ECSA.^[170] As the overall PGM loading in PEM electrolysis needs to be reduced for widespread application, the concept of supported catalysts, akin to Pt on C catalysts in fuel cells, may be inevitable. The reduction of Ir can only be continued up to a certain point, when the CL becomes too thin and inhomogeneous below 5 μm.^[93,180] In the grand scheme of things, the development of relatively active non-PGM catalysts would significantly propel the technology. The total supply of PGMs remains a concern for the widespread application of PEM electrolysis as a cornerstone of energy transition technology and more research into Ir alternatives could prove unavoidable.

As extensively demonstrated in this thesis, the concept of an ionomer and PGM loading gradient along the thickness of the CL emerges as a promising concept

that could be expanded to include multiple gradients concurrently. The simultaneous application of ionomer and Ir loading gradients can further optimize individual components of the CCM and enhance material investment efficiency. However, careful consideration must be given to the nature of the catalyst and the homogeneous CL properties targeted for use in gradient designs. Beyond grading the ionomer and catalyst material, the implementation of a hierarchical catalyst structure or pore network could be a promising application of this concept. This could be achieved by varying coating parameters, such as the temperature and suspension composition, to allow the CL to form varying degrees of pore volume. Another approach would be to use structured materials that have a defined pore network, like mesoporous TiO_2 or ATO, with different structural properties in sequential layers. This could substantially enhance mass transport phenomena, especially under certain operation conditions, such as water starvation in lower CL portions at high operating currents.^[94,190,191] With the introduction of novel materials that address some shortcomings of the current gradients presented here, their performance impact could be even more significant. For example, a microporous layer for PTLs could establish lower contact resistance at the CL-PTL interface, leading to a reduced requirement for catalyst in-plane conductivity at that interface.^[95] Individual contributions of the gradient design that affect performance should also be evaluated in tandem with modelling systems. These systems can further assess its impact and guide future efforts to produce more efficient gradients by addressing specific local overpotential terms within the CL. This, coupled with more sophisticated analysis hardware, could further enhance this promising approach. For instance, performance analysis based on elevated operation pressures and segmented cell hardware could help localize certain effects.^[21,41] Advanced imaging technology, such as nano-computed tomography might also elucidate the catalyst micro structure to yield valuable insights about the pore network and thus ionic as well as electronic conduction paths inside an intact CL.

Bibliography

- [1] H. P. Jones, D. G. Hole, E. S. Zavaleta, *Nature Clim. Change* **2012**, *2*, 504–509.
- [2] S. I. Zandalinas, F. B. Fritschi, R. Mittler, *Trends Plant Sci.* **2021**, *26*, 588–599.
- [3] OECD, *The Climate Action Monitor 2022: Helping Countries Advance Towards Net Zero*, OECD Publishing, Paris, **2022**.
- [4] German Federal Ministry for the Environment, Nature Conservation, Nuclear Safety and Consumer Protection, Climate Action Plan 2050: Principles and goals of the German government's climate policy, **2016**.
- [5] Deutsche Bundesregierung, Von der Kohle zur Zukunft: Kohleausstieg und Strukturstärkung, **2023**, <https://www.bundesregierung.de/breg-de/schwerpunkte/klimaschutz/kohleausstieg-1664496>.
- [6] L. de La Peña, R. Guo, X. Cao, X. Ni, W. Zhang, *Resour. Conserv. Recycl.* **2022**, *177*, 105957.
- [7] Federal Ministry for Economic Affairs and Energy, The National Hydrogen Strategy, (Ed.: Public Relations Division), **2020**.
- [8] M. Chen, S.-F. Chou, F. Blaabjerg, P. Davari, *Appl. Sci. (Basel)* **2022**, *12*, 1906.
- [9] C. van Pham, D. Escalera–López, K. Mayrhofer, S. Cherevko, S. Thiele, *Adv. Energy Mater.* **2021**, 2101998.
- [10] U. Babic, E. Nilsson, A. Pătru, T. J. Schmidt, L. Gubler, *J. Electrochem. Soc.* **2019**, *166*, F214–F220.
- [11] U. Babic, M. Suermann, F. Büchi, L. Gubler, T. Schmidt, *J. Electrochem. Soc.* **2017**, *164*, F387–F399.
- [12] M. Bernt, H. A. Gasteiger, *J. Electrochem. Soc.* **2016**, *163*, F3179–F3189.
- [13] C. Daiane Ferreira da Silva, F. Claudel, V. Martin, R. Chattot, S. Abbou, K. Kumar, I. Jiménez-Morales, S. Cavaliere, D. Jones, J. Rozière, L. Solà-Hernandez, C. Beauger, M. Faustini, J. Peron, B. Gilles, T. Encinas, L. Piccolo, F. H. Barros de Lima, L. Dubau, F. Maillard, *ACS Catal.* **2021**, *11*, 4107–4116.
- [14] F. C. Cetinbas, S. G. Advani, A. K. Prasad, *J. Power Sources* **2014**, *270*, 594–602.
- [15] M. Santis, S. A. Freunberger, A. Reiner, F. N. Büchi, *Electrochim. Acta* **2006**, *51*, 5383–5393.
- [16] Z. Chang, J. Zhang, W. Zhang, H. Su, L. Xing, Q. Ma, H. Zhang, Q. Xu, *Processes (Basel)* **2021**, *9*, 1787.
- [17] R. de Levie, *J. Electroanal. Chem. (Lausanne)* **1999**, *476*, 92–93.
- [18] L. Vidas, R. Castro, *Appl. Sci. (Basel)* **2021**, 11363.

- [19] A. S. Ansar, A. S. Gago, F. Razmjooei, R. Reißner, Z. Xu, K. A. Friedrich in *Electrochemical Power Sources: Fundamentals, Systems, and Applications*, (Eds.: T. Smolinka, J. Garche), Elsevier, **2022**, pp. 165–198.
- [20] J. Brauns, T. Turek, *Processes (Basel)* **2020**, 248.
- [21] P. Trinke, P. Haug, J. Brauns, B. Bensmann, R. Hanke-Rauschenbach, T. Turek, *J. Electrochem. Soc.* **2018**, *165*, F502–F513.
- [22] S. Shiva-Kumar, V. Himabindu, *Mater. Sci. Energy Technol.* **2019**, *2*, 442–454.
- [23] A. J. Bard, L. R. Faulkner, *Electrochemical Methods: Fundamentals and Applications*, 2nd ed., John Wiley and Sons, New York, **2001**.
- [24] W. Li, H. Tian, L. Ma, Y. Wang, X. Liu, X. Gao, *Mater. Adv.* **2022**, *3*, 5598–5644.
- [25] M. W. Chase, *NIST-JANAF thermochemical tables*, Fourth edition. Washington, DC : American Chemical Society and New York : American Institute of Physics for the National Institute of Standards and Technology, Washington, D.C., **1998**.
- [26] S. A. Grigoriev, V. N. Fateev in *Hydrogen production technologies*, (Eds.: M. Sankir, N. Demirci Sankir), Scrivener Publishing, Beverly, MA and Hoboken, NJ, **2017**, pp. 231–269.
- [27] A. J. Shih, M. C. O. Monteiro, F. Dattila, D. Pavesi, M. Philips, A. H. M. Da Silva, R. E. Vos, K. Ojha, S. Park, O. van der Heijden, G. Marcandalli, A. Goyal, M. Villalba, X. Chen, Gunasooriya, G. T. Kasun Kalhara, I. McCrum, R. Mom, N. López, M. T. M. Koper, *Nat. Rev. Methods Primers* **2022**, *2*, 1–19.
- [28] C. Xiang, K. M. Papadantonakis, N. S. Lewis, *Mater. Horiz.* **2016**, *3*, 169–173.
- [29] A. Hodges, A. L. Hoang, G. Tsekouras, K. Wagner, C.-Y. Lee, G. F. Swiegers, G. G. Wallace, *Nat. Commun.* **2022**, *13*, 1304.
- [30] C. C. L. McCrory, S. Jung, J. C. Peters, T. F. Jaramillo, *J. Am. Chem. Soc.* **2013**, *135*, 16977–16987.
- [31] D. Henkensmeier, M. Najibah, C. Harms, J. Žitka, J. Hnát, K. Bouzek, *J. Electrochem. En. Conv. Stor* **2021**, *18*, 024001–024019.
- [32] T. Adibi, A. Sojoudi, S. C. Saha, *Int. J. Thermofluids* **2022**, *13*, 100126.
- [33] I. Vincent, D. Bessarabov, *Renewable Sustainable Energy Rev.* **2018**, *81*, 1690–1704.
- [34] A. Nechache, S. Hody, *Renewable Sustainable Energy Rev.* **2021**, *149*, 111322.
- [35] M. Riedel, M. P. Heddrich, A. Ansar, Q. Fang, L. Blum, K. A. Friedrich, *J. Power Sources* **2020**, *475*, 228682.
- [36] L. Wehrle, D. Schmider, J. Dailly, A. Banerjee, O. Deutschmann, *Appl. Energy* **2022**, *317*, 119143.

- [37] Y. Tian, N. Abhishek, C. Yang, R. Yang, S. Choi, B. Chi, J. Pu, Y. Ling, J. T. Irvine, G. Kim, *Matter* **2022**, *5*, 482–514.
- [38] Z. Pan, Q. Liu, Z. Yan, Z. Jiao, L. Bi, S. H. Chan, Z. Zhong, *Electrochem. Commun.* **2022**, *137*, 107267.
- [39] G. Bender, M. Carmo, T. Smolinka, A. Gago, N. Danilovic, M. Mueller, F. Ganci, A. Fallisch, P. Lettenmeier, K. A. Friedrich, K. Ayers, B. Pivovar, J. Mergel, D. Stolten, *Int. J. Hydrogen Energy* **2019**, *44*, 9174–9187.
- [40] N. W. DeLuca, Y. A. Elabd, *J. Polym. Sci. B Polym. Phys.* **2006**, *44*, 2201–2225.
- [41] P. Trinke, G. Keeley, M. Carmo, B. Bensmann, R. Hanke-Rauschenbach, *J. Electrochem. Soc.* **2019**, *166*, F465–F471.
- [42] K. C. Neyerlin, W. Gu, J. Jorne, H. A. Gasteiger, *J. Electrochem. Soc.* **2007**, *154*, B631.
- [43] J. Durst, A. Siebel, C. Simon, F. Hasché, J. Herranz, H. A. Gasteiger, *Energy Environ. Sci.* **2014**, *7*, 2255–2260.
- [44] M. Langemann, D. L. Fritz, M. Müller, D. Stolten, *Int. J. Hydrogen Energy* **2015**, *40*, 11385–11391.
- [45] P. Shirvanian, F. van Berkel, *Electrochem. Commun.* **2020**, *114*, 106704.
- [46] M. Breitwieser, M. Klingele, S. Vierrath, R. Zengerle, S. Thiele, *Adv. Energy Mater.* **2018**, *8*, 1701257.
- [47] B. Bensmann, R. Hanke-Rauschenbach, I. K. Peña Arias, K. Sundmacher, *Electrochim. Acta* **2013**, *110*, 570–580.
- [48] M. Carmo, D. L. Fritz, J. Mergel, D. Stolten, *Int. J. Hydrogen Energy* **2013**, *38*, 4901–4934.
- [49] N. Danilovic, R. Subbaraman, K.-C. Chang, S. H. Chang, Y. J. Kang, J. Snyder, A. P. Paulikas, D. Strmcnik, Y.-T. Kim, D. Myers, V. R. Stamenkovic, N. M. Markovic, *J. Phys. Chem. Lett.* **2014**, *5*, 2474–2478.
- [50] L. Moriau, M. Smiljanić, A. Lončar, N. Hodnik, *ChemCatChem* **2022**, e202200586.
- [51] S. Trasatti, *J. Electroanal. Chem. Interfacial Electrochem.* **1980**, *111*, 125–131.
- [52] L. An, C. Wei, M. Lu, H. Liu, Y. Chen, G. G. Scherer, A. C. Fisher, P. Xi, Z. J. Xu, C.-H. Yan, *Adv. Mater.* **2021**, *33*, e2006328.
- [53] S. Trasatti, *Electrochim. Acta* **1984**, *29*, 1503–1512.
- [54] M. H. Miles, M. A. Thomason, *J. Electrochem. Soc.* **1976**, *123*, 1459–1461.
- [55] D. Galizzioli, F. Tantardini, S. Trasatti, *J. Appl. Electrochem.* **1974**, *4*, 57–67.
- [56] S. M. Alia, G. C. Anderson, *J. Electrochem. Soc.* **2019**, *166*, F282–F294.
- [57] D. F. Abbott, R. K. Pittkowski, K. Macounová, R. Nebel, E. Marelli, E. Fabbrì, I. E. Castelli, P. Krtil, T. J. Schmidt, *ACS Appl. Mater. Interfaces* **2019**, *11*, 37748–37760.

- [58] J. Zhang, X. Fu, F. Xia, W. Zhang, D. Ma, Y. Zhou, H. Peng, J. Wu, X. Gong, D. Wang, Q. Yue, *Small* **2022**, *18*, e2108031.
- [59] Y.-T. Kim, P. P. Lopes, S.-A. Park, A.-Y. Lee, J. Lim, H. Lee, S. Back, Y. Jung, N. Danilovic, V. Stamenkovic, J. Erlebacher, J. Snyder, N. M. Markovic, *Nat. Commun.* **2017**, *8*, 1449.
- [60] M. Zlatar, D. Nater, D. Escalera-López, R. M. Joy, P. Pobedinskas, K. Haenen, C. Copéret, S. Cherevko, *Electrochim. Acta* **2023**, *444*, 141982.
- [61] X.-K. Gu, J. C. A. Camayang, S. Samira, E. Nikolla, *J. Catal.* **2020**, *388*, 130–140.
- [62] W.-H. Lai, L.-F. Zhang, W.-B. Hua, S. Indris, Z.-C. Yan, Z. Hu, B. Zhang, Y. Liu, L. Wang, M. Liu, R. Liu, Y.-X. Wang, J.-Z. Wang, Z. Hu, H.-K. Liu, S.-L. Chou, S.-X. Dou, *Angew. Chem. Int. Ed.* **2019**, *58*, 11868–11873.
- [63] M. Xiao, J. Zhu, G. Li, N. Li, S. Li, Z. P. Cano, L. Ma, P. Cui, P. Xu, G. Jiang, H. Jin, S. Wang, T. Wu, J. Lu, A. Yu, D. Su, Z. Chen, *Angew. Chem. Int. Ed.* **2019**, *58*, 9640–9645.
- [64] Q. Feng, X.-Z. Yuan, G. Liu, B. Wei, Z. Zhang, H. Li, H. Wang, *J. Power Sources* **2017**, *366*, 33–55.
- [65] M. Carmo, G. P. Keeley, D. Holtz, T. Grube, M. Robinius, M. Müller, D. Stolten, *Int. J. Hydrogen Energy* **2019**, *44*, 3450–3455.
- [66] S. Geiger, O. Kasian, M. Ledendecker, E. Pizzutilo, A. M. Mingers, W. T. Fu, O. Diaz-Morales, Z. Li, T. Oellers, L. Fruchter, A. Ludwig, K. J. J. Mayrhofer, M. T. M. Koper, S. Cherevko, *Nat. Catal.* **2018**, *1*, 508–515.
- [67] H. Dhawan, M. Secanell, N. Semagina, *Johnson Matthey Technol. Rev.* **2021**, *65*, 247–262.
- [68] V. A. Saveleva, L. Wang, O. Kasian, M. Batuk, J. Hadermann, J. J. Gallet, F. Bournel, N. Alonso-Vante, G. Ozouf, C. Beauger, K. J. J. Mayrhofer, S. Cherevko, A. S. Gago, K. A. Friedrich, S. Zafeiratos, E. R. Savinova, *ACS Catal.* **2020**, *10*, 2508–2516.
- [69] L. Wang, F. Song, G. Ozouf, D. Geiger, T. Morawietz, M. Handl, P. Gazdzicki, C. Beauger, U. Kaiser, R. Hiesgen, A. S. Gago, K. A. Friedrich, *J. Mater. Chem. A* **2017**, *5*, 3172–3178.
- [70] F.-D. Kong, S. Zhang, G.-P. Yin, N. Zhang, Z.-B. Wang, C.-Y. Du, *Electrochem. Commun.* **2012**, *14*, 63–66.
- [71] R. Badam, M. Hara, H.-H. Huang, M. Yoshimura, *Int. J. Hydrogen Energy* **2018**, *43*, 18095–18104.
- [72] X. Wu, B. Feng, W. Li, Y. Niu, Y. Yu, S. Lu, C. Zhong, P. Liu, Z. Tian, L. Chen, W. Hu, C. M. Li, *Nano Energy* **2019**, *62*, 117–126.
- [73] P. Joshi, H.-H. Huang, R. Yadav, M. Hara, M. Yoshimura, *Catal. Sci. Technol.* **2020**, *10*, 6599–6610.
- [74] V. K. Puthiyapura, M. Mamlouk, S. Pasupathi, B. G. Pollet, K. Scott, *J. Power Sources* **2014**, *269*, 451–460.

- [75] P. Mazúr, J. Polonský, M. Paidar, K. Bouzek, *Int. J. Hydrogen Energy* **2012**, *37*, 12081–12088.
- [76] E. Oakton, D. Lebedev, M. Povia, D. F. Abbott, E. Fabbri, A. Fedorov, M. Nachtegaal, C. Copéret, T. J. Schmidt, *ACS Catal.* **2017**, *7*, 2346–2352.
- [77] Y. Kuroda, H. Igarashi, T. Nagai, T. W. Napporn, K. Matsuzawa, S. Mitsushima, K.-i. Ota, A. Ishihara, *Electrocatalysis* **2019**, *10*, 459–465.
- [78] X. Li, A. L. Zhu, W. Qu, H. Wang, R. Hui, L. Zhang, J. Zhang, *Electrochim. Acta* **2010**, *55*, 5891–5898.
- [79] H. Malik, S. Sarkar, S. Mohanty, K. Carlson, *Sci. Rep.* **2020**, *10*, 8050.
- [80] W. Zhou, W. Li, J.-Q. Wang, Y. Qu, Y. Yang, Y. Xie, K. Zhang, L. Wang, H. Fu, D. Zhao, *J. Am. Chem. Soc.* **2014**, *136*, 9280–9283.
- [81] Z.-X. Lu, Y. Shi, C.-F. Yan, C.-Q. Guo, Z.-D. Wang, *Int. J. Hydrogen Energy* **2017**, *42*, 3572–3578.
- [82] H. Lv, G. Zhang, C. Hao, C. Mi, W. Zhou, D. Yang, B. Li, C. Zhang, *RSC Adv.* **2017**, *7*, 40427–40436.
- [83] C. Hao, H. Lv, Q. Zhao, B. Li, C. Zhang, C. Mi, Y. Song, J. Ma, *Int. J. Hydrogen Energy* **2017**, *42*, 9384–9395.
- [84] A. Hartig-Weiss, M. Miller, H. Beyer, A. Schmitt, A. Siebel, A. T. S. Freiberg, H. A. Gasteiger, H. A. El-Sayed, *ACS Appl. Nano Mater.* **2020**, *3*, 2185–2196.
- [85] H. Ohno, S. Nohara, K. Kakinuma, M. Uchida, H. Uchida, *Catalysts* **2019**, *9*, 74.
- [86] L. Solà-Hernández, F. Claudel, F. Maillard, C. Beauger, *Int. J. Hydrogen Energy* **2019**, *44*, 24331–24341.
- [87] K. Peters, P. Zeller, G. Stefanic, V. Skoromets, H. Němec, P. Kužel, D. Fattakhova-Rohlfing, *Chem. Mater.* **2015**, *27*, 1090–1099.
- [88] H.-S. Oh, H. N. Nong, T. Reier, A. Bergmann, M. Gliech, J. Ferreira de Araújo, E. Willinger, R. Schlögl, D. Teschner, P. Strasser, *J. Am. Chem. Soc.* **2016**, *138*, 12552–12563.
- [89] M. Bühler, P. Holzapfel, D. McLaughlin, S. Thiele, *J. Electrochem. Soc.* **2019**, *166*, F1070–F1078.
- [90] R. O’Hayre, F. B. Prinz, *J. Electrochem. Soc.* **2004**, *151*, A756.
- [91] M. Mandal, M. Secanell, *J. Power Sources* **2022**, *541*, 231629.
- [92] A. Orfanidi, P. J. Rheinländer, N. Schulte, H. A. Gasteiger, *J. Electrochem. Soc.* **2018**, *165*, F1254–F1263.
- [93] M. Bernt, C. Schramm, J. Schröter, C. Gebauer, J. Byrknes, C. Eickes, H. A. Gasteiger, *J. Electrochem. Soc.* **2021**, *168*, 084513.
- [94] B. Britton, S. Holdcroft, *J. Electrochem. Soc.* **2016**, *163*, F353–F358.
- [95] M. Moore, M. Mandal, A. Kosakian, M. Secanell, *J. Electrochem. Soc.* **2023**, *170*, 044503.

- [96] Y. Jang, C. Seol, S. M. Kim, S. Jang, *Int. J. Hydrogen Energy* **2022**, *47*, 18229–18239.
- [97] D. Bernsmeier, M. Bernicke, R. Schmack, R. Sachse, B. Paul, A. Bergmann, P. Strasser, E. Ortel, R. Kraehnert, *ChemSusChem* **2018**, *11*, 2367–2374.
- [98] D. Böhm, M. Beetz, C. Gebauer, M. Bernt, J. Schröter, M. Kornherr, F. Zoller, T. Bein, D. Fattakhova-Rohlfing, *Appl. Mater. Today* **2021**, *24*, 101134.
- [99] M. Bühler, F. Hegge, P. Holzapfel, M. Bierling, M. Suermann, S. Vierrath, S. Thiele, *J. Mater. Chem. A* **2019**, *7*, 26984–26995.
- [100] M. Mandal, M. Moore, M. Secanell, *ACS Appl. Mater. Interfaces* **2020**, *12*, 49549–49562.
- [101] P. Holzapfel, M. Bühler, C. van Pham, F. Hegge, T. Böhm, D. McLaughlin, M. Breitwieser, S. Thiele, *Electrochem. Commun.* **2020**, *110*, 106640.
- [102] J. Xie, K. L. More, T. A. Zawodzinski, W. H. Smith, *J. Electrochem. Soc.* **2004**, *151*, A1841.
- [103] K. Ehelebe, N. Schmitt, G. Sievers, A. W. Jensen, A. Hrnjić, P. Collantes Jiménez, P. Kaiser, M. Geuß, Y.-P. Ku, P. Jovanovič, K. J. J. Mayrhofer, B. Etzold, N. Hodnik, M. Escudero-Escribano, M. Arenz, S. Cherevko, *ACS Energy Lett.* **2022**, *7*, 816–826.
- [104] A. Bornet, R. Pittkowski, T. M. Nielsen, E. Berner, A. Maletzko, J. Schröder, J. Quinson, J. Melke, K. M. Ø. Jensen, M. Arenz, *ACS Catal.* **2023**, *13*, 7568–7577.
- [105] C. Immerz, M. Paidar, G. Papakonstantinou, B. Bensmann, T. Bystron, T. Vidaković-Koch, K. Bouzek, K. Sundmacher, R. Hanke-Rauschenbach, *J. Appl. Electrochem.* **2018**, 701–711.
- [106] L. Xing, W. Shi, H. Su, Q. Xu, P. K. Das, B. Mao, K. Scott, *Energy* **2019**, *177*, 445–464.
- [107] O. Antoine, Y. Bultel, P. Ozil, R. Durand, *Electrochim. Acta* **2000**, *45*, 4493–4500.
- [108] Y. T. Li, H. Guo, F. Ye, *Int. J. Energy Res.* **2022**, *46*, 8872–8890.
- [109] C. Immerz, B. Bensmann, P. Trinke, M. Suermann, R. Hanke-Rauschenbach, *J. Electrochem. Soc.* **2018**, *165*, F1292–F1299.
- [110] H.-N. Su, S.-J. Liao, Y.-N. Wu, *J. Power Sources* **2010**, *195*, 3477–3480.
- [111] A. D. Taylor, E. Y. Kim, V. P. Humes, J. Kizuka, L. T. Thompson, *J. Power Sources* **2007**, *171*, 101–106.
- [112] L. Ye, Y. Gao, S. Zhu, J. Zheng, P. Li, J. P. Zheng, *Int. J. Hydrogen Energy* **2017**, *42*, 7241–7245.
- [113] Y. Qiu, H. Zhang, H. Zhong, F. Zhang, *Int. J. Hydrogen Energy* **2013**, *38*, 5836–5844.
- [114] D. Song, Q. Wang, Z. Liu, M. Eikerling, Z. Xie, T. Navessin, S. Holdcroft, *Electrochim. Acta* **2005**, *50*, 3347–3358.

- [115] H. Nguyen, D. Sultanova, P. A. Heizmann, S. Vierrath, M. Breitwieser, *Mater. Adv.* **2022**, *3*, 8460–8468.
- [116] G.-Y. Chen, C. Wang, Y.-J. Lei, J. Zhang, Z. Mao, Z.-Q. Mao, J.-W. Guo, J. Li, M. Ouyang, *Int. J. Hydrogen Energy* **2017**, *42*, 29960–29965.
- [117] K.-H. Kim, H.-J. Kim, K.-Y. Lee, J. H. Jang, S.-Y. Lee, E. Cho, I.-H. Oh, T.-H. Lim, *Int. J. Hydrogen Energy* **2008**, *33*, 2783–2789.
- [118] Z. Xie, T. Navessin, K. Shi, R. Chow, Q. Wang, D. Song, B. Andreaus, M. Eikerling, Z. Liu, S. Holdcroft, *J. Electrochem. Soc.* **2005**, *152*, A1171.
- [119] L. Xing, W. Shi, P. K. Das, K. Scott, *AIChE J.* **2017**, *63*, 4895–4910.
- [120] Y. Xu, G. Chang, R. Fan, T. Cai, *Int. J. Energy Res.* **2022**, *46*, 21028–21044.
- [121] J. Thomas, T. Gemming, *Analytical Transmission Electron Microscopy : An Introduction for Operators*, Springer Netherlands, Heidelberg, **2014**.
- [122] R. F. Egerton, *Physical Principles of Electron Microscopy : An Introduction to TEM, SEM, and AEM*, 2nd ed., Springer International Publishing, Basel, **2016**.
- [123] N. Bassim, K. Scott, L. A. Giannuzzi, *MRS Bull.* **2014**, *39*, 317–325.
- [124] W. Massa, *Kristallstrukturbestimmung*, 8th ed., Springer Spektrum, Wiesbaden, **2015**.
- [125] R. Guinebretiere, *X-ray diffraction by polycrystalline materials*, ISTE, London Newport Beach, CA, **2007**.
- [126] J. F. Watts, J. Wolstenholme, *An Introduction to Surface Analysis by XPS and AES*, John Wiley and Sons Ltd., Chichester, **2003**.
- [127] P. W. Atkins, J. de Paula, *Physikalische Chemie*, 4th ed., Wiley-VCH, Weinheim, **2006**.
- [128] D. Pröfrock, A. Prange, *Appl. Spectrosc.* **2012**, *66*, 843–868.
- [129] R. Bottom in *Principles and Applications of Thermal Analysis*, (Ed.: P. Gabbott), Blackwell Publishing, Oxford, **2008**, pp. 87–118.
- [130] A. J. Bard, G. Inzelt, F. Scholz, *Electrochemical Dictionary*, 2nd, Springer, Berlin and Heidelberg, **2012**.
- [131] C. M. A. Brett, A. M. O. Brett, *Electrochemistry Principles, Methods, and Applications*, Oxford University Press, New York, **1993**.
- [132] A. J. Bard, M. Stratmann, P. R. Unwin, *Encyclopedia of Electrochemistry - Instrumentation and Electroanalytical Chemistry*, Wiley-VCH, Weinheim, **2003**.
- [133] R. Riasse, C. Lafforgue, F. Vandenberghe, F. Micoud, A. Morin, M. Arenz, J. Durst, M. Chatenet, *J. Power Sources* **2023**, *556*, 232491.
- [134] T. Lazaridis, B. M. Stühmeier, H. A. Gasteiger, H. A. El-Sayed, *Nat. Catal.* **2022**, *5*, 363–373.
- [135] P. K. Giesbrecht, M. S. Freund, *J. Phys. Chem. C Nanomater. Interfaces* **2022**, *126*, 17844–17861.

- [136] Q. Meyer, S. Liu, Y. Li, C. Zhao, *J. Power Sources* **2022**, 533, 231058.
- [137] S. M. Alia, K. E. Hurst, S. S. Kocha, B. S. Pivovarov, *J. Electrochem. Soc.* **2016**, 163, F3051–F3056.
- [138] S. Zhao, H. Yu, R. Maric, N. Danilovic, C. Capuano, K. Ayers, W. Mustain, *J. Electrochem. Soc.* **2015**, 162, F1292–F1298.
- [139] M. Gollasch, J. Schmeling, C. Harms, M. Wark, *Adv. Mater. Interfaces* **2023**, 2300036.
- [140] L. Wang, P. Lettenmeier, U. Golla-Schindler, P. Gazdzicki, N. A. Cañas, T. Morawietz, R. Hiesgen, S. S. Hosseiny, A. S. Gago, K. A. Friedrich, *PCCP* **2016**, 18, 4487–4495.
- [141] R. Adams, R. L. Shriner, *J. Am. Chem. Soc.* **1923**, 45, 2171–2179.
- [142] D. F. Abbott, D. Lebedev, K. Waltar, M. Povia, M. Nachtegaal, E. Fabbri, C. Copéret, T. J. Schmidt, *Chem. Mater.* **2016**, 28, 6591–6604.
- [143] C. Felix, T. Maiyalagan, S. Pasupathi, B. Bladergroen, V. Linkov, *Micro Nanosyst.* **2016**, 4, 186–191.
- [144] S. Abbou, R. Chattot, V. Martin, F. Claudel, L. Solà-Hernandez, C. Beauger, L. Dubau, F. Maillard, *ACS Catal.* **2020**, 10, 7283–7294.
- [145] Y. Zhao, E. A. Hernandez-Pagan, N. M. Vargas-Barbosa, J. L. Dysart, T. E. Mallouk, *J. Phys. Chem. Lett.* **2011**, 2, 402–406.
- [146] D. Böhm, M. Beetz, M. Schuster, K. Peters, A. G. Hufnagel, M. Döblinger, B. Böller, T. Bein, D. Fattakhova-Rohlfing, *Adv. Funct. Mater.* **2020**, 30, 1906670.
- [147] F. Bizzotto, J. Quinson, A. Zana, J. J. K. Kirkensgaard, A. Dworzak, M. Oezaslan, M. Arenz, *Catal. Sci. Technol.* **2019**, 9, 6345–6356.
- [148] N. Trogisch, M. Koch, E. N. El Sawy, H. A. El-Sayed, *ACS Catal.* **2022**, 12, 13715–13724.
- [149] T. H. Wan, M. Saccoccio, C. Chen, F. Ciucci, *Electrochim. Acta* **2015**, 184, 483–499.
- [150] T. H. Wan, M. Saccoccio, C. Chen, F. Ciucci, DRTtools, **2022**, <https://github.com/ciuccislab/DRTtools>.
- [151] V. Pfeifer, T. E. Jones, J. J. Velasco Vélez, C. Massué, R. Arrigo, D. Teschner, F. Girgsdies, M. Scherzer, M. T. Greiner, J. Allan, M. Hashagen, G. Weinberg, S. Piccinin, M. Hävecker, A. Knop-Gericke, R. Schlögl, *Surf. Interface Anal.* **2016**, 48, 261–273.
- [152] P. F. Karimi, B. Peppley, A. Bazylak, *ECS Trans.* **2015**, 69, 87–98.
- [153] H.-S. Oh, H. N. Nong, T. Reier, M. Gliech, P. Strasser, *Chem. Sci.* **2015**, 6, 3321–3328.
- [154] V. K. Puthiyapura, S. Pasupathi, H. Su, X. Liu, B. Pollet, K. Scott, *Int. J. Hydrogen Energy* **2014**, 39, 1905–1913.
- [155] S. Geiger, O. Kasian, B. R. Shrestha, A. M. Mingers, K. J. J. Mayrhofer, S. Cherevko, *J. Electrochem. Soc.* **2016**, 163, F3132–F3138.

- [156] C. Wang, F. Lan, Z. He, X. Xie, Y. Zhao, H. Hou, L. Guo, V. Murugadoss, H. Liu, Q. Shao, Q. Gao, T. Ding, R. Wei, Z. Guo, *ChemSusChem* **2019**, *12*, 1576–1590.
- [157] D. Gall, *J. Appl. Phys.* **2016**, *119*, 085101.
- [158] F. Claudel, L. Dubau, G. Berthomé, L. Sola-Hernandez, C. Beauger, L. Piccolo, F. Maillard, *ACS Catal.* **2019**, *9*, 4688–4698.
- [159] H. A. El-Sayed, A. Weiß, L. F. Olbrich, G. P. Putro, H. A. Gasteiger, *J. Electrochem. Soc.* **2019**, *166*, F458–F464.
- [160] P. Lettenmeier, J. Majchel, L. Wang, V. A. Saveleva, S. Zafeiratos, E. R. Savinova, J.-J. Gallet, F. Bournel, A. S. Gago, K. A. Friedrich, *Chem. Sci.* **2018**, *9*, 3570–3579.
- [161] V. Pfeifer, T. E. Jones, J. J. Velasco Vélez, R. Arrigo, S. Piccinin, M. Hävecker, A. Knop-Gericke, R. Schlögl, *Chem. Sci.* **2017**, *8*, 2143–2149.
- [162] H. G. Sanchez Casalongue, M. L. Ng, S. Kaya, D. Friebel, H. Ogasawara, A. Nilsson, *Angew. Chem. Int. Ed.* **2014**, *53*, 7169–7172.
- [163] P. Steegstra, M. Busch, I. Panas, E. Ahlberg, *J. Phys. Chem. C Nanomater. Interfaces* **2013**, *117*, 20975–20981.
- [164] P. G. Pickup, V. I. Birss, *J. Electroanal. Chem. Interfacial Electrochem.* **1987**, *220*, 83–100.
- [165] O. Reid, F. S. Saleh, E. B. Easton, *Electrochim. Acta* **2013**, *114*, 278–284.
- [166] P. Connor, J. Schuch, B. Kaiser, W. Jaegermann, *Z. Phys. Chem.* **2020**, *234*, 979–994.
- [167] Z.-Y. Wu, F.-Y. Chen, B. Li, S.-W. Yu, Y. Z. Finfrock, D. M. Meira, Q.-Q. Yan, P. Zhu, M.-X. Chen, T.-W. Song, Z. Yin, H.-W. Liang, S. Zhang, G. Wang, H. Wang, *Nat. Mater.* **2023**, *22*, 100–108.
- [168] F. Liao, K. Yin, Y. Ji, W. Zhu, Z. Fan, Y. Li, J. Zhong, M. Shao, Z. Kang, Q. Shao, *Nat. Commun.* **2023**, *14*, 1248.
- [169] S. Cherevko, S. Geiger, O. Kasian, A. Mingers, K. J. Mayrhofer, *J. Electroanal. Chem. (Lausanne)* **2016**, *774*, 102–110.
- [170] C. Liang, R. Rao, K. Svane, J. Hadden, B. Moss, S. Scott, M. Sachs, J. Murawski, A. Frandsen, J. Riley, M. Ryan, J. Durrant, J. Rossmeisl, I. Stephens, “Unravelling the effects of active site densities and energetics on the water oxidation activity of iridium oxides”, **2023**, <https://doi.org/10.21203/rs.3.rs-2605628/v1>.
- [171] A. Weiß, A. Siebel, M. Bernt, T.-H. Shen, V. Tileli, H. A. Gasteiger, *J. Electrochem. Soc.* **2019**, *166*, F487–F497.
- [172] J. García-Martínez, M. Johnson, J. Valla, K. Li, J. Y. Ying, *Catal. Sci. Technol.* **2012**, *2*, 987.
- [173] N. A.-F. Aboul-Maaty, H. A.-S. Oraby, *Bull. Natl. Res. Cent.* **2019**, *43*, 1–10.
- [174] V. Minkina, S. Shabunya, V. Kalinin, V. Martynenko, A. Smirnova, *Int. J. Hydrogen Energy* **2008**, *33*, 5629–5635.

- [175] Z. Xie, S. Yu, G. Yang, K. Li, L. Ding, W. Wang, F.-Y. Zhang, *Int. J. Hydrogen Energy* **2021**, *46*, 1155–1162.
- [176] M. Suermann, T. J. Schmidt, F. N. Buchi, *ECS Trans.* **2015**, *69*, 1141–1148.
- [177] U. Babic, T. J. Schmidt, L. Gubler, *J. Electrochem. Soc.* **2018**, *165*, J3016–J3018.
- [178] J. Lopata, Z. Kang, J. Young, G. Bender, J. W. Weidner, S. Shimpalee, *J. Electrochem. Soc.* **2020**, *167*, 064507.
- [179] H. Liu, H. B. Tao, B. Liu, *J. Phys. Chem. Lett.* **2022**, *13*, 6520–6531.
- [180] M. Bernt, A. Siebel, H. A. Gasteiger, *J. Electrochem. Soc.* **2018**, *165*, F305–F314.
- [181] T. E. Springer, T. A. Zawodzinski, S. Gottesfeld, *J. Electrochem. Soc.* **1991**, *138*, 2334.
- [182] S. C. DeCaluwe, A. M. Baker, P. Bhargava, J. E. Fischer, J. A. Dura, *Nano Energy* **2018**, *46*, 91–100.
- [183] A. El Kaddouri, J.-C. Perrin, T. Colinart, C. Moyne, S. Leclerc, L. Guendouz, O. Lottin, *Macromolecules* **2016**, *49*, 7296–7307.
- [184] K. C. Neyerlin, W. Gu, J. Jorne, A. Clark, H. A. Gasteiger, *J. Electrochem. Soc.* **2007**, *154*, B279.
- [185] L. V. Böhre, S. Bullerdiel, P. Trinke, B. Bensmann, A.-L. E. R. Deutsch, P. Behrens, R. Hanke-Rauschenbach, *J. Electrochem. Soc.* **2022**, *169*, 124513.
- [186] X. Tan, J. Shen, N. Semagina, M. Secanell, *J. Catal.* **2019**, *371*, 57–70.
- [187] I. A. Khan, P. Morgen, S. Gyergyek, R. Sharma, S. M. Andersen, *Mater. Chem. Phys.* **2023**, 128192.
- [188] W. Zhang, J. Chang, Y. Yang, *SusMat.* **2023**, *3*, 2–20.
- [189] S. M. Sze, K. K. Ng, *Physics of Semiconductor Devices*, 3., John Wiley & Sons, Ltd, Hoboken, NJ, **2006**.
- [190] H. Lv, S. Wang, Y. Sun, J. Chen, W. Zhou, C. Zhang, *J. Power Sources* **2023**, *564*, 232878.
- [191] S. Dong, C. Zhang, Z. Yue, F. Zhang, H. Zhao, Q. Cheng, G. Wang, J. Xu, C. Chen, Z. Zou, Z. Dou, H. Yang, *Nano Lett.* **2022**, *22*, 9434–9440.

A Appendix

A.1 List of Figures

1.0.1	Circular hydrogen economy schema depicting emission-free electricity generation in yellow, transportation-based hydrogen applications in blue and, industrial hydrogen application in red.	1
3.1.1	Schematic representation of a) the Pourbaix diagram of liquid water, showing the pH value dependence of E^0 according to the Nernst equation and b) the change of thermodynamic parameters with the reaction temperature for liquid and gaseous water along with their respective E^0 or E_{TN} . The depictions were adapted by Li <i>et al.</i> ^[24] with thermodynamic parameters taken from the NIST-JANAF database for thermodynamic parameters. ^[25]	7
3.1.2	Schematic representation of the Tafel plot with extractable parameters. ^[12,23,27]	9
3.1.3	Schematic of the conventional cell design in unipolar and bipolar multi-cell setup and the zero-gap design with electrodes directly on the separator.	11
3.1.4	Schematic of a PEMWE cell.	14
3.1.5	Electrocatalytic activity in O_2 evolution at various oxide electrodes as a function of the enthalpy of the lower to higher oxide transition in alkaline (hollow) and acidic (full) solutions. Reprinted with permission from [53]. Copyright 1984, Elsevier Ltd.	16
3.1.6	Schematic representation of postulated ADEM (left) and LPM (right) OER mechanisms, adapted from Geiger <i>et al.</i> ^[66]	18
3.2.1	Schematic representation of a CL with catalyst support indicated in grey, active catalyst in white and ionomer in yellow with indicated TPB and electronic and ionic charge carrier pathways along with reactant pathways.	22
3.2.2	Schematic representation of a) the electrode patterning following the cells flow field, b) a gradient in x-y direction from inlet to outlet of the flow field, and c) a gradient in z direction of the CCM with the composition gradient indicated in blue shading.	25
4.1.1	Schematic representation of the penetration depth and propagation volume inside the sample in SEM.	30
4.2.1	Schematic representation of the diffraction of X-rays on crystal planes along with the Bragg-Bretano measurement arrangement on the outer circle.	31
4.3.1	Schematic representation of the analysis stages for concentration determination via ICP-MS with (I) representing the vaporizer, (II) representing the plasma ionization, (III) representing the ion optics and lenses, (IV) representing the quadrupole splitting and (V) representing the detector.	33

4.4.1	Schematic representation of the RDE setup.	34
4.4.2	Schematic depiction of a) the applied sinusoidal signal with its corresponding answer signal and b) an exemplary Nyquist plot with half-circles of processes with different resistances.	35
4.4.3	Schematic depiction of a CV of an oxidic Ir catalyst with indicated oxidic Ir charge used to determine q^* in blue.	37
5.3.1	Schematic representation of the different MEA single cell setups.	45
6.1.1	Schematic representation of the resulting CCM thickness per catalyst layer depending on unsupported or supported catalyst usage.	51
6.1.2	Schematic representation of synthesis pathways with the indicated method and proposed formed Ir species.	52
6.1.3	Ir loading for each synthesis for the three different desired loadings with indicated error bars pertaining to the median between both attempts and designated first and second attempts for the MAF method.	54
6.1.4	X-Ray diffractograms of all catalysts as-synthesized with unloaded ATO as reference.	55
6.1.5	X-Ray Diffractograms of different loadings of MAF catalyst.	57
6.1.6	<i>In-situ</i> high-temperature diffractogram for 65 wt.% loaded RS catalyst with indicated peaks corresponding to cubic Ir and tetragonal IrO ₂ and intensity trends with indicated diffractions for cubic Ir (black, ICDD: 00-046-1044), tetragonal IrO ₂ (gray, ICDD: 00-015-0870) and ATO (Sb _{0.1} Sn _{0.9} O ₂ , blue, ICDD: 98-015-5956) Color grading indicates the calcination temperature for blue at room temperature to red at 441 °C with 7 °C steps from 350 to 441 °C.	58
6.1.7	X-Ray Diffractograms of all catalysts both in as-synthesized and calcined form.	59
6.1.8	TEM micrographs of a) 15 wt.% Ir , b) 40 wt.% Ir, c) 65 wt.% uncalcined RS catalysts and d) 15 wt.% Ir calcined RS catalysts. Additionally, e) and f) depict the calcined 65 wt.% RS catalyst with enhanced resolution and indicated lattice spacing in f).	60
6.1.9	TEM micrographs of a) 15 wt.% Ir, b) 40 wt.% Ir, c) 65 wt.% MAF catalysts with d) showing enhanced resolution and indicated lattice spacing.	61
6.1.10	TEM micrographs of a) 15 wt.% Ir, b) 40 wt.%, c) Ir 65 wt.% Ir uncalcined CD catalyst, d) 15 wt.% Ir, e) 40 wt.% Ir, f) 65 wt.% Ir calcined CD catalyst, g) 15 wt.% Ir, h) 40 wt.% Ir, i) 65 wt.% Ir uncalcined HTD catalyst and j) 15 wt.% Ir, k) 40 wt.% Ir calcined HTD catalyst.	62
6.1.11	Comparison between the chemical composition of Ir4f species detected by XPS and indicated in the atomic ratio between different oxidation states for uncalcined and calcined catalysts.	63
6.1.12	Ir 4f high-resolution XP spectra of uncalcined (a-d) and calcined (e-g) catalysts.	64

6.1.13	Mass normalized polarization curves a) of the (upper) uncalcined catalysts and (lower) calcined catalysts with 40 wt.% desired loading and Ir black and MAF catalyst as a reference and b) at a low overpotential of Ir (solid line) and IrO ₂ (dotted line) catalysts with the desired 40 wt.% Ir loading.	67
6.1.14	Cyclic voltammograms of 65 wt.% Ir RS catalyst, during initial electrolyte immersion (blue) and after electrochemical activation procedure (green).	70
6.1.15	Mass activity regarding the catalysts' actual loading with (full) uncalcined catalysts and (hollow) calcined catalysts.	71
6.1.16	S-number (blue) and the amount of produced O atoms (green) during the AST for three selected catalysts.	72
6.2.1	Polarization data for homogeneous CCMs with 10 wt.% and 30 wt.% ionomer loading at a catalyst loading of 1 mg _{Ir} cm ⁻² and 2 mg _{Ir} cm ⁻²	78
6.2.2	Calculated volume fractions for an Ir black catalyst based on the calculations and reference values presented by Bernt <i>et al.</i> ^[12]	79
6.2.3	Polarization curves for homogeneous and gradient CCMs with a) uncompensated and b) HFR compensated potential.	80
6.2.4	Tafel analysis of homogeneous and gradient CCMs of iR-free potential with Tafel slopes determined between 10 and 100 mA cm ⁻²	83
6.2.5	Parameter comparison depending on the total ionomer content of the homogeneous CCMs of a) uncompensated potential at different current densities and b) HFR values with color gradient indicating the current density (0.0-4.0 A cm ⁻²) at which it was calculated (darker color indicating low current density and lighter color indicating high current density).	84
6.2.6	Overpotential breakdown of homogeneous CCMs with different overpotential contributions indicated. Cathodic η_{Ion} is an estimation of 2.5 m Ω cm ² according to Bernt <i>et al.</i> ^[12] and is constant in all CCMs.	88
6.2.7	TG analysis to determine the ionomer content of Ir black CCMs through ionomer decomposition in O ₂ atmosphere.	91
6.2.8	Cross-sectional SEM and EDS images depicting the 10 30 wt.% gradient CCM with Ir and F elemental mappings in arbitrary units along with the SEM image.	91
6.2.9	Cross-sectional SEM and EDS images depicting the 10 30 wt.% gradient CCM with Ir and F elemental mappings in arbitrary units along with the SEM image.	92
6.2.10	Polarization curves for homogeneous and gradient CCMs with a) uncompensated and b) HFR compensated potential and gradient CCMs highlighted.	93
6.2.11	Parameter comparison depending on the total ionomer content of the homogeneous or gradient CCMs of a) uncompensated potential at different current densities and b) HFR values with color gradient indicating the current density at which it was calculated (darker color indicating low current density and lighter color indicating high current density).	94

6.2.12	Ionomer loading dependent visualization of a) the anodic R_{ion}^{CL} and b) the ECSA, calculated before the conditioning period.	95
6.2.13	Overpotential breakdown of gradient CCMs with different overpotential contributions indicated. The cathodic R_{ion}^{CL} is an estimation of $2.5 \text{ m}\Omega \text{ cm}^2$ according to Bernt <i>et al.</i> ^[12] and is constant in all CCMs.	96
6.3.1	Polarization of homogeneous 40wt.% IrO_2/ATO CCMs with varying ionomer loadings.	100
6.3.2	Influence of sequentially recorded polarization curves on the HFR for 40 wt.% IrO_2/ATO CCMs with 5 and 15 wt.% ionomer loading ($m_{ion}/m_{ion} + m_{cat}$).	100
6.3.3	Performance of homogeneous IrO_2/ATO CCMs with a Ir black reference CCM in a) uncompensated polarization data and b) EIS spectra recorded at 25 mA cm^{-2}	102
6.3.4	Performance of homogeneous IrO_2/ATO CCMs with a Ir black reference CCM in a) uncompensated polarization data and b) compensated iR-free polarization data.	103
6.3.5	Kinetic CCM properties calculated by Tafel analysis of differently loaded IrO_2/ATO catalysts at different overall ATO loadings.	105
6.3.6	Dependence of the HFR in comparison to the applied current density for differently loaded IrO_2/ATO CCMs and Ir black reference CCM.	106
6.3.7	Depictions of a) CVs for different IrO_2 loadings on ATO in a thinner and thicker CL and b) dependence of the charge attributed to oxidic Ir redox processes (integration of the capacitance-corrected CV above 0.4 V vs. RHE) in relation to the IrO_2 content and total Ir content in the CL.	108
6.3.8	DRT analysis of a) the homogeneous 40 wt.% IrO_2/ATO low total loading CCM at different current densities with the arrow indicating major shifts in operation change and b) all homogeneous CCMs at 150 mA cm^{-2}	109
6.3.9	DRT analysis of a) the homogeneous 40 and 65 wt.% IrO_2/ATO high total loading CCMs at 0.5 A cm^{-2} and b) the homogeneous 40 and 65 wt.% IrO_2/ATO high total loading CCMs at 1.0 A cm^{-2} with the coloured arrows indicating change in peak position and intensity for either one of the CCMs (blue or green) or both simultaneously (black) from 0.5 to 1.0 A cm^{-2}	111
6.3.10	Performance of gradient and homogeneous IrO_2/ATO CCMs with a Ir black reference CCM in a) uncompensated polarization data and b) compensated iR-free polarization data.	113
6.3.11	Dependence of the HFR in comparison to the applied current density for gradient and homogeneous IrO_2/ATO CCMs.	113
6.3.12	Depictions of a) CVs for gradient and homogeneous IrO_2/ATO CCMs and b) dependence of the charge attributed to IrO redox processes in relation to the IrO_2 content and total Ir content in the CL.	114
6.3.13	DRT analysis of a) gradient and homogeneous IrO_2/ATO CCMs at 0.5 A cm^{-2} and b) gradient and homogeneous IrO_2/ATO CCMs at 1.0 A cm^{-2}	115

A.1	Nyquist-plots of electrochemical impedance spectra of homogeneous IrO ₂ /ATO CCMs recorded at a) 100 mA cm ⁻² , b) 150 mA cm ⁻² , c) 1.0 A cm ⁻² , and d) 2.0 A cm ⁻²	138
A.2	DRT analysis of homogeneous 40 and 65 wt.% IrO ₂ /ATO high total loading CCMs at a) 2.0 A cm ⁻² and b) 4.0 A cm ⁻²	138
A.3	Overpotential breakdown of the homogeneous IrO ₂ /ATO CCMs.	139
A.4	DRT analysis of gradient 40 65 wt.% and 65 40 wt.% CCMs as well as homogeneous 40 and 65 wt.% IrO ₂ /ATO high total loading CCMs at a) 2.0 A cm ⁻² and b) 4.0 A cm ⁻²	139

A.2 List of Tables

5.2.1	Solvent composition for different catalyst materials with solvent ratio of the resulting solvent mixture and solid ratios of the resulting suspension.	42
5.4.1	Deconvolution parameter limits for XPS in adherence to parameters from Pfeifer <i>et al.</i> ^[151]	48
6.2.1	Contributions of anodic R_{Ion}^{CL} for the different homogeneous ionomer loading CCMs.	86
6.3.1	Compositions and overall Ir loading of the IrO ₂ /ATO CCMs.	103
A.1	Educts for different loading variants of the Reduction synthesis method. Other solvents and additives were not changed between Ir loadings.	140
A.2	Educts for different loading variants of the Adams Fusion synthesis method. Other solvents and additives were not changed between Ir loadings.	140
A.3	Educts for different loading variants of the Colloidal deposition method. Other solvents and additives were not changed between Ir loadings.	140
A.4	Educts for different loading variants of the Hydrothermal synthesis method. Other solvents and additives were not changed between Ir loadings.	140
A.5	Crystallite sizes for cubic Ir (111) and tetragonal IrO ₂ (110) faces, calculated by Scherrer analysis of all different catalysts both uncalcined and calcined. * marked cells show reflexes too low in intensity for rigorous analysis - marked cells display the absence of a reflex	141
A.6	i_0 and Tafel slopes for the ionomer gradient CCMs.	141
A.7	R_{Ion}^{CL}, i_0 and Tafel slopes for the Ir loading gradient CCMs.	142

A.3 Supplementary Figures

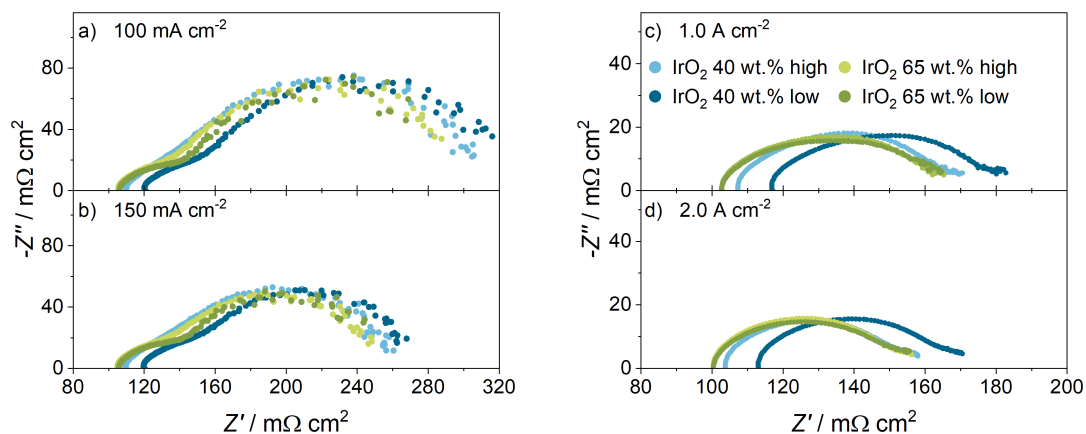


Figure A.1: Nyquist-plots of electrochemical impedance spectra of homogeneous IrO₂/ATO CCMs recorded at a) 100 mA cm⁻², b) 150 mA cm⁻², c) 1.0 A cm⁻², and d) 2.0 A cm⁻²

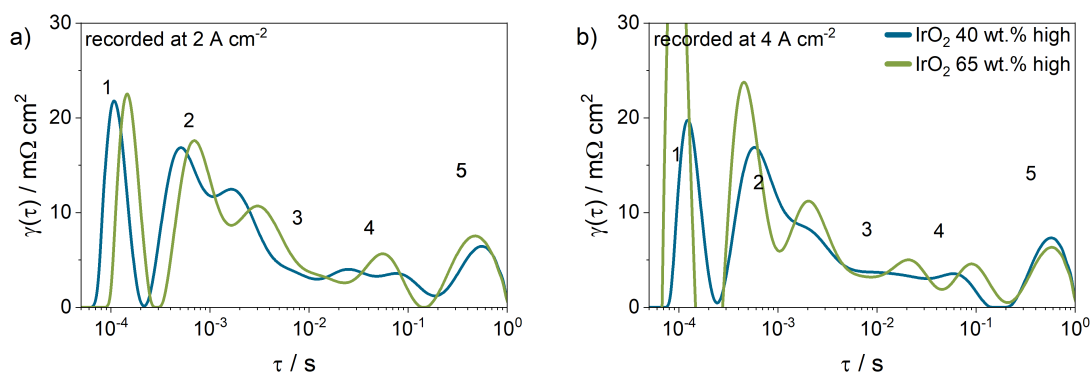


Figure A.2: DRT analysis of homogeneous 40 and 65 wt.% IrO₂/ATO high total loading CCMs at a) 2.0 A cm⁻² and b) 4.0 A cm⁻².

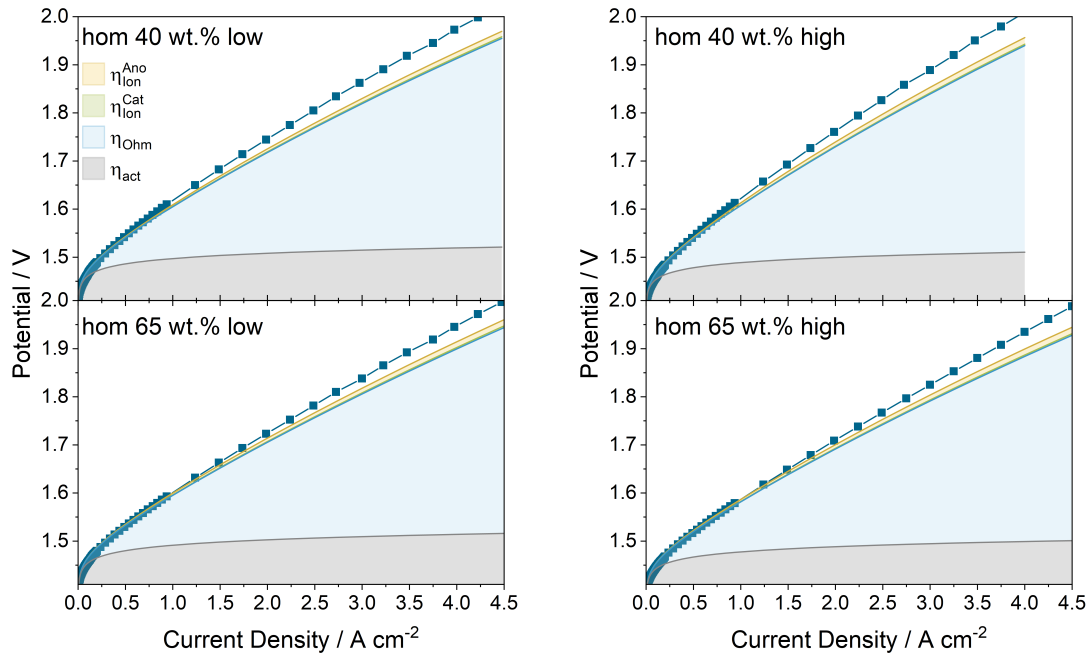


Figure A.3: Overpotential breakdown of the homogeneous IrO₂/ATO CCMs.

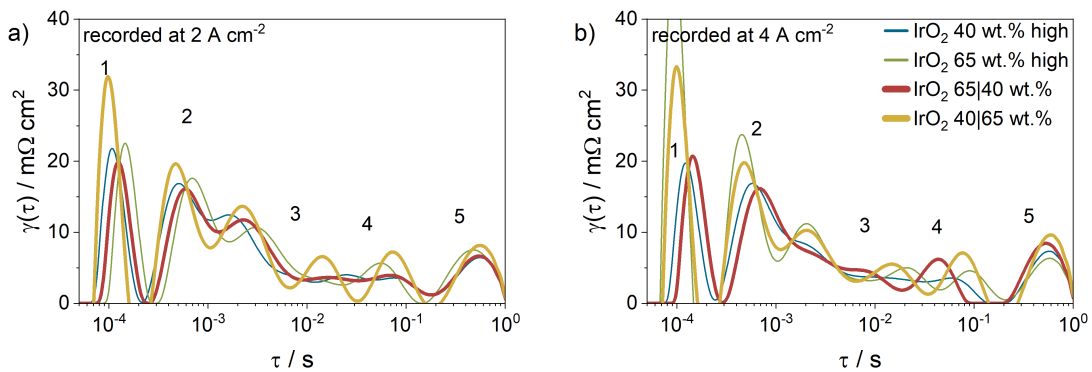


Figure A.4: DRT analysis of gradient 40|65 wt.% and 65|40 wt.% CCMs as well as homogeneous 40 and 65 wt.% IrO₂/ATO high total loading CCMs at a) 2.0 A cm⁻² and b) 4.0 A cm⁻².

A.4 Supplementary Tables

Table A.1: Educts for different loading variants of the Reduction synthesis method. Other solvents and additives were not changed between Ir loadings.

Ir loading / wt.%	ATO / mg	$\text{IrCl}_3 \cdot x\text{H}_2\text{O}$ / mg	NaBH_4 / mg
15 wt.%	170.0	56.0	108.0
40 wt.%	170.0	212.0	290.0
65 wt.%	170.0	590.0	471.0

Table A.2: Educts for different loading variants of the Adams Fusion synthesis method. Other solvents and additives were not changed between Ir loadings.

Ir loading / wt.%	ATO / mg	$\text{IrCl}_3 \cdot x\text{H}_2\text{O}$ / mg	NaNO_3 / g
15 wt.%	185.0	61.0	3.0
40 wt.%	110.0	137.0	3.0
65 wt.%	65.0	183.0	3.0

Table A.3: Educts for different loading variants of the Colloidal deposition method. Other solvents and additives were not changed between Ir loadings.

Ir loading / wt.%	ATO / mg	H_2IrCl_6 / mg
15 wt.%	160.0	60.0
40 wt.%	43.0	60.0
65 wt.%	15.0	60.0

Table A.4: Educts for different loading variants of the Hydrothermal synthesis method. Other solvents and additives were not changed between Ir loadings.

Ir loading / wt.%	ATO / mg	Ir Colloid / mL	<i>tert.</i> -butanol / mL
15 wt.%	160.4	190.0	90.0
40 wt.%	42.9	190.0	90.0
65 wt.%	15.3	190.0	90.0

Table A.5: Crystallite sizes for cubic Ir (111) and tetragonal IrO₂ (110) faces, calculated by Scherrer analysis of all different catalysts both uncalcined and calcined.
 * marked cells show reflexes too low in intensity for rigorous analysis
 - marked cells display the absence of a reflex

Catalyst	uncalcined		calcined	
	Ir ⁰ (111)	IrO ₂ (110)	Ir ⁰ (111)	IrO ₂ (110)
RS 15 wt. %	2.0 nm	-	*	3.1 nm
RS 40 wt. %	1.7 nm	-	5.3 nm	2.8 nm
RS 65 wt. %	1.7 nm	-	6.3 nm	2.8 nm
HTD 15 wt. %	*	-	*	*
HTD 40 wt. %	3.0 nm	-	*	3.2 nm
HTD 65 wt. %	*	*	*	*
CD 15 wt. %	-	-	-	*
CD 40 wt. %	-	-	-	3.2 nm
CD 65 wt. %	-	-	-	*
MAF 15 wt. %	-	2.9 nm	-	-
MAF 40 wt. %	-	2.0 nm	-	-
MAF 65 wt. %	-	1.7 nm	-	-

Table A.6: i_0 and Tafel slopes for the ionomer gradient CCMs.

CCM	Tafel slope / mV dec ⁻¹	i_0 / A cm ⁻²
hom. 5 wt. % Nafion	44.8	5.2×10^{-8}
hom. 10 wt. % Nafion	47.3	1.2×10^{-7}
hom. 20 wt. % Nafion	48.0	1.4×10^{-7}
hom. 30 wt. % Nafion	44.4	3.8×10^{-8}
gra. 30 10 wt. % Nafion	41.9	1.5×10^{-8}
gra. 10 30 wt. % Nafion	44.5	8.2×10^{-8}

Table A.7: R_{ion}^{CL} , i_0 and Tafel slopes for the Ir loading gradient CCMs.

CCM	Tafel slope / mV dec ⁻¹	i_0 / A cm ⁻²	R_{ion}^{CL} / m Ω cm ²
hom. 40 wt.% IrO ₂ /ATO low	36.6	2.1 x 10 ⁻⁹	10.9
hom. 40 wt.% IrO ₂ /ATO high	35.6	2.1 x 10 ⁻⁹	16.7
hom. 65 wt.% IrO ₂ /ATO low	37.5	4.7 x 10 ⁻⁹	13.1
hom. 65 wt.% IrO ₂ /ATO high	35.6	4.1 x 10 ⁻⁹	14.3
gra. 65 40 wt.% IrO ₂ /ATO	34.6	1.7 x 10 ⁻⁹	13.2
gra. 40 65 wt.% IrO ₂ /ATO	34.3	1.7 x 10 ⁻⁹	12.3

A.5 Supplementary Equations

$$V_{cat} = \frac{L_{cat}}{\rho_{cat} d_{CL}} \quad (A.1)$$

Where V_{cat} is the volume occupied by the catalyst, L_{cat} is the catalyst loading, ρ_{cat} is the density of the catalyst, and d_{CL} is the thickness of the CL.^[12]

$$V_{ion} = \frac{L_{ion}}{\rho_{ion} d_{CL}} \quad (A.2)$$

Where V_{ion} is the volume occupied by the ionomer in the dry state, L_{ion} is the ionomer loading, and ρ_{ion} is the density of the ionomer in a dry state with a value of 2.1 g cm^{-2} and a factor of 1.8 was added to reflect the swelling behavior of the ionomer at $80 \text{ }^\circ\text{C}$, immersed in water.^[12]

$$\eta_{act} = \frac{RT}{\alpha F} \operatorname{arsinh} \frac{i}{i_0} = \frac{b}{2.3} \operatorname{arsinh} \frac{i}{i_0} \quad (A.3)$$

Where b is the Tafel slope. η_{act} is specific for each electrode with its corresponding α_{ano} or α_{cat} .

A.6 Publication and Conference Contributions

Journal Publications

1. **M. Gollasch**, J. Schmeling, C. Harms, M. Wark,
Comparative Analysis of Synthesis Routes for Antimony-Doped Tin Oxide-Supported Iridium and Iridium oxide Catalysts for OER in PEM Water Electrolysis,
Advanced Materials Interfaces 2023, 2300036.

Conference Contributions

1. **M. Gollasch**, C. Harms, M. Wark,
Functional Ionomer Gradients in Anode Catalyst Layers for Low Temperature PEM Water Electrolysis,
242nd Electrochemical Society Meeting 2022, Atlanta, United States, oral presentation.
2. **M. Gollasch**, J. Schmeling, C. Harms, M. Wark,
Evaluation of iridium and iridium oxide-based supported catalyst syntheses for oxygen evolution in PEM water electrolysis,
CARISMA 2023, Lefkada Island, Greece, oral presentation.

Journal Publications beyond this Thesis

1. **M. Gollasch**, J. Müller-Hülstede, H. Schmies, D. Schonvogel, P. Wagner, A. Dyck, M. Wark,
Elucidating Synergistic Effects of Different Metal Ratios in Bimetallic Fe/Co-N-C Catalysts for Oxygen Reduction Reaction,
Catalysts 2021, 11, 7, 841.

A.7 Abbreviations and Symbols

List of Symbols

a	activity
$A_{electrode}$	electrode area
α	charge transfer coefficient
α_{ano}	anodic charge transfer coefficient
α_{cat}	cathodic charge transfer coefficient
b	kinetic resistance
C_{DL}	double layer capacitance
d_{CL}	thickness of the CL
ΔG	change in overall free Gibbs enthalpy
ΔG°	free Gibbs enthalpy
ΔH	change in overall enthalpy
d_{hkl}	separation of crystal planes
ΔH°	change in enthalpy
Δ_p	path-length difference
ΔS	change in overall entropy
ΔS°	change in entropy
E	cell potential
E^0	reversible standard potential
E_{ano}^0	reversible standard potential of the anode
E_{cat}^0	reversible standard potential of the cathode
E_B	binding energy
E_{kin}	kinetic energy
E_{TN}	thermo-neutral potential
f	frequency
F	Faraday constant
$\gamma(\tau)$	DRT process-associated resistance
η	overpotential
h	Planck's constant

η_{act}	activation overpotential
η_{Ion}	ionic overpotential
η_{MT}	mass transport overpotential
η_{Ohm}	ohmic overpotential
i	current
i_0	exchange current
j	imaginary unit number
λ	wavelength
L_{cat}	catalyst loading
L_{ion}	ionomer loading
L_{Ir}	Ir loading
$\lambda_{Tikhonov}$	Tikhonov regularization parameter
m	FWHM-coefficient
\dot{n}	substance flow
ν	wave frequency
n_{Ir}	amount of dissolved Ir
n_{O_2}	amount of produced O ₂
Θ	glancing angle
q^*	mass-specific charge
$Q_{H_{upd}}$	charge of the H _{upd}
q_{Ir}	charge density of H on Ir
Θ_s	spectrometer work function
r	scan rate
ρ	density
R	universal gas constant
R_{Ion}^{CL}	catalyst layer ionic sheet resistance
R_{Ion}^{eff}	effective ionic CL resistance
R_{Ohm}	Ohmic resistance
τ	time constant
t	time
T	temperature

U_{corr}	corrected potential
V_{cat}	volume occupied by the catalyst
V_{ion}	volume occupied by the ionomer
ξ	kinetic correction factor
z	electron transfer number
Z	impedance
Z'	real part of the impedance
Z''	imaginary part of the impedance

List of Abbreviations

ADEM	adsorbate evolution mechanism
AEMWE	anion-exchange water electrolysis
AST	accelerated stress test
ATO	Sb-doped SnO ₂
AWE	alkaline water electrolysis
BBP	bipolar plate
BSE	back-scattering electron
CAPEX	capital expenditure
CCM	catalyst coated membrane
CD	colloidal deposition
CL	catalyst layer
CTAB	cetyltrimethylammonium bromide
CV	cyclic voltammetry
DRT	distribution of relaxation times
ECSA	electrochemical surface area
EDS	energy dispersive X-ray spectroscopy
EIS	electrochemical impedance spectroscopy
FE	Faradaic efficiency
FWHM	full-width half-maximum
GCO	Gd-doped CeO ₂
GDE	gas-diffusion electrode
GDL	gas-diffusion layer
H _{upd}	hydrogen underpotential deposition
HER	hydrogen evolution reaction
HFR	high-frequency resistance
HHV	higher heating value
HR	high-resolution
HTD	hydrothermal deoposition
ICP	inductively coupled plasma
LHV	lower heating value

LPM	lattice participated mechanism
LSV	linear sweep voltammetry
MAF	modified Adam's fusion
MEA	membrane electrode assembly
MS	mass spectrometry
OER	oxygen evolution reaction
OPEX	operational expenditure
ORR	oxygen reduction reaction
PEM	proton-exchange membrane
PEMWE	proton-exchange membrane water electrolysis
PFSA	perfluoro sulfonic acid
PGM	Pt-group metal
PTE	porous transport electrode
PTFE	polytetrafluoroethylene
PTL	porous transport layer
RDE	rotating disk electrode
RHE	reversible hydrogen electrode
RS	reduction synthesis
SEM	scanning electron microscopy
SGL	Gaussian-Lorentzian sum
SMSI	strong metal-support interaction
SOWE	solid-oxide water electrolysis
TEM	transmission electron microscopy
TGA	thermogravimetric analysis
TOF	turn-over frequency
TPB	triple-phase boundary
VE	voltage efficiency
WE	working electrode
XPS	X-ray photoelectron spectroscopy
XRD	X-ray diffraction
YSZ	Y-stabilized ZrO ₂

Erklärung

Hiermit erkläre ich, Marius Gollasch, geboren am 15.08.1994 in Delmenhorst, dass ich diese Dissertation selbstständig verfasst habe und die benutzten Hilfsmittel vollständig angegeben sind. Die Dissertation wurde bereits in Teilen veröffentlicht und es ist eine Publikationsliste beigefügt. Ich erkläre, dass die Dissertation weder in ihrer Gesamtheit noch in Teilen einer anderen Hochschule zur Begutachtung in einem Promotionsverfahren vorliegt oder vorlag. Die Regelungen zu guter wissenschaftlicher Praxis der Carl von Ossietzky Universität Oldenburg wurden befolgt. Im Zusammenhang mit dem Promotionsvorhaben wurden keine kommerziellen Vermittlungs- oder Beratungsdienste (Promotionsberatung) in Anspruch genommen.

Oldenburg, 17.10.2023

Marius Gollasch